EXTRACTION OF OCEAN WAVE INFORMATION FROM MICROWAVE NAUTICAL RADAR IMAGES: FOURIER METHOD VS WAVELET METHOD

JIAQI AN

Extraction of Ocean Wave Information from Microwave Nautical Radar Images: Fourier Method vs Wavelet Method

by

©Jiaqi An, B.Eng.

A thesis submitted to the School of Graduate Studies in partial fulfillment of the requirements for the degree of

Master of Engineering

Faculty of Engineering and Applied Science

Memorial University of Newfoundland

September, 2013

St. John's Newfoundland

Abstract

The development of algorithms for extracting ocean wave information from X-band nautical radar images is addressed. The algorithms are designed based on the three-dimensional (3-D) fast Fourier transform (FFT) and two-dimensional (2-D) continuous wavelet transform (CWT). First, in order to design the 3-D FFT-based wave algorithm, methods for extracting sea surface current information using least squares (LS), iterative LS, and normalized scalar product (NSP) methods are examined. With the results of mode classification of wave components from the iterative LS current estimation process, an improved wave measurement algorithm is proposed in which a modified band-pass filter is constructed to retain the contributions of the fundamental wave only and to remove the harmonics and non-wave components for wave information extraction. Noise components and aliasing effects are also eliminated based on existing theories and techniques associated with 3-D FFT-based wave field analysis. An alternative scheme for wave measurement using the 2-D CWT is also presented. The relationship of the scaling factor of the CWT and the minimum distinguishable wavenumber is developed and its expression is presented with a calibration factor. Empirical optimal values of the scaling parameter for variable wave conditions are provided based on extensive simulated radar tests. Based on the existing techniques employed in the classic 3-D FFT analysis, a look-up-table method and an iterative method are proposed to determine the calibration factor. For the iterative method,

a self-adaptive wavelet analysis algorithm for wave measurement is developed. The designed wave algorithms are first evaluated with the numerical simulation under various sea conditions, assuming shadowing modulation (SH) and tilt modulation (TM). Then for further validation, the algorithms are applied to dual-polarized radar field data collected on the east coast of Canada. Results derived from FFT- and CWT-based algorithms are analyzed and compared with *in situ* TRIAXYS directional wave buoy data collected in the same region. The comparisons reveal that the proposed algorithms are practical and effective for retrieving ocean wave information from the radar data.

Acknowledgements

The author wishes to thank his supervisors Dr. Weimin Huang, Dr. Eric Gill, and the Faculty of Engineering and Applied Science for providing him the opportunity of conducting this research in nautical radar image processing. During the two-year study, the author received solid training, valuable experience, and professional guidance from his supervisors. Their great patience and invaluable guidance have not only helped the author with the research project, but also have provided him the courage and confidence for future research and career development.

This work was supported by a Research and Development Corporation (RDC) IRIF Ignite grant (207765) and a Natural Sciences and Engineering Research Council of Canada Discovery Grant (NSERC 402313-2012) to Dr. W. Huang, a NSERC Discovery Grant (238263-2010) and an Atlantic Innovation Fund (AIF) to Dr. E. Gill, and a RDC Ocean Industries Student Research Award (208695). The provision of the radar field data by Rutter Technologies is gratefully acknowledged. Finally, the author would like to thank his parents. None of the work could have been completed without their patience, support and understanding.

Table of Contents

List of Tables

List of Figures

List of Symbols

The page numbers indicated are the place of first mention.

Chapter 1

Introduction

1.1 Background of Study

Ocean wave and current parameters, including wave propagation direction, mean period, peak frequency, and current velocity, provide important information for the safety and efficiency of operation and routing of marine traffic as well as for offshore platform design and maintenance. Such information can be acquired by a variety of means including visual observations of the sea surface, buoy measurements, analysis of synthetic aperture radar (SAR) data, and inverting radar plan position indicator (PPI) images. In practice, all methods will experience some limitations in monitoring the maritime space. For example, results of visual observation are highly dependent on the experience of the observers. Satellite data can provide wave field averaged over a large area, but it is costly to obtain. Furthermore, satellite-borne sensors cannot provide continuous ocean wave measurement of a specified area since it usually takes hours or days for a satellite to revisit the same area of the earth. Although moored wave buoys record relatively accurate directional wave field information, they only provide the local sea state conditions where the buoy is deployed and are of limited

utility to mobile ships [1].

Due to the interaction of the electromagnetic signal transmitted by the nautical radar with ripples on the ocean surface, a backscattered signal is received by the radar and becomes visible on the display unit. This signal is commonly referred to as sea clutter [2], and traditionally it was considered as undesirable noise for ship operation and navigation purposes during the early time of radar development. However, such "noise" contains useful information about ocean waves and surface currents. The correlation of the display unit clutter with the wave field was not addressed meaningfully until Wright proposed an approach for imaging ocean waves from sea clutter in X-band radar images in 1965 [3].

Conventional nautical radar is installed on most vessels and scans the sea surface with high temporal and spatial resolution. Also, it produces consecutive images of a specified area which allows continuous sea state monitoring without directional ambiguity. It is not as easily damaged as moored buoys which may experience collisions with ocean traffic or be shaken under severe sea states. Therefore, using remote sensing techniques to measure reliable dynamic ocean wave and current parameters from PPI images of a nautical radar becomes a convenient and reliable solution for continuous and real-time sea state surveillance under a wide variety of ocean conditions without incurring additional capital cost.

The Newfoundland and Labrador region encompasses over 29,000 kilometers of coastline and St. John's is one of the oldest harbors in North America. Newfoundland is famous for its traditional fishery industry as one of the world's three major fishing grounds. Extensive ship and surface platform operations occur in the region due to the substantial activity of the local oil industry. With this as a motivation for this research, algorithms are developed to provide reliable environmental information so that these maritime activities may be conducted safely and efficiently.

1.2 Literature Review

In the past forty years, remote sensing techniques have evolved quickly and many applications for the measurement of the ocean waves and currents have been designed. Significant efforts have been expended in the research of ocean wave monitoring systems such as synthetic aperture radar (SAR) [4], side-looking aperture radar (SLAR) [5], and high-frequency (HF) radar [6]. Also, the wave and current measurement capabilities of typical nautical radars that operate in the X-band for sea surface surveillance have been investigated. X-band radars, operating at wavelengths of 2.50 cm to 3.75 cm, transmit an electromagnetic signal that interacts with the rough sea surface and then receive the backscattered field (see Fig. 1.1). The backscattered signals are then converted to PPI images. Unlike the costly satellite surveillance or the easily damaged wave buoy instrument, the conventional nautical radars installed on most vessels can provide high temporal and spatial resolution mapping of continuous ocean surface processes. During the 1960s, Ijima *et al.* [7] and Wright [3] presented an approach for imaging ocean waves using a marine radar. Before that research, the ocean backscatter was simply considered as a kind of noise since it obscured target echoes in the marine radar image [8]. Subsequent early research was conducted to monitor ocean waves and estimate the wave direction, wave length, and wave period from the radar images [9]-[12]. At that time, data was stored as analog signals on film.

In the 1980s, radar images were digitized for two-dimensional (2-D) Fourier transform (FFT) analysis and 2-D spectra similar to those obtained from buoy data were derived [13], [14]. These so-called radar image spectra demonstrated the possibility of using nautical radar images for wave measurement. However, a 180° directional ambiguity was observed on the 2-D image spectrum obtained from the radar image, and this could not be removed without obtaining wave direction information by other

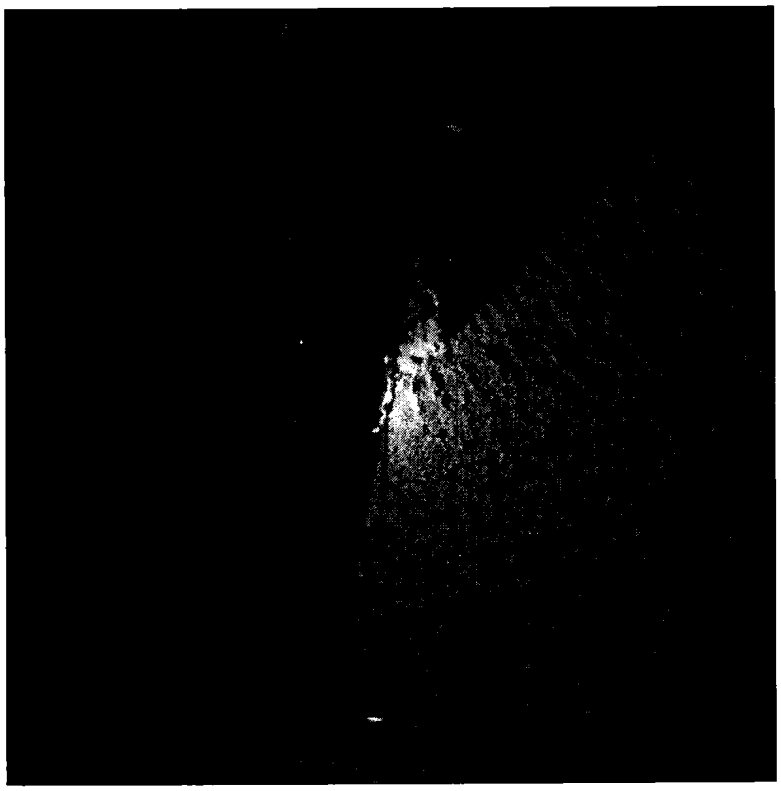

Figure 1.1: An X-band nautical radar plan position indicator (PPI) image collected on the east coast of Canada on Dec.20, 2010

means. Atanassov *et al.* [15] proposed a method to eliminate the directional ambiguity by using two radar images for wave analysis. In 1985, Young [16] proposed a three-dimensional (3-D) FFT-based algorithm to be applied to time sequences of digitized radar images in order to eliminate the 180° ambiguity in phase. This method considered the changes of the sea clutter in both time and space. Before wave retrieval, Young estimated current by a least squares (LS) method. Next, a two-dimensional shell was constructed based on the derived current information and the Doppler-shifted dispersion relationship between the wave vector $\vec{k}$ and angular frequency ω as given by

$$\omega(\vec{k}, \vec{u}) = \sqrt{g\left|\vec{k}\right| \tanh(\left|\vec{k}\right| h)} + \vec{k} \cdot \vec{u} \tag{1.1}$$

where g is the acceleration due to gravity (= 9.8 m/s), h is the water depth, and $\vec{u}$ is the near surface current. By introducing this shell, energy that does not belong to the wave field and falls outside the shell is eliminated. Compared with previous research, Young's 3-D FFT analysis retrieved more accurate ocean wave spectra and parameters. Later it was found that the derived 3-D image spectrum consists of three major components:

1. wave energy due to the backscatter modulation;

2. background noise due to the sea surface roughness;

3. higher harmonics of the wave energy due to radar imaging effects.

In Young's method, background noise and harmonic component effects were not considered. According to the Nyquist–Shannon sampling theorem, aliasing effects may also occur when the sampling frequency of the radar system is small (as may occur at low antenna rotation speeds). In 1998, Nieto Borge [17] proposed a solution to overcome the Nyquist limit issue for wave measurement, thus allowing wave parameters to be estimated from the radar image spectrum [18], [19].

A comprehensive list of wave parameters and wave-related functions for wave extraction was published by the International Association for Hydro-Environment Engineering and Research (IAHR) working group on wave generation and analysis for maritime applications [20], [21]. Among these wave parameters, ocean wave height was also obtained from the radar imagery [22]. For nautical radar images, it has been reported by Ziemer *et al.* [23] that the significant wave height (H_s) is proportional to the signal-to-noise ratio (SNR) of the radar backscatter. Later, Nieto Borge [24] presented an improved method for significant wave height estimation. Field experiments were conducted for his algorithm validation [25], [26]. For grazing incidence, an alternative method to estimate H_s based on shadowing statistics was designed by

Wenzel [27]. This method was validated by Henschel *et al.* [28], and Buckley and Aler [29], [30].

The simulation of radar images has also been studied for the purpose of wave algorithm development. For example, in 1995, Seemann and Ziemer [31] developed an approach for computer simulation of imaging ocean wave fields. It was found that the longer waves become visible in the radar images because they modulate the sea clutter signals. Other features associated with the marine radar image may be summarized as [2], [32]-[34]:

- range dependence
- azimuthal dependence with the wind direction
- wind speed dependence
- azimuthal dependence with the wave propagation direction
- wave tilt modulation (TM)
- shadowing modulation (SH), which occurs when higher waves are present
- wave hydrodynamic modulation (HM) due to the motion of the water particles

These features contribute extra energy components to the derived spectrum and significantly affect energy distributions of the wave field imaged by the marine radar. Therefore, it is necessary to consider these phenomena both in the process of simulating the nautical radar images and in measuring the wave and current information. In this process, HM describes the modulation of the energy of the ripples by the interaction with the longer waves; TM is the modulation due to the changes of the effective incidence angle along the long wave slope; and SH is the partial shadowing of the sea

surface from the radar antenna by higher waves [35], [36]. Researchers also demonstrated means of numerically simulating sea clutter images at grazing incidence by applying shadowing and tilt modulation on an ocean surface generated with a specified wave spectrum [32], [37]. An alternative method for simulating marine radar images was proposed by Nomiyama *et al.* [1], [38], [39]. In their research, the PPI images were generated based on calibrated normalized radar cross section (NRCS) statistics [40]-[44].

In order to improve the wave measurement result, in 1997, Senet *et al.* [45]-[47] developed a new method to determine the near surface current velocity based on Young's theory. They considered the aliasing effect as well as the harmonics in the spectral analysis and performed the least squares (LS) method iteratively. Gangeskar [48] introduced a weighted function into the LS method to compensate for the errors in current estimation which increases the accuracy of the derived current velocity. Recently, a novel strategy to retrieve current information with a maximization of the normalized scalar product (NSP) has been proposed by Serafino [49], [50]. Compared to Senet's iteration method, large current velocity derived from Serafino's method is more accurate for low speed antennas.

A complete 3-D FFT-based algorithm for wave and current information extraction has been designed and successfully incorporated in the commercialized Wave Monitoring System (WaMoS) by Nieto Borge *et al.* [51]-[53] at the German GKSS Research Center, Geesthacht.

Comparisons of the results derived from the shipborne WaMos system with pitch-roll buoy data were reported by Alfonso *et al.* [54]. Data analysis from radars on a floating production and offloading platform (FPSO) was conducted by Nieto Borge *et al.* in 2000 [55]. Results of this algorithm have also been compared with scalar wave data [51] and directional waverider buoy data [56]. However, those comparisons are

mainly made at the level of spectral parameters in an illustrative way and only a few examples of the directional spectra were provided. Later, a systematic and extensive comparison of the spectral analysis of ocean wave fields were presented by Izquierdo *et al.* [57]-[59], where the obtained statistics were listed in detail to quantify the degree of agreement between the parameters estimated from the data sets provided by different sensors.

Wave estimation methods have also been developed by research groups in Asia. These include Hirayama *et al.* [60]-[63], Iseki *et al.* [64], Yoshimoto *et al.* [65], and Ishida [66]. They developed algorithms for robust estimation of wave direction [39], [1] and significant wave height [67], [68] using the PPI images. In 2010, the performance of the Fourier-based algorithms was tested for various sea conditions and results were derived by Cui *et al.* [69], [70] from dual-polarized marine radar data. The influence of non-linear ocean waves on X-band nautical radar observations was discussed by Li *et al.* [71].

In addition to the Fourier analyses, more recently, the wavelet transform, which allows the mother wavelet to be translated in the space domain and dilated in the frequency domain [72], [73], has emerged as a useful, flexible, and efficient technique for wave analysis. In 1995, Carlson [74] proposed the application of two-dimensional wavelet analysis for noise reduction and image enhancement in SAR images of the sea surface. In 1997, D. Jordan *et al.* [75] addressed the implementation issues associated with the continuous wavelet transform for digital time series analysis. Later, Massel [76] demonstrated that the Morlet wavelet transform can be used for analyzing one-dimensional signals of surface waves. Based on the IAHR list of sea state parameters [21], Huang [77] clarified the existing wave parameters and functions and introduced new parameters in the wavelet analysis. Antoine *et al.* [78] discussed the two dimensional wavelet analysis and its application in image processing. Wu *et al.*

proposed using a 2-D continuous wavelet transform (CWT) to process X-band nautical radar data. Mother wavelet selection and wavelet configuration for radar image processing were presented in their research. Image wavenumber spectra were successfully derived from both simulated sea surface elevation maps and experimental radar data [79]-[83].

1.3 Scope of Thesis

After reviewing the existing theories and techniques for wave measurement, improved algorithms for retrieving ocean wave information using the 3-D FFT and 2-D CWT are developed in this thesis.

The 3-D FFT-based algorithm for the retrieval of wave and current information proposed by Nieto Borge [51]-[53] provides better results than the earlier studies. In that algorithm, a band-pass filter based on the Doppler-shifted dispersion relationship is constructed in order to remove the energy that does not belong to the wave field. Also, aliasing effects are eliminated using a back folding strategy [51]-[53]. However, the non-wave components, and fundamental and higher-order harmonic wave components that fall in the pass band of the filter are all used for wave spectrum derivation, and this may contaminate the final results. In this thesis, the classic 3-D FFT-based algorithm is improved with an enhanced band-pass filter. In the proposed band-pass filtering process, sample points of fundamental components are preserved while all the harmonics and non-wave components are eliminated.

As for the wavelet-based wave algorithm proposed by Wu *et al.* [79]-[83], the numerical simulation testing in their research was conducted on the sea surface elevation map instead of simulated radar images. Also, modulation effects, such as tilt and shadowing, were not considered. Most of their research was focused on non-homogeneous

wave field wavelet-based analysis. The selection of the particular wavelet parameters under different wave conditions was not explored in detail. Furthermore, only image wavenumber spectra were presented and studied [79]-[83]. In this thesis, both a look-up-table-based and a self-adaptive 2-D CWT-based algorithm for extracting ocean wave information from X-band nautical radar images are presented.

The organization of this thesis is as follows:

In Chapter 2, the current estimation techniques using LS, iterative LS, and NSP methods are examined. The theories and techniques used in the classic Fourier-based wave analysis algorithms are reviewed. Based on the mode classification results obtained using the iterative LS current method, an improved algorithm for retrieving wave information is then proposed. In this method, fundamental components are discriminated from other sample points for the band-pass filtering process.

The theory of the wavelet transform and its application in wave field analysis are investigated in Chapter 3. The relationship between the scaling factor and the minimum distinguishable wavenumber is derived, and its expression is presented in terms of a calibration factor. Empirical optimal values of the scaling parameter for variable wave conditions are provided based on extensive simulated radar tests. Based on the existing techniques employed in the classical 3-D FFT method, an iterative method for determining the calibration factor is designed. Look-up-table-based and self-adaptive wavelet analysis algorithms for wave measurement are also proposed.

In Chapter 4, the proposed algorithms are first tested with simulated radar images under various sea conditions, assuming shadowing (SH) and tilt modulation (TM). Then, for further validation, the algorithms are applied to both horizontally polarized (H-pol) and vertically polarized (V-pol) radar field data collected on the east coast of Canada. Results retrieved from both the 3-D FFT-based algorithm and the 2-D CWT-based algorithm are presented, analyzed, and compared with *in situ* buoy

records.

Finally, conclusions and related future work are provided in Chapter 5.

Chapter 2

3-D Fourier-based Algorithms for Wave Measurement

In the 3-D Fourier-based wave analysis, the temporal sequences composed of consecutive sea clutter images from a nautical radar system are processed to obtain the temporal and spatial change of the ocean wave field [84]. Without sea surface current, the energy of the ocean waves is localized on the dispersion shell on the image spectrum produced by applying the Fourier transform to the radar image sequence. However, if the radar images are collected from a moving vessel or if a non-zero near-surface current is present, the dispersion shell will be deformed due to the Doppler shift, as described in equation (1.1). Thus, the moving vessel and near-surface current velocities should be determined before any attempt is made to retrieve the ocean wave information [32]. In this chapter, the classic and modified 3-D FFT-based wave analysis algorithms for retrieving current and wave information are discussed.

2.1 3-D FFT-based Current Information Extraction Methods

The 3-D FFT-based algorithm for ocean wave and current information extraction was initially proposed by Young *et al.* in 1985 [16], and later refined by Nieto *et al.* [51]-[59]. The basic step-wise procedure, with corresponding rational, to extract wave information from the radar data may be summarized as:

- sub-image acquisition: to reduce the complexity of the algorithm computations
- image normalization: to eliminate main contributions of the static patterns in space and time;
- 3-D FFT analysis on an image sequence: to obtain 3-D image spectra;
- high-pass filtering: to remove non-stationary and non-homogeneous components near zero frequency;
- current estimation: to obtain near-surface current information;
- band-pass filtering: to discriminate the wave energy from undesired components;
- conversion from image spectra to wave spectra using an MTF: to mininize the non-linearity due to the radar imaging mechanism;
- derivation of wave spectra and parameters such as
  - directional frequency spectra $E(f, \theta)$
  - frequency spectra $E(f)$
  - mean wave direction $\theta(f)$
  - overall mean wave direction θ_w

– mean period T_{01} and peak frequency f_p.

From the listed step-wise procedure, it is found that in order to determine the surface current information, multiple processing steps, including sub-image acquisition and normalization, 3-D spectral analysis, and high-pass filtering, need to be employed first. These are detailed in Section 2.2.1. This section focuses on the current algorithms assuming that the high-pass filtered image spectra have been obtained.

Young *et al.* [16] proposed a least squares (LS) method in which only the fundamental dispersion relationship is used for current estimation, and Senet *et al.* improved this LS method by calculating the current velocity iteratively based on the higher order harmonic dispersion relationship and an anti-aliasing scheme [17], [47]. Serafino *et al.* presented another approach to determine the optimal current that maximizes the normalized scalar product (NSP) [49], [50]. In this section, these 3-D FFT-based current estimation methods are discussed briefly. Modifications of the latter two methods to improve the computational efficiency and accuracy, as suggested by Huang *et al.* [85]-[87], are also presented.

2.1.1 The Least Squares Method

In [16] and [47], in order to account for the Doppler shift, the vector sum of the platform's (e.g., vessel's) velocity $\vec{u}_s$ and the current velocity $\vec{u}_c$ is defined as the velocity of encounter $\vec{u}_e$.

$$\vec{u}_e = \vec{u}_s + \vec{u}_c \tag{2.1}$$

The Doppler frequency shift, induced by the near-surface current down to the penetration depth of the waves, can be observed in the wave field imaged by the nautical radar. The penetration depth for a single wave is approximately half of its wavelength $\lambda/2$ [47]. Stewart *et al.* [88] have shown that the component of the velocity of

encounter $\vec{u}_e$ in the direction of the wave vector $\vec{k}$ is a weighted mean current over the upper layer of the ocean. This result can be extended to consider the full current vector [16] as

$$\vec{u}_c = 2k \int_{-d}^{0} \vec{u}_e(z) e^{(2kz)} dz \tag{2.2}$$

where z is the vertical coordinate, d is the depth of the upper layer for surface current determination, and $\vec{u}_e(z)$ is the vertical velocity vector profile.

Young's least squares current regression approach is based on the fundamental water dispersion relation of the ocean surface gravity waves, wave vector $\vec{k}$ and angular frequency ω. This Doppler-shifted dispersion relationship is written as

$$\omega(\vec{k}, \vec{u}_e) = \varsigma + \omega_D \tag{2.3}$$

where the first term ς is the intrinsic frequency. If the water is deep enough, ς can be simplified as

$$\varsigma = \sqrt{gk} \tag{2.4}$$

The second term, ω_D, is the Doppler frequency, defined as

$$\omega_D = |\vec{u}_e| \left|\vec{k}\right| \cos\theta_{\vec{k}\vec{u}} = k_x u_x + k_y u_y \tag{2.5}$$

where $\theta_{\vec{k}\vec{u}}$ is the angle between the wave and velocity vectors, k_x, u_x, k_y, u_y are the wavenumber and velocity components in the x and y directions, respectively. It is observed from (2.5) that the Doppler frequency is affected by the velocity component projected in the direction of wave vector $\vec{k}$. The intrinsic and Doppler-shifted dispersion shells are illustrated in Fig. 2.1. The figure clearly shows that the dispersion shell is significantly deformed due to the velocity of encounter.

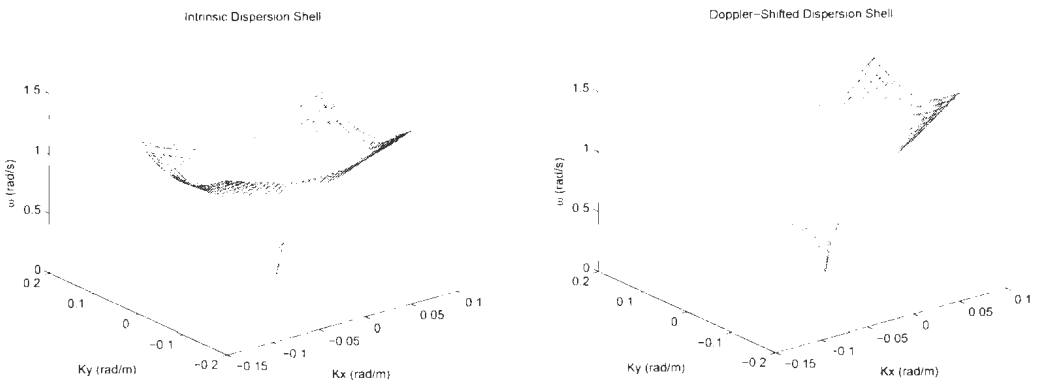

Figure 2.1: (a) Intrinsic and (b) Doppler-shifted dispersion shell

The criterion for LS current estimation is written as [47]

$$Q^2 = \sum_{i=1}^{N} (\left|\omega_i - \omega(\vec{k}_i)\right|^2) \rightarrow min \tag{2.6}$$

where N is the number of coordinates collected for the least squares fitting process, ω_i is the ith sampled frequency component from image spectrum $I(k_x, k_y, \omega)$ after high-pass filtering, and $\omega(\vec{k}_i)$ is the angular frequency calculated by (2.3) at the ith sampled wave vector component. The ith Doppler term in (2.6) is defined as

$$\omega_{iD} = \omega_i - \omega(\vec{k}_i) \tag{2.7}$$

The current velocity (u_x, u_y) that minimizes Q^2 satisfies the following two equations

$$\begin{aligned} \partial Q^2 / \partial u_x &= 0 \\ \partial Q^2 / \partial u_y &= 0 \end{aligned} \tag{2.8}$$

Equation (2.8) can be rewritten as

$$\begin{pmatrix} D_{xx} & D_{xy} \\ D_{yx} & D_{yy} \end{pmatrix} \begin{pmatrix} u_x \\ u_y \end{pmatrix} = \begin{pmatrix} b_x \\ b_y \end{pmatrix} \tag{2.9}$$

where

$$D_{xx} = \sum_{i=1}^{N} k_{ix}^2 \tag{2.10}$$

$$D_{xy} = D_{yx} = \sum_{i=1}^{N} k_{ix} k_{iy} \tag{2.11}$$

$$D_{yy} = \sum_{i=1}^{N} k_{iy}^2 \tag{2.12}$$

$$b_x = \sum_{i=1}^{N} k_{ix} \omega_{iD} \tag{2.13}$$

$$b_y = \sum_{i=1}^{N} k_{iy} \omega_{iD} \tag{2.14}$$

where k_{ix}, k_{iy} are the ith wavenumber components in x and y direction, respectively. Equation (2.9) can be rewritten more compactly as

$$D\vec{u}_e = \vec{b} \tag{2.15}$$

where the definitions of D, $\vec{u}_e$, and $\vec{b}$ are obvious. If D is invertible (i.e., $\det(D) \neq 0$), the current vector is given by [47]

$$\vec{u}_e = D^{-1}\vec{b} \tag{2.16}$$

2.1.2 The Iterative Least Squares Method

Young's LS current estimation algorithm is designed using the fundamental dispersion relationship (1.1). Higher harmonic components are not considered. In addition, measures to overcome the aliasing effect due to the low sampling frequency are not included. Thus, the classic LS method needs to be improved to include the higher harmonics and to overcome aliasing effects. The harmonic and aliasing effects are discussed as below.

Harmonic effects

Higher harmonic components are caused by non-linearity of the nautical radar imaging and the non-linearity of the ocean waves [47]. The harmonic effects are depicted in Fig. 2.2. In the figure, the BGN spectral energy is assumed as background noise.

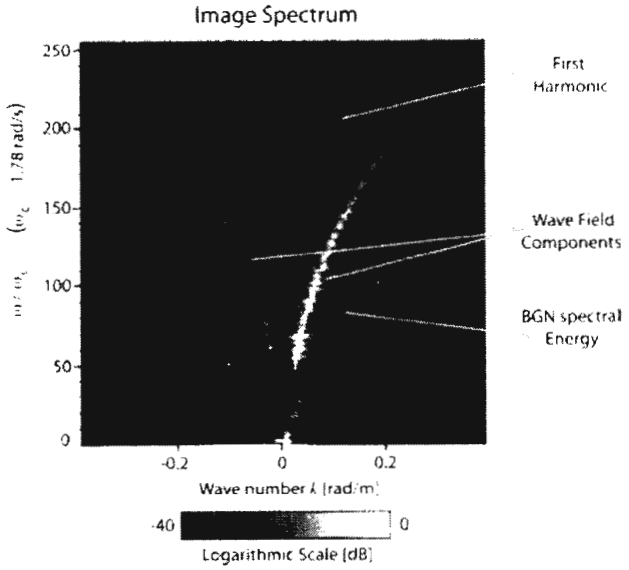

Figure 2.2: Harmonic effects observed from the 2-D image spectrum (taken from Nieto Borge *et al.* [2]).

By introducing the factor $p+1$ into (1.1), a harmonic dispersion relation of order

p is obtained for wave analysis, and may be written as

$$\omega_p(\vec{k}, \vec{u}_e) = (p+1)\sqrt{\frac{g|\vec{k}|}{p+1}} + \vec{k} \cdot \vec{u}_e \tag{2.17}$$

It is obvious that the fundamental components without harmonics can be also expressed by (2.17) with $p = 0$.

Aliasing effects

If the radar is operated with a low antenna rotation speed, the wave signals collected from the system may be undersampled. According to the Nyquist-Shannon sampling theorem [89]-[91], signals with a frequency f whose absolute values are higher than the Nyquist frequency f_N will not be recovered. Such frequencies may be expressed mathematically as

$$|f| > f_N = \frac{f_s}{2} \tag{2.18}$$

where f_s is the sampling frequency as determined by the antenna rotation speed. As discussed in [17], this aliasing effect can be eliminated by the property of $2\omega_N$ periodicity and the Hermitian property of the 3-D FFT. These properties may be written, respectively, as

$$I(k_x, k_y, \omega) = I(k_x, k_y, \omega + 2n\omega_N) \tag{2.19}$$

$$I(k_x, k_y, \omega) = I(-k_x, -k_y, -\omega) \tag{2.20}$$

where n is an integer, and

$$\omega_N = 2\pi f_N \tag{2.21}$$

Iterative LS method

Based on the aforementioned harmonic dispersion relation and back-folding strategy (see Fig. 2.3), a two-step LS current regression algorithm is proposed by Senet *et al.* [45]-[47] as follows:

1. Apply Young's LS method to obtain a first guess of the current velocity.

2. Update the current velocity results iteratively with consideration of the fundamental and harmonic components, combining a strategy of reconstructing the aliased dispersion shells.

In the first guess estimation, an energy threshold T_{FG} is applied to separate the spectral samples of the fundamental mode from the undesired components such as non-linear samples, aliased signals, and the background noise. It is assumed that all the sample points after the thresholding process with T_{FG} will be located in the interval $[0, \omega_{Ny}]$ with no aliasing effects.

Once the first guess of the current velocity is obtained, the LS criterion in (2.6) is revised for the iterative current estimation and may be written as

$$Q^2 = \sum_{i'=1}^{N'} (\left|\omega_{i'} - \omega_{p,r}(\vec{k}_{i'})\right|^2) \rightarrow min \tag{2.22}$$

where N' is the number of coordinates collected for the iterative LS process, and $\omega_{i'}$ is the i'th sampled frequency component from the image spectrum $I(\vec{k}_{i'}, \omega_{i'})$. With a lower threshold T_{IT}, most of the noise components are eliminated and the sample points $(\vec{k}_{i'}, \omega_{i'})$ preserved are fundamental and 1st harmonics, i.e. $p = 0, 1$, respectively. In (2.22), $\omega_{p,r}(\vec{k}_{i'})$ is the pth order aliased wave frequency calculated from (2.17) using the previous current velocity, and the frequency is folded within $[0, \omega_N]$ by the $2\omega_N$ periodicity and Hermitian property. r indicates the range of frequency

derived from (2.17) before aliasing.

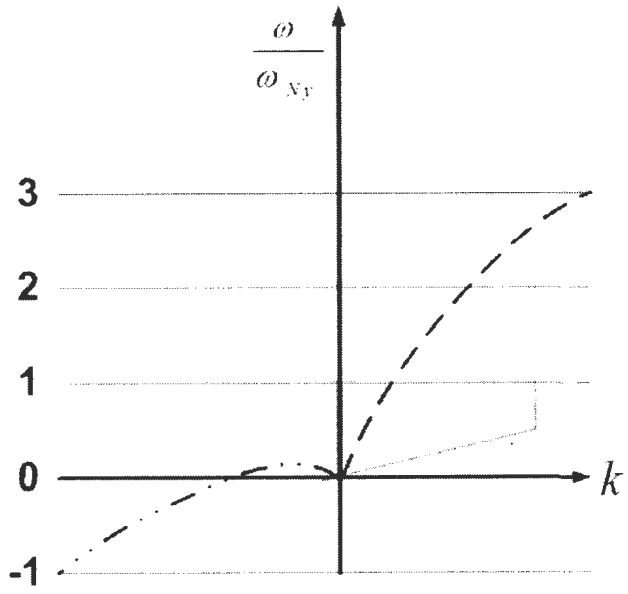

Figure 2.3: Back-folding strategy used to overcome the Nyquist limit.

The points preserved after the thresholding process are then classified as contributions from the fundamental, 1st-order, higher order harmonic components with mapped frequencies $\omega_{p,r}(\vec{k}_{i'})$ $(p = 0, 1, ...)$ or noise. For the i'th sample $(\vec{k}_{i'}, \omega_{i'})$, the classification is accomplished by evaluating the difference between the mapped angular frequencies $\omega_{p,r}(\vec{k}_{i'})$ $(p = 0, 1)$ and $\omega_{i'}$. If

$$MIN(\left|\omega_{i'} - \omega_{p,r}(\vec{k}_{i'})\right|) > \Delta\omega \tag{2.23}$$

the i'th sample point will be regarded as higher-order wave contributions or noise and discarded. $\Delta\omega$ is the frequency resolution determined by the sampling frequency.

The following equation is evaluated for mode classification:

$$\xi = \left|\omega_{i'} - \omega_{0,r}(\vec{k}_{i'})\right| - \left|\omega_{i'} - \omega_{1,r}(\vec{k}_{i'})\right| \tag{2.24}$$

If $\xi < 0$, the sample associated with $\omega_{i'}$ is treated as a fundamental component; otherwise, it is regarded as a 1st-order harmonic component.

Once the mode of every sample point is determined, the corresponding dispersion relationship is used for current estimation. After a new current velocity is calculated from the LS process, it is then used in (2.17) for another round of LS estimation. This process is repeated until a preset termination criterion is satisfied.

In Senet's research, a fixed number of 10 iterations is applied to calculate the velocity [47]. It was observed during the research that the number of iterations required for an accurate estimation of velocity depends on the quality of the first guess [85]. Thus, a revised termination criterion is suggested to improve the efficiency and accuracy of the LS estimation [86]: if the iteration result converges to a specified value, the iteration process can be terminated. This criterion can be written as

$$\begin{cases} \left| u_{x_n} - u_{x_{n-1}} \right| \leq \delta \\ \left| u_{y_n} - u_{y_{n-1}} \right| \leq \delta \end{cases} \tag{2.25}$$

where u_{x_n}, u_{y_n} are the present values of the derived current velocities in the x and y directions, and $u_{x_{n-1}}$, $u_{y_{n-1}}$ are the previous iteration results for the derived current velocities in the x and y directions. δ is the convergence condition. The value of $\delta = 0.005$ m/s used throughout this thesis appears to be sufficient for all tested cases. This value is determined by the resolution of the retrieved current from a series of test data, as discussed in [86], which guarantees the retrieved current information is sufficiently accurate in the iteration process.

Threshold selection is crucial in discriminating the components of interest from the undesired signals. Here, the threshold for the first guess estimation T_{FG} is selected as 20% of the peak energy in the image spectrum, and for the iteration process, T_{IT} is chosen between $2\% - 3\%$ [47].

If the radar images are collected on a moving vessel, according to (2.1) the velocity of encounter $\vec{u}_e$ retrieved from the iterative LS method is the vector sum of the vessel's velocity $\vec{u}_s$ and the near-surface current velocity $\vec{u}_c$. Usually, the vessel's velocity $\vec{u}_s$ is available from navigation instruments such as a GPS device. Therefore, the true velocity of the surface current $\vec{u}_c$ can be obtained by subtracting $\vec{u}_s$ from the derived vector $\vec{u}_e$.

2.1.3 The Normalized Scalar Product Method

In addition to the LS and iterative LS method, a novel strategy to retrieve the information of a high speed current was proposed by Serafino *et al.* [49]. Unlike the iterative LS method, this method does not rely on the selection of the threshold for sampling, and produces reliable results even when the velocity of encounter is very large. The current information is determined through the maximization of the normalized scalar product (NSP) between the amplitude of the high-pass filtered image spectrum $|I(k_x, k_y, \omega)|$ and the characteristic function $G(k_x, k_y, \omega, u_x, u_y)$. The characteristic function can be written as

$$G(k_x, k_y, \omega, u_x, u_y) = \begin{cases} 1: & \text{if } \left|\sqrt{gk} + k_x u_x + k_y u_y - \omega(k)\right| \leq \Delta\omega/2 \\ 0: & \text{otherwise.} \end{cases} \tag{2.26}$$

The normalized scalar product $V(u_x, u_y)$ is a function of velocity components, u_x, and u_y, and is defined as

$$V(u_x, u_y) = \frac{\langle |I(k_x, k_y, \omega)|, G(k_x, k_y, \omega, u_x, u_y) \rangle}{\sqrt{P_E \cdot P_G}} \tag{2.27}$$

where P_E and P_G are the power associated with the image spectrum $|I(k_x, k_y, \omega)|$ and $G(k_x, k_y, \omega, u_x, u_y)$:

$$P_E = \frac{\sum_{-k_{xmax}}^{k_{xmax}} \sum_{-k_{ymax}}^{k_{ymax}} \sum_{-\omega_{max}}^{\omega_{max}} (|I(k_x, k_y, \omega)|)^2}{N_x N_y N_t} \tag{2.28}$$

$$P_G = \frac{\sum_{-k_{xmax}}^{k_{xmax}} \sum_{-k_{ymax}}^{k_{ymax}} \sum_{-\omega_{max}}^{\omega_{max}} (|G(k_x, k_y, \omega, u_x, u_y)|)^2}{N_x N_y N_t} \tag{2.29}$$

where N_x, N_y are the number of pixels of the sub-image in the x and y directions, respectively. N_t is the number of frames of the image sequence used for Fourier analysis. By searching for optimal values of the velocity components that maximizes the normalized scalar product in (2.27), the near-surface current information can be obtained.

In order to derive accurate current information, the NSP method requires a large search range and a fine resolution of the velocity in the x and y directions for finding the maximized normalized scalar product. Thus, a large number of computations (thousands of seconds) are usually expected in this method. To reduce the computational cost of this method, an improvement is suggested using variable search ranges and resolutions [87] as follows:

1. Search for an approximate estimation of the current velocity (u_{x_0}, u_{y_0}) with a wide search range $[-U_0, U_0]$ and a coarse resolution Δu_0.

2. Search for the optimal velocity components (u_{x_i}, u_{y_i}) with a narrowed range near the velocity (u_{x_0}, u_{y_0}) derived in Step 1. $(u_{x_i} \in [u_{x_0} - m\Delta u_0, u_{x_0} + m\Delta u_0], u_{y_i} \in [u_{y_0} - m\Delta u_0, u_{y_0} + m\Delta u_0])$ and a higher search resolution Δu_i, where m (= 1 or 2) is the coefficient used to determine the search scope around the previously derived velocity.

3. Replace (u_{x_0}, u_{y_0}) with (u_{x_i}, u_{y_i}) and Δu_0 with Δu_i, and repeat Step 2 until a satisfactory result is found.

It has been found numerically that satisfactory results of the optimal velocity components will be derived after iteratively updating the search results two or three times in Step 3. In this way, the computational complexity can be significantly reduced.

2.2 3-D FFT-based Wave Information Extraction Algorithm

2.2.1 The Classic Algorithm

As summarized in Section 2.1, the classic 3-D FFT-based wave analysis algorithm, based on [16], [51]-[53], will be provided in detail in this section:

Sub-image acquisition and image normalization

Radar images obtained from typical field installations are usually of a large size and not suitable for direct three-dimensional Fourier analysis due to the large computational burden which would be required. Therefore, to efficiently extract wave information it is suggested that Fourier analysis be performed on a carefully selected sub-area instead of the whole radar image. Reichert [92] reported the azimuthal dependence of the backscatter imaged by nautical radar on the wind direction. Also, Nieto Borge *et al.* [51] observed a distortion of wave fronts for positions close to the antenna due to tilt modulation. Of course, the intensity of the back-scattered energy is inversely proportional to the fourth power of the distance between the radar and the target [42]. Therefore, it is not practical to select the sub-image position either too close to or too far away from the antenna. The selection of sub-images for Fourier analysis is

examined and tested in [38]-[1]. In this thesis, a series of radar images are simulated with a size of 512 × 512 pixels and a resolution of 10.5 m/pixel. The radar antenna is assumed to be at the center of the image. Sequences of 32 consecutive sub-images with a dimension of 128 × 128 pixels are acquired in the wave propagation direction with a distance of $200 - 800$ m from the radar antenna as shown in Fig. 2.4. (It may be noted that in Section 4.2 where field data is tested, sub-images with this same size are selected close to the wave buoy, which is 1239.5 m from the radar (see Fig. 4.32)).

After acquiring the series of sub-images, it is necessary to normalize the sequence so as to eliminate the contributions of the static patterns in space and time present in the data set [51]. If the image intensity at position (x, y) at time t is defined as $s(x, y, t)$, the mean intensity $\overline{s}_t(x, y)$ can be easily calculated from the image series. By subtracting this mean intensity from the sub-image series (see Fig. 2.5), a normalized image sequence is obtained and may be written as:

$$s_n(x, y, t) = s(x, y, t) - \overline{s}_t(x, y) \tag{2.30}$$

Three dimensional Fourier analysis

After performing the 3-D Fourier analysis on the normalized image sequence, a complex spectrum $F(k_x, k_y, \omega)$ is derived. Spatial frequencies (k_x, k_y) reflect the space-wavenumber transform from the space domain (x, y), while angular frequency ω reflects the time-frequency transform from the time domain t.

According to the Hermitian property (2.20), a real-valued image spectrum $R(k_x, k_y, \omega)$, can be obtained from the complex spectrum as

$$R(k_x, k_y, \omega) = \frac{1}{L_x L_y T_{total}} |F(k_x, k_y, \omega)|^2 \tag{2.31}$$

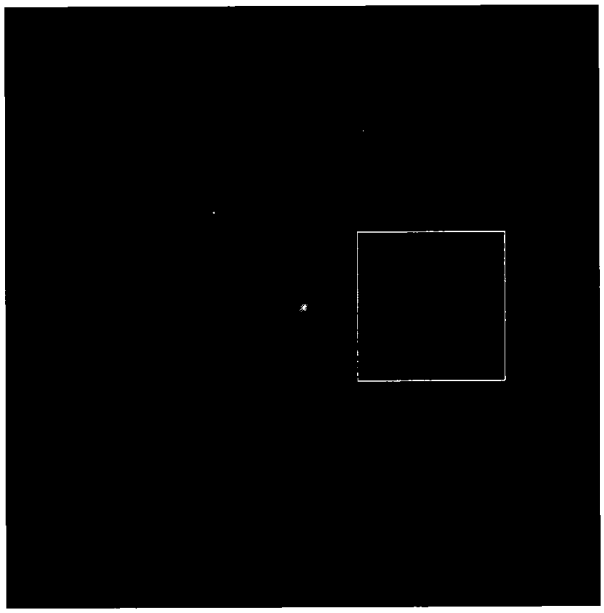

Figure 2.4: Example of sub-image acquisition: a 128 × 128 pixels sub-image is extracted from a 512×512 simulated radar image, at the wave propagation direction 500 m away from the antenna (center of the original image).

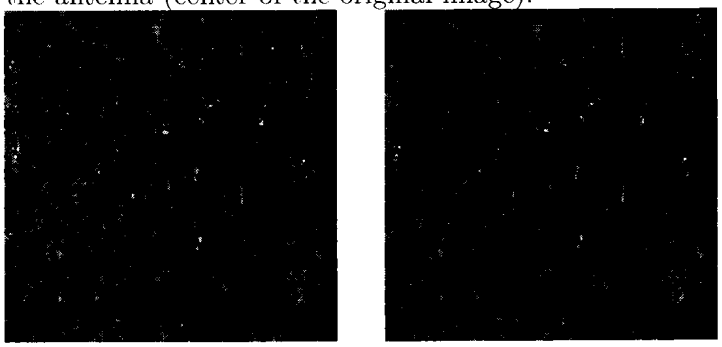

Figure 2.5: Example of image normalization: on the left is the image before image normalization; on the right is the image after normalization.

where T_{total} is the total time duration of a sub-image sequence, and L_x, L_y are the lengths of the sub-image in the x and y directions, respectively [51]-[53].

High-pass filtering

Energy components at very low frequencies are not considered as part of wind or swell wave fields, and thus a high-pass filter is applied to the derived spectrum to eliminate

these non-stationary and non-homogeneous components. The high-pass filter uses an empirical threshold of $\omega_{th} = 2\pi \times 0.03$ rad/s [51] and is written as

$$H(\vec{k},\omega) = \begin{cases} 0; & \text{if } (\vec{k},\omega) \in \Omega_F, \\ 1; & \text{otherwise} \end{cases} \tag{2.32}$$

where Ω_F, the spectral stop-band regulated by the threshold (as shown in Fig. 2.6), is given by

$$\Omega_F \equiv \{\vec{k} \in |\vec{k}| \leq k(\omega_{th})\} \times [-\omega_{th}, \omega_{th}] \tag{2.33}$$

with $k(\omega_{th})$ being the wavenumber solution of the still water dispersion relationship (2.4) for the given ω_{th} [51]-[53].

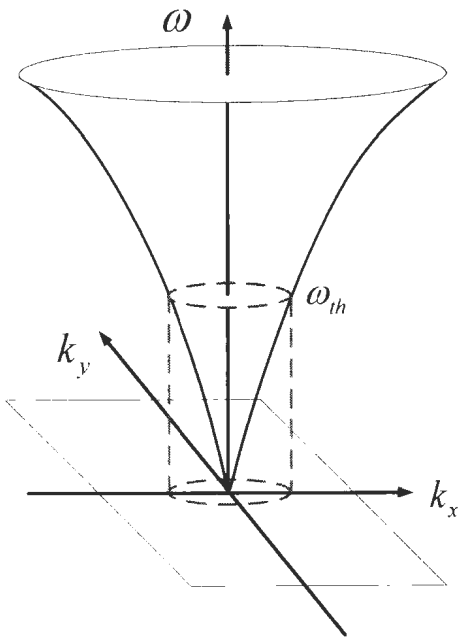

Figure 2.6: High-pass filter; the cylinder represents the stop-band.

The high-passed image spectrum is obtained by applying the high-pass filter to

the 3-D spectrum:

$$I(k_x, k_y, \omega) = H(k_x, k_y, \omega) \cdot R(k_x, k_y, \omega) \tag{2.34}$$

Current estimation

Once the high-passed image spectrum is obtained, near-surface current information can be estimated, as discussed in Section 2.1. In this thesis, the iterative LS method is selected for use in the wave field analysis algorithm for FFT-based wave information extraction.

Band-pass filtering

After obtaining the sea surface current information, a band-pass filter is constructed based on the Doppler-shifted dispersion shell (1.1) to remove the spectral energy due to non-wave contributions. In [17], the band-pass filter is described as

$$I_{bapa}(\vec{k}_{mn}, \omega_{i_r}) = \begin{cases} I((-1)^r \vec{k}_{mn}, \omega_i), & \Delta_{i_r} k \leq \delta k_{i_r}, \\ 0, & \text{otherwise} \end{cases} \tag{2.35}$$

where

$$\delta k_{i_r} = \left| \vec{k}(\omega_{i_r+1}) \right| - \left| \vec{k}(\omega_{i_r-1}) \right| \tag{2.36}$$

$$\Delta_{i_r} k \equiv \left| (-1)^r \vec{k}_{mn} - \vec{k}(\omega_{i_r}) \right| \tag{2.37}$$

In (2.35), $I(\vec{k}_{mn}, \omega_i)$ is the high-pass filtered image spectrum for the sampled wave vector $\vec{k}_{mn}$ and frequency ω_i. $\omega_{i_r} \in [r\omega_N, (r+1)\omega_N]$ is the back-folded frequency with integer number $r \in [-3, 2]$. δk_{i_r} is the pass-band and $\Delta_{i_r} k$ is the magnitude of the vector difference between the sampled wave vector $\vec{k}_{mn}$ and the calculated wave vector $\vec{k}(\omega_{i_r})$ (see Fig. 2.7).

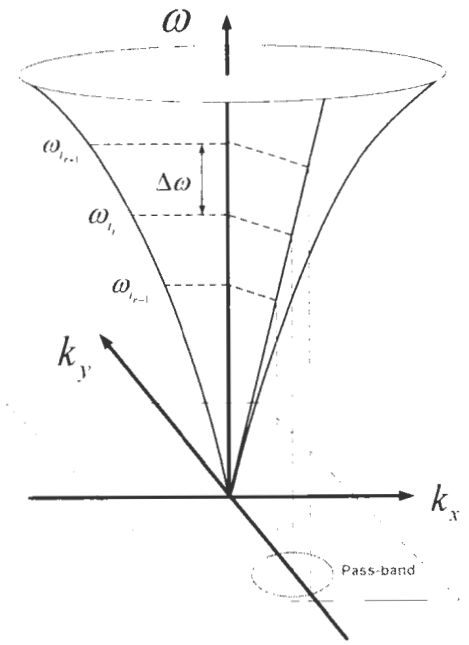

Figure 2.7: Band-pass filter: the circle represents the pass-band.

Modulation Transfer Function (MTF)

Due to the radar imaging mechanisms such as shadowing and tilt modulation as well as the non-linearity of the wave field, a non-linear difference can be observed between the spectra derived from the radar image and those from the *in situ* records for the case of grazing incidence. This difference can be minimized by introducing a modulation transfer function (MTF) into the algorithm [23], [36].

In [32], the modulation transfer function is defined as

$$|M(k)|^2 = E_b(k)/I_r(k) \tag{2.38}$$

where $I_r(k)$ is the 1-D wavenumber spectrum derived from the radar data and $E_b(k)$ is the wavenumber spectrum derived from the buoy records. A series of field data tests

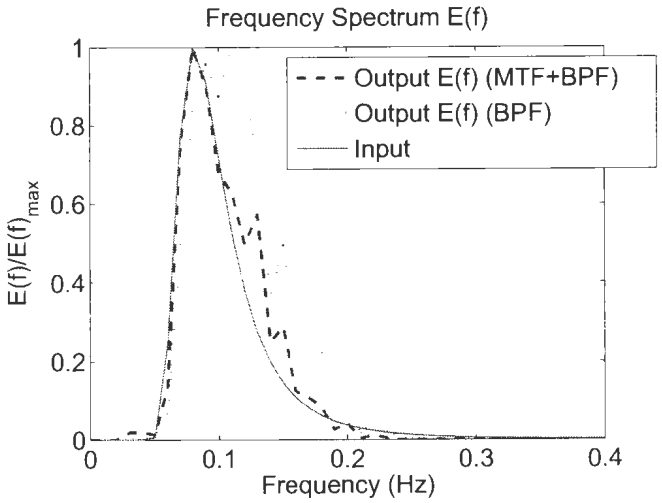

Figure 2.8: Comparisons of the input and derived spectra $E(f)$ with/without MTF.

were conducted in [32] using a WaMos II radar system and a pitch-roll WaveScan buoy to determine $|M(k)|^2$. After analyzing the collected data, a power decay law given by

$$|M(k)|^2 = \vec{k}^{\mu} \tag{2.39}$$

was determined for the modulation transfer function. In that research, a mean value of $\bar{\mu} = -1.2$ was empirically determined and was later used in many data tests [51]-[53]. However, different μ values should be determined for different wave analysis algorithms (FFT/CWT) via data test calibrations and curve fittings (see Chapter 4).

Fig. 2.8 shows the comparisons of the input (solid line) and derived frequency spectra $E(f)$ without the use of the MTF (dot line) and the spectrum when the MTF is incorporated (dash line). It is observed from Fig. 2.8 that the wave spectrum derived using the MTF agrees better with the input spectrum. Two peaks are also seen on the spectrum derived without the MTF. This leads to produces large errors in the calculation of peak frequency and period. In addition, the retrieved spectrum deviates significantly from the input in the high frequency band if the MTF is not

used.

Derivations of Wave Spectra and Parameters

After the band-pass filtering and MTF process, a 2-D wave spectrum can be derived as

$$E(k_x, k_y) = \left|\vec{k}\right|^{\mu} I(k_x, k_y) \tag{2.40}$$

where $I(k_x, k_y)$ is the 2-D image spectrum after the band-pass filtering.

The wavenumber-direction spectrum $E(k, \theta)$ and frequency-direction spectrum $E(\omega, \theta)$ are then determined from $E(k_x, k_y)$ via the form

$$E(k, \theta) = E(k_x, k_y)\frac{dk_x dk_y}{dk d\theta} = E(k_x, k_y) \cdot \left|\vec{k}\right| \tag{2.41}$$

$$E(\omega, \theta) = E(\vec{k}, \theta)\frac{dk}{d\omega}. \tag{2.42}$$

The 1-D frequency spectrum $E(\omega)$ is obtained by integrating the 2-D frequency-direction spectrum $E(\omega, \theta)$ over the interval $[0, 2\pi]$

$$E(\omega) = \int_0^{2\pi} E(\omega, \theta) d\theta \tag{2.43}$$

From the 1-D frequency spectrum, the spectral moment can be calculated as

$$m_n = \int_0^{f_N} f^n E(f) df \tag{2.44}$$

where f_N is the Nyquist frequency.

Also, according to research from the IAHR working group [21], the peak frequency

can be calculated by Delft's method as

$$f_p = \frac{\int_{f_1}^{f_2} fE(f)df}{\int_{f_1}^{f_2} E(f)df} \tag{2.45}$$

where f_1 and f_2 are the lowest and highest frequencies at which

$$E(f) = 0.8 \max\{E(f)\}. \tag{2.46}$$

The mean period, obtained from the spectral moments m_0 and m_1, is given as

$$T_{01} = 2\pi \frac{m_0}{m_1}. \tag{2.47}$$

Mean wave direction is a function of frequency, written as

$$\theta(f) = \text{atan}(b(f)/a(f)) \tag{2.48}$$

where a and b are the directional Fourier coefficients [52]. If f_c is the cut-off frequency, overall mean wave direction θ_w is then determined by averaging the mean wave direction over all frequency components $f \in [0, f_c]$, written as

$$\theta_w = \text{atan}\left(\frac{\int_0^{f_c} \int_{-\pi}^{\pi} E(f,\theta)k(f)\sin\theta d\theta df}{\int_0^{f_c} \int_{-\pi}^{\pi} E(f,\theta)k(f)\cos\theta d\theta df}\right) \tag{2.49}$$

2.2.2 Enhanced Algorithm with Modified Band-Pass Filter

In the classic 3-D FFT algorithm, the band-pass filter is designed based on the Doppler-shifted dispersion relationship to eliminate the aliasing effects via a back-folding strategy [17]. However, the fundamental, harmonic wave components and noise that fall in the pass-band are all used for derivation of the wave spectra and

wave parameters. The contributions of noise and higher order wave components may lead to less accurate wave spectra and related parameters. In order to remove the contributions from these undesired components, an enhanced algorithm with a modified band-pass filter involving only the fundamental mode wave components is designed in this thesis (see also [93], [94]). This is accomplished based on the mode classification results obtained from the iterative least squares current estimation algorithm proposed by Senet *et al.* [47].

Based on a series of data tests, it is determined that $\omega_p(\vec{k}) \in [-\omega_N, 3\omega_N]$ can be used to retrieve accurate near-surface current information in the iterative LS process. Due to a low sampling frequency, aliasing effects occur and fold the sample points from $[-\omega_N, 3\omega_N]$ into $[0, \omega_N]$. Therefore, it is desirable to identify the aliased sample points and fold these components $\omega_p(\vec{k}) \in [-\omega_N, 3\omega_N]$ to $\omega_{p,r}(\vec{k}_{i'}) \in [0, \omega_N]$ before mode classification.

By determining the range of $\omega_p(\vec{k}_{i'})$ and $\omega_p(-\vec{k}_{i'})$ using (2.17), $\omega_{p,r}(\vec{k}_{i'})$ is calculated as follows:

1. if $\omega_p(\vec{k}_{i'}) \in [n\omega_N, (n+1)\omega_N]$, where $n = 0, 2$, $\omega_{p,r}(\vec{k}_{i'}) = \omega_{p,n}(\vec{k}_{i'}) = \omega_p(\vec{k}_{i'}) - n\omega_N$;

2. if $\omega_p(-\vec{k}_{i'}) \in [m\omega_N, (m+1)\omega_N]$, where $m = -1, 1$, $\omega_{p,r}(\vec{k}_{i'}) = \omega_{p,m}(-\vec{k}_{i'}) = -\omega_p(-\vec{k}_{i'}) + (m+1)\omega_N$;

3. otherwise, this point is discarded.

Once all the possible frequencies $\omega_p(\vec{k}_{i'})$ and $\omega_p(-\vec{k}_{i'})$ are folded to $\omega_{p,r}(\vec{k}_{i'}) \in [0, \omega_N]$, mode classification is performed by comparing the difference between the folded frequencies and the sample frequency $\omega_{i'}$ via minimization as follows:

$$MIN(|\omega_{i'} - \omega_{0,n}(\vec{k}_{i'})|, \quad |\omega_{i'} - \omega_{1,n}(\vec{k}_{i'})|, \\ |\omega_{i'} - \omega_{0,m}(-\vec{k}_{i'})|, \quad |\omega_{i'} - \omega_{1,m}(-\vec{k}_{i'})|) \tag{2.50}$$

Meanwhile, the order of the harmonics and the range of each sample point are indicated with a flag $F_i(p, r)$ to enable back-folding of the sample points $\omega_{i'} \in [0, \omega_N]$ to $\omega_{i_r} \in [-\omega_N, 3\omega_N]$ for refining the band-pass filter (2.35). During the back-folding process, only the points of the fundamental mode ($p = 0$) that fall in the pass-band of the filter in (2.36) are kept for wave information extraction. That is, the ($p \neq 0$) contributions are discarded. In this way, fundamental mode contributions are retained and used as filter inputs in order to derive more accurate band-passed spectra.

Chapter 3

2-D Wavelet-based Algorithm for Wave Measurement

In the previous chapter, the classic 3-D FFT-based wave analysis algorithms for ocean wave and current information retrieval are presented. In this chapter, an alternative strategy in which a 2-D continuous wavelet transform (CWT) is applied to a single frame of the nautical radar image to extract ocean wave information is presented. The theory of the 2-D wavelet transform is first reviewed. Next, the application of the 2-D CWT for wave field analysis is discussed. This includes the selection and simplification of a mother wavelet, discretization and sampling of the wavelet function for radar image processing, and the determination and calibration of the required wavelet parameters.

3.1 2-D Wavelet Transform and Its Application for Wave Field Analysis

3.1.1 2-D Wavelet Transform

As stated in [77]-[81], the 2-D wavelet transform (WT) decomposes a signal into a series of wavelets which are scaled, shifted, and rotated versions of the so-called mother wavelet (see Fig. 3.1). If an image is given as $s(\vec{\gamma}) = s(x, y)$, where s and $\vec{\gamma} = (x, y)$ represent the intensity of the pixel and its coordinates in the image, respectively, its 2-D WT, W, may be defined as [78], [79]

$$W(\vec{b}, \theta, a) = C_{\Psi}^{-1/2} a^{-1} \cdot \int_{R^2} \Psi^*(a^{-1} r_{-\theta}(\vec{\gamma} - \vec{b})) s(\vec{\gamma}) d^2\vec{\gamma}. \tag{3.1}$$

Here $\vec{b} = (b_x, b_y)$ is a shifting parameter that indicates the shifted position of the wavelet in the space domain; a is a non-dimensional scaling parameter that is related to the dilated spatial frequency (wavenumber) of the space domain, while a^{-1} normalizes all the dilated wavelets to equalize their energy; and Ψ^* is the complex conjugate of the mother wavelet function Ψ. θ is a rotation factor which defines a rotation matrix $r_{-\theta}$ that rotates the wavelet by angle θ in the space domain. This rotation matrix may be written as [79]

$$r_{-\theta} = \begin{pmatrix} \cos\theta & \sin\theta \\ -\sin\theta & \cos\theta \end{pmatrix} \tag{3.2}$$

where $0 \leq \theta < 2\pi$. Finally, to guarantee the invertibility of the WT, the normalization constant, C_{Ψ}, must satisfy the admissibility condition as found in [79]

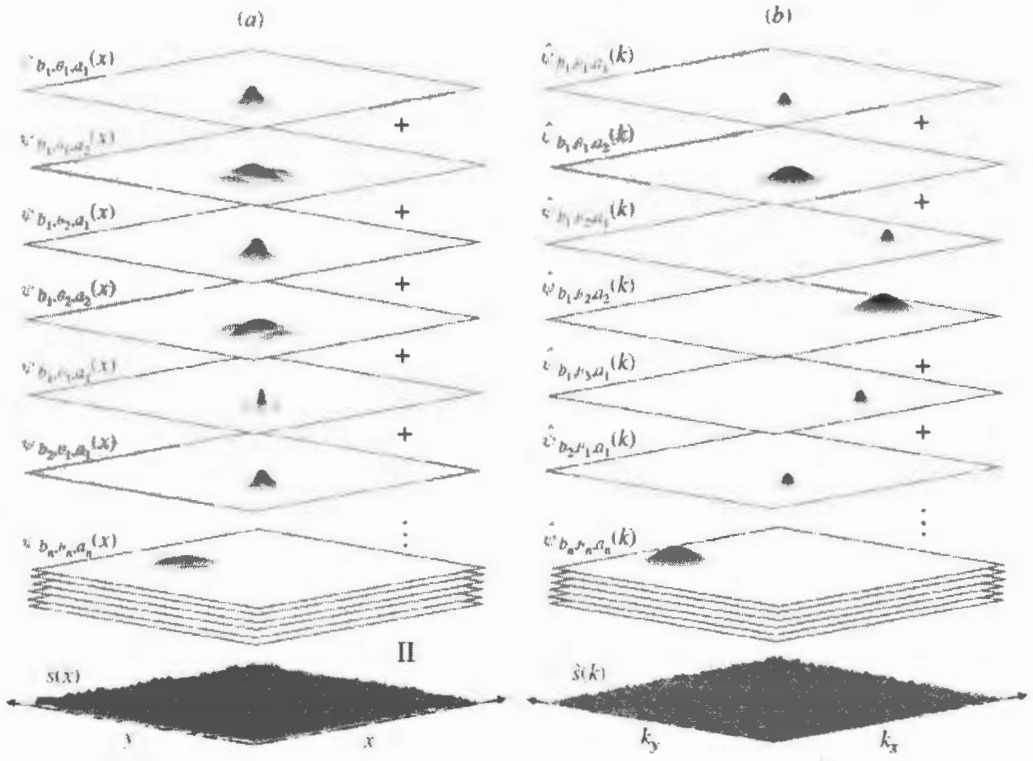

Figure 3.1: Decompositions of a signal into various wavelets in (a) the space domain and (b) spatial frequency domain (taken from Wu *et al.* [79]).

3.1.2 2-D CWT for Radar Image Processing

The selection of the mother wavelet

The mother wavelet function Ψ in (3.1) needs to be specified before the wavelet transform. The extraction of ocean wave parameters and the directional frequency spectrum requires the specification of a directional mother wavelet [79]. Here, the Morlet wavelet, which can be considered as a band-pass filter with an adjustable pass-band, is chosen as the mother wavelet [75], [79]. In the space domain and spatial frequency domain, the Morlet wavelet function can be written as [79]

$$\Psi(\vec{\gamma}) = e^{-0.5|A\vec{\gamma}|^2} e^{i\vec{k}_0 \cdot \vec{\gamma}} - e^{-0.5|A\vec{\gamma}|^2} e^{-0.5\left|A^{-1}\vec{k}_0\right|^2} \tag{3.3}$$

and its FT is

$$\hat{\Psi}(\vec{k}) = \sqrt{\epsilon}[e^{-0.5|A^{-1}(\vec{k}-\vec{k}_0)|^2} - e^{-0.5|A^{-1}\vec{k}_0|^2} e^{-0.5|A^{-1}\vec{k}|^2}] \tag{3.4}$$

Here, $\vec{\gamma}$ is the coordinate in the space domain. $A = \text{diag}[\epsilon^{-0.5}, 1], (\epsilon \geq 1)$ is a 2×2 anisotropic diagonal matrix [78], and the vector $\vec{k}_0 = (k_{0_x}, k_{0_y})$ controls the peak position of the wavelet function. The second term of the Morlet wavelet function in (3.3) and (3.4) is considered as a correction term and it is negligible for $|\vec{k}_0| \geq 5.6$ [78]. Furthermore, it is discussed in [78] that the mother wavelet can be considered as a band-pass filter and the pass-band becomes narrower as ϵ increases.

In [79], the mother wavelet of equation (3.4) was simplified for the purpose of radar image processing by adopting $\vec{k}_0 = (6, 0)$ and $\epsilon = 1$, which enables $\hat{\Psi}(\vec{k}) = \hat{\Psi}(k_x, k_y)$ to be symmetrical in the x and y directions. In the space domain and spatial frequency domain, the simplified mother wavelet can be written as

$$\Psi(\vec{\gamma}) = e^{-0.5\,\gamma^2} e^{i\vec{k}_0\vec{\gamma}} \tag{3.5}$$

and

$$\hat{\Psi}(\vec{k}) = e^{-0.5|\vec{k}-\vec{k}_0|^2}. \tag{3.6}$$

Equations (3.6) and (3.5) are also known as Gabor functions [95], which are widely used in image processing. This is because the functions can be used to model the perceptive field of primates' primary visual cortex. Also, these simplified functions significantly reduce the computational complexity in the wavelet analysis [78]. Fig. 3.2 illustrates the real and imaginary part of the simplified Morlet wavelet (Gabor) function $\Psi(\vec{\gamma})$ in the space domain. Fig. 3.3 shows the simplified Morlet wavelet (Gabor)

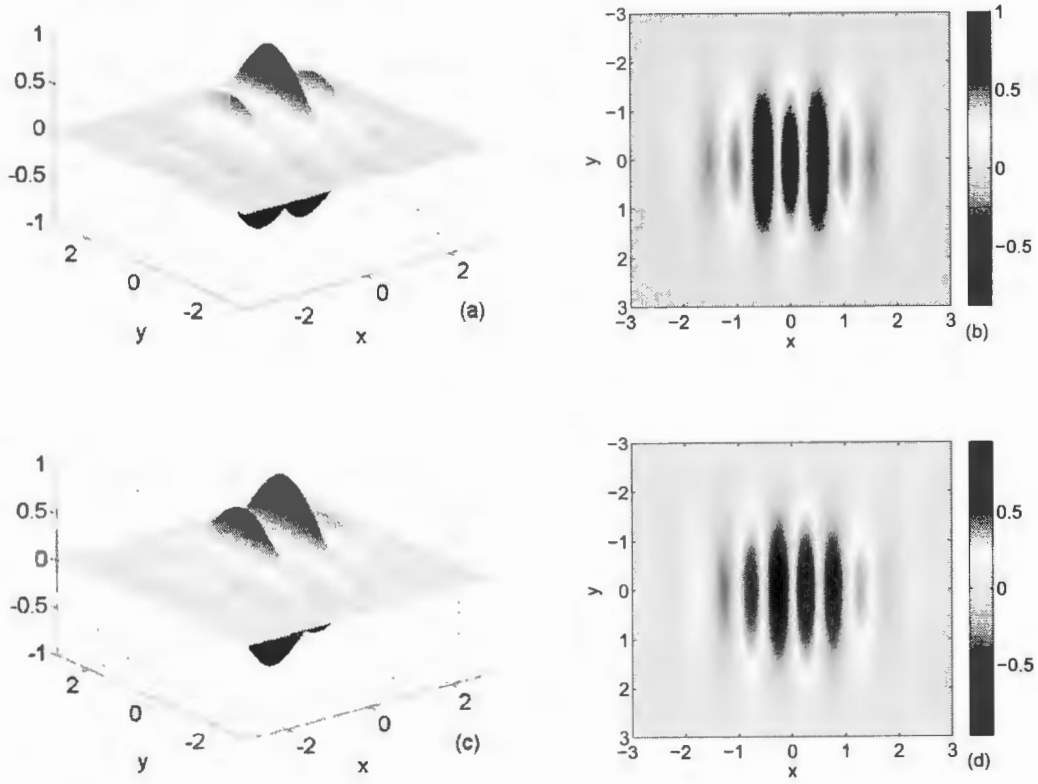

Figure 3.2: Gabor function $\Psi(\vec{\gamma})$: (a) real part in 3-D perspective; (b) real part in 2-D intensity plot; (c) imaginary part in 3-D perspective; (d) imaginary part in 2-D intensity plot

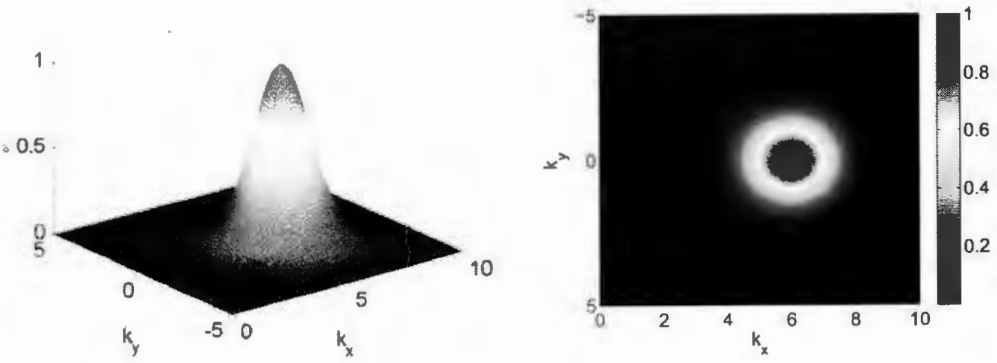

Figure 3.3: Gabor function $\hat{\Psi}(\vec{k})$ in the spatial frequency domain. The energy peak is located at $(k_x, k_y) = (6, 0)$.

function $\hat{\Psi}(\vec{k})$ in the spatial frequency domain.

Configurations of the 2-D CWT for radar image processing

In order to apply the selected non-dimensional continuous Morlet wavelet function to dimensional digital radar image analysis, the 2-D CWT function requires the process of both discretization and sampling. First, the continuous wavelet function in (3.1) can be rewritten discretely in the form [79]

$$W(b_{x_u}, b_{y_v}, \theta_m, a_n) = C_\Psi^{-0.5} a_n^{-1} \sum_{p=1}^{N_x} \sum_{q=1}^{N_y} \cdot \Psi^*[a_n^{-1} r_{-\theta_m}(x_p - b_{x_u}, y_q - b_{y_v})] \\ s(x_p, y_q)\Delta x \Delta y \qquad (3.7)$$

with W being a function of the discrete shifting (b_{x_u}, b_{y_v}), rotation (θ_m), and scaling factors (a_n); (x_p, y_q) are the sample points on the radar image; the subscripts u, v, m, n, p, and q are the discretization indices; N_x and N_y are the total sampling numbers in the x and y directions of the image; and Δx, Δy are the radar image resolutions in the x and y directions, respectively. Equation (3.7) is computationally intensive. To reduce the algorithm execution time, it is desirable to perform the CWT in the spatial frequency domain (the Fourier space). This converts the convolutions into multiplications [79], with the result written as

$$W(b_{x_u}, b_{y_v}, \theta_m, a_n) = C_\Psi^{-0.5} a_n \sum_{p=1}^{N_{k'_x}} \sum_{q=1}^{N_{k'_y}} e^{i(b_{x_u} k'_{x_p} + b_{y_v} k'_{y_q})} \cdot \hat{\Psi}^*[a_n r_{-\theta_m}(k'_{x_p}, k'_{y_q})] \\ \hat{s}(k'_{x_p}, k'_{y_q})\Delta k'_x \Delta k'_y \qquad (3.8)$$

where $\hat{s}$ is the Fourier transform of the image intensity s, and "$*$" indicates complex conjugation. As previously mentioned, $\vec{k} = (k_x, k_y)$ is the wave vector in non-dimensional space, and after the wavelet transform, $\vec{k'} = (k'_x, k'_y)$ is the wave vector in

dimensional space, where $k'_x \in [-\frac{N_{k'_x}}{2}\Delta k'_x, \frac{N_{k'_x}}{2}\Delta k'_x]$ and $k'_y \in [-\frac{N_{k'_y}}{2}\Delta k'_y, \frac{N_{k'_y}}{2}\Delta k'_y]$, with (k'_{x_p}, k'_{y_q}) indicating the sampled components of $\vec{k'}$. $N_{k'_x}$ and $N_{k'_y}$ are total numbers of the sampled wavenumber in the x and y directions, respectively. Usually $N_{k'_x} = N_x$ and $N_{k'_y} = N_y$ [79]. $\Delta k'_x$ and $\Delta k'_y$ are the wavenumber resolutions in the dimensional spatial frequency domain, written as [79]

$$\Delta k'_x = \frac{2\pi}{N_x \Delta x} \tag{3.9}$$

$$\Delta k'_y = \frac{2\pi}{N_x \Delta y}. \tag{3.10}$$

In (3.8), it is observed that the transformed wavelet can be obtained by scaling, shifting, and rotating the mother wavelet. After dilation and rotation with parameters a and $r_{-\theta}$, respectively, the corresponding peak wave vector in dimensional space is $\vec{k'}$ which satisfies

$$\vec{k_0} = a r_{-\theta}(\vec{k'}) \ . \tag{3.11}$$

From equations (3.2) and (3.11)

$$k_{0_x} = a(k'_x \cos\theta + k'_y \sin\theta) \tag{3.12}$$

$$k_{0_y} = a(-k'_x \sin\theta + k'_y \cos\theta) \tag{3.13}$$

Therefore, the 2-D CWT, $W(b_x, b_y, \theta, a)$, can be written as a function of the shifting factor $\vec{b} = (b_x, b_y)$ and transformed wave vector $\vec{k'}$. Once the shifting factor is specified as $\vec{b_0}$, a 2-D wavenumber spectrum $W(\vec{k'})$ at point $\vec{b_0}$ is determined as

$$W(b_x, b_y, \theta, a) \rightarrow W(\vec{b}, \vec{k'}) \xrightarrow{\vec{b_0}} W(\vec{k'}). \tag{3.14}$$

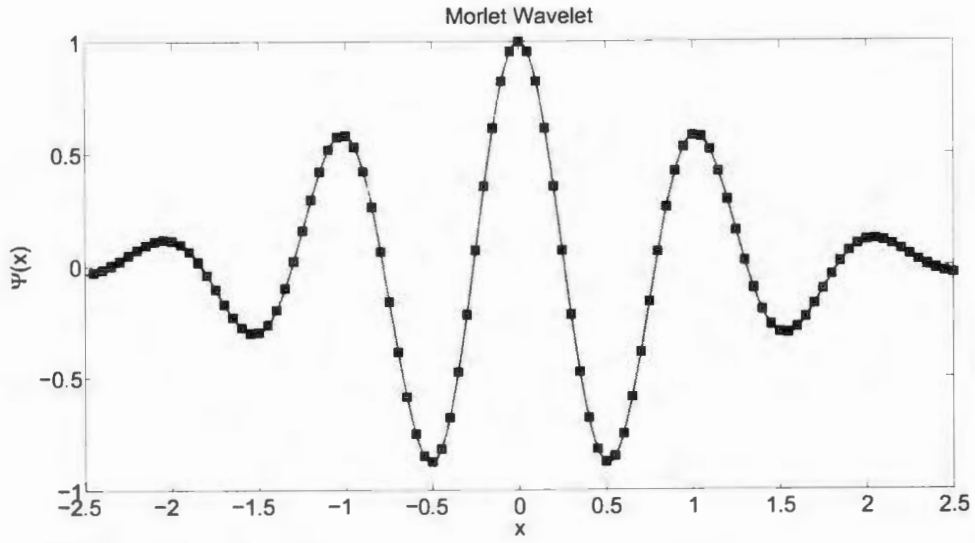

Figure 3.4: Sampling of the wavelet function: $[-D, D] \leftrightarrow [0, N_s\Delta x]$. $2D$ is the length in non-dimensional space; $N_s\Delta x$ is the length in dimensional space.

The derived image spectrum $W(\vec{k'})$ is dimensional. Thus, $\hat{\Psi}^*$ in (3.8) needs to be sampled, and this process converts the non-dimensional wavelet into a dimensional one. As discussed earlier in this section, the matrix $r_{-\theta}$ is applied to control the direction of the wavelet function and k_{0_y} is set to zero so that k_{0_x} controls the peak spatial frequency in the spatial frequency domain [79]. The sampling process and the determination of the corresponding wavelet factors may be simply conducted on the k_x axis, where the rotation angle $\theta = 0$. In the space domain, if the sampling resolution is Δx m and the total number of sample points is N_s, the total length to be transformed by the mother wavelet used for image analysis in dimensional space is simply $X' = N_s\Delta x$ m. If the total length of the mother wavelet in non-dimensional space is $X = 2D$, this non-dimensional mother wavelet is mapped into N_s points during the sampling process (see Fig. 3.4). This may be formally represented as [75], [80]

$$[-D, D] \leftrightarrow [0, N_s\Delta x] \,. \tag{3.15}$$

The non-dimensional length of the mother wavelet can be determined as

$$2D = 2 \times 3.5\sigma_x \tag{3.16}$$

where σ_x is the standard deviation given in [75] as

$$\sigma_x = (\int_{-\infty}^{\infty} (x - x_0)^2 \left|\Psi(x)\right|^2 dx)^{1/2} \tag{3.17}$$

with the peak position x_0 on the x axis of the space domain being given by

$$x_0 = \frac{\int_{-\infty}^{\infty} x \left|\Psi(x)\right|^2 dx}{\int_{-\infty}^{\infty} \left|\Psi(x)\right|^2 dx}. \tag{3.18}$$

The minimum number of sample points can be calculated in terms of the Morlet wavelet's non-dimensional length as [75]

$$N_s = \frac{2D}{\pi}(k_{0_x} + \sqrt{-2\ln(\eta)}) \tag{3.19}$$

where η is a parameter defined in [75] as

$$\eta = \frac{\left|\hat{\Psi}(k_{c_x})\right|}{\left|\hat{\Psi}(k_{0_x})\right|}. \tag{3.20}$$

Equation (3.20) indicates that η is the ratio of the wavelet value at the cut-off wavenumber k_{c_x} and that at the peak wavenumber k_{0_x}, and the value of η is commonly set to 0.01 by Chung *et al.* in [79], [80].

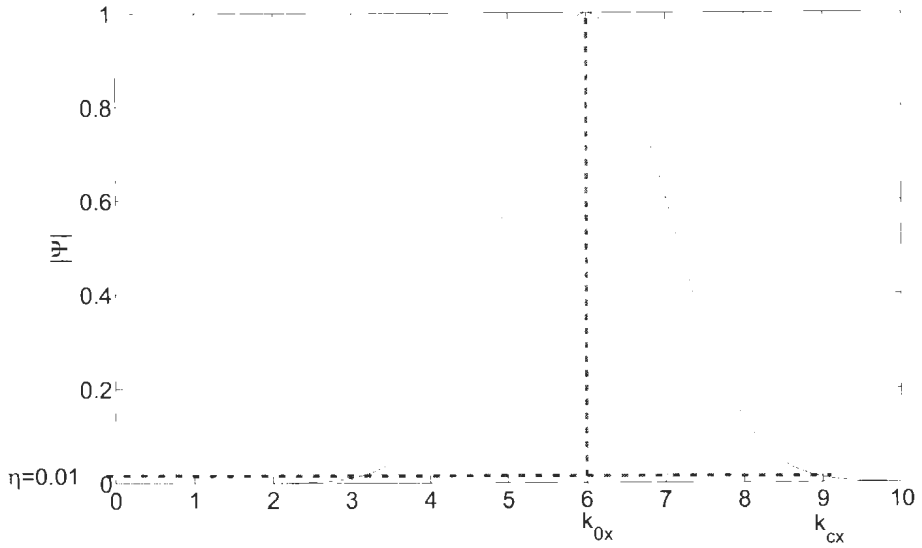

Figure 3.5: The selection of η

3.2 The Discussion of the Scaling Factor and 2-D CWT Wave Algorithms

In order to obtain the wave field spectrum from the wavelet analysis as indicated in (3.8) and (3.14), wavelet parameters $\vec{b}$, θ, and a need to be specified. In an earlier section, the determination of the shifting and rotating factors have been discussed. In this section, the selection of the scaling factor for wavelet analysis will be explored in more detail.

3.2.1 The Discussion of the Scaling Factor

In [96], the relationship of the scaling factor and the desired wavenumbers is deduced based on the assumption that the scaling factor, a_n, takes the form of a geometric progression [75] and is related to the range of the wave spectrum. From (3.9) and (3.10), it may be observed that the spatial frequencies are inversely proportional to

the total lengths of the radar image in the x and y directions. With $\theta = 0$, it can be shown from (3.11) and (3.15) that

$$\frac{k_{0_x}}{[a_n(k'_x\cos 0 + k'_y \sin 0)]} = \frac{1/X}{1/X'} = \frac{N_s \Delta x}{2D} \tag{3.21}$$

Therefore, the expression of the sampled wavenumber in dimensional space is written as

$$k'_x = \frac{2Dk_{0_x}}{a_n N_s \Delta x}. \tag{3.22}$$

The scaling factor a_n is obviously determined from (3.22) to be

$$a_n = \frac{2Dk_{0_x}}{N_s \Delta x k'_x} \tag{3.23}$$

Given that the sampled wavenumber range of the image spectrum on the k_x axis is

$$|k'_x| = 0, \Delta k'_x, 2\Delta k'_x, ..., \frac{N_x}{2}\Delta k'_x \ . \tag{3.24}$$

the maximum value of the scaling factor can be determined by considering (3.22) with k'_x set to a minimum value given as

$$k_{x'_{min}} = \beta \Delta k'_x \tag{3.25}$$

with k_{0_x} set to a value of 6. Clearly, the maximum value of a_n may then be written as

$$a_{max} = \frac{2D \cdot 6}{N_s \Delta x \beta \Delta k'_x} \tag{3.26}$$

where β is a calibration parameter that regulates the value of a_{max}. Therefore, we conclude that after the sampling process, the minimum distinguishable value of the

wavenumber $k'_{x_{min}}$ of the dimensional spectrum can be specified by an appropriate selection of the maximum scaling factor, or, more specifically, by the selection of the calibration factor β that refines the values of a_{max}.

It is known that with a decreasing mean wave period, T_{01}, the peak frequency (wavenumber) increases and the whole spectrum shifts to larger (spatial) frequency components. In this case, the corresponding minimum distinguishable frequency and wavenumber will keep increasing. Therefore, it is reasonable to assume that if Δx and N_x are fixed, for a sea state with a smaller mean wave period, a larger calibration factor β should be used, as indicated by (3.25). A failure to select an appropriate β may result in a less accurate or completely incorrect derivation of wave spectra and parameters. Fig. 3.6 shows examples of one-dimensional frequency spectra $E(f)$ derived using the 2-D CWT and using different β for simulated radar images with $T_{01} = 10$ s, $\Delta x = 10.5$ m, and $N_x = 128$. It is observed from Fig. 3.6 that the derived spectrum using $\beta = 3.2$ agrees best with the input $E(f)$. If a smaller β of 1.4 is used, a false peak is observed on the left of the spectral peak. If a larger β of 5.4 is used, the derived spectrum is shifted to the right compared with the input $E(f)$. Clearly, the T_{01} derived from the spectra in Fig. 3.6(a) and (c) are less accurate. As indicated in Section 3.1.2, the 2-D CWT analysis in the frequency domain is essentially the sum of a series of band-pass filtered signals. The image function $\hat{s}$ is processed with the modified band-pass filters, which are defined by the transformed wavelet functions. The scaling factors control the bandwidths and peak positions of the wavelet series. In [75], it is observed that the larger the scaling factor, the closer the peak position will be to the origin, as shown in Fig 3.7. Therefore, an underestimated β in (3.26) results in an overestimated a_{max} which generates undesired signals at small frequency components. This results in a redundant energy component (a false peak). On the contrary, an overestimated β will cause missing energy (right-shifted) in the derived

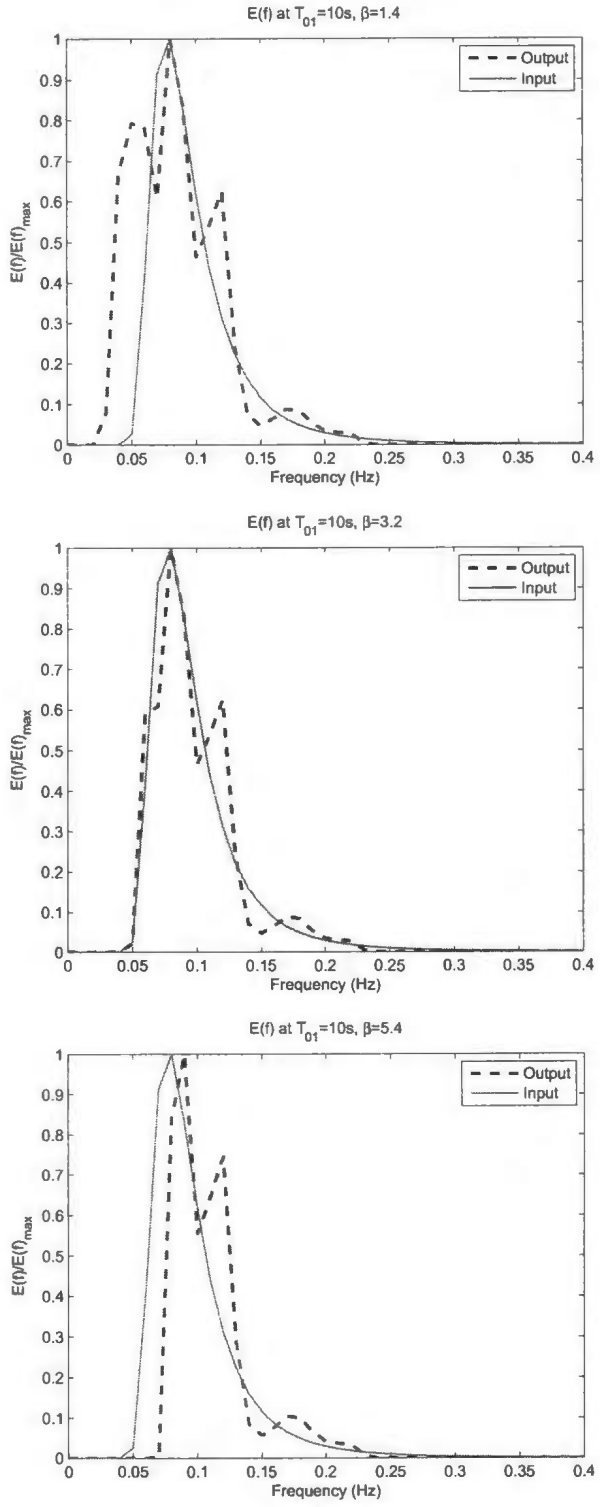

Figure 3.6: An example of CWT derived 1-D spectra E(f) using different β at $T_{01} = 10$ s, $\Delta x = 10.5$ m, $N_x = 128$: (a) $\beta = 1.4$; (b) $\beta = 3.2$; (c) $\beta = 5.4$.

spectrum.

As in [96], based on a series of simulated data tests, the empirical values of β for sea conditions with varying T_{01} are shown in Table 3.1. Here, only the wave fields with typically observed T_{01} are provided. Moreover, the values of β provided in Table 3.1 are obtained at a specific image resolution of $\Delta x = 10.5$ m and sub-image length of $N_x = 128$. According to (3.25), β_n for different Δx_n and N_{x_n} should be modified as

$$\beta_n = \beta \frac{N_{x_n} \Delta x_n}{N_x \Delta x} \tag{3.27}$$

Therefore, once the radar image resolution and the size of the sub-image are provided, an appropriate value of β for the 2-D CWT analysis can be determined from Table 3.1 and (3.27), according to the mean period of the wave field to be examined.

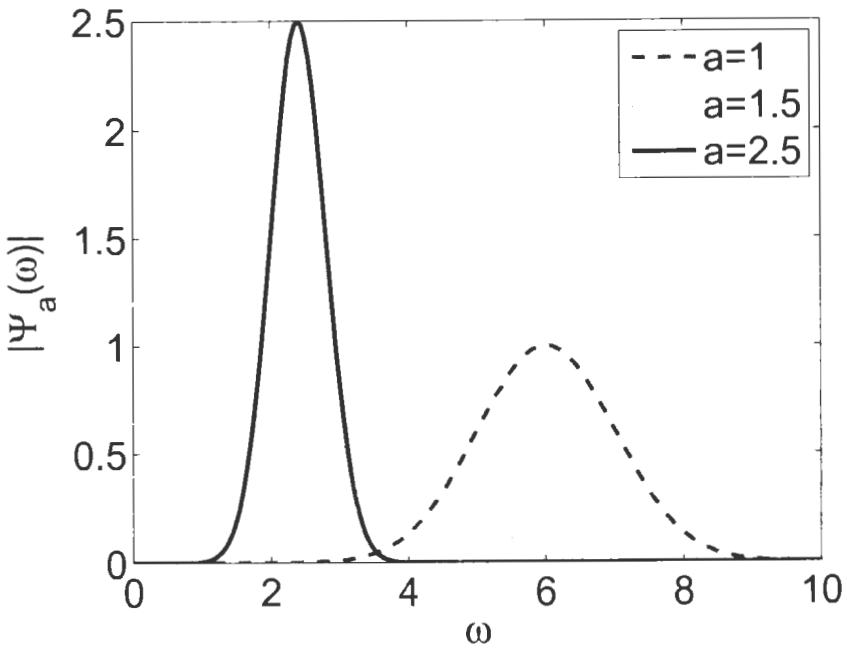

Figure 3.7: Morlet wavelet $|\hat{\Psi}(\vec{k})|$ functions with different scaling factor a. As a increases, the corresponding center frequency decreases (closer to the origin), and the magnitude increases.

Table 3.1: β for Different T_{01} with $\Delta x = 10.5$ m, $N_x = 128$

T_{01} (s)	β
16	1.4-1.6
14	1.7-2.0
13	2.1-2.2
12	2.3-2.4
11	2.5-2.9
10	3.0-3.4
9	3.5-3.9
8.5	4.0-4.5
8	4.5-5.2
7.5	5.2-5.7
7	5.8-6.5
6.5	6.6-7.3
6	7.4-8.4

Knowing a_{max} (or β) is not sufficient to determine all the scaling factors. As previously discussed, the Morlet wavelet in the spatial frequency domain can be regarded as a band-pass filter whose width decreases as the scaling factor increases. It is therefore assumed that a_n takes the form of the geometric progression [75]

$$a_n = M^{n-1}, \quad n = 1, 2, \ldots, N_a \quad (M > 1) \tag{3.28}$$

where $n = 1$ corresponds to the wavelet without dilation (mother wavelet). Thus,

$$a_{min} = a_1 = 1 \ . \tag{3.29}$$

The base M in (3.28) is given as [75]

$$M = \frac{k_{p_1}}{k_d + k_{p_1}} \tag{3.30}$$

where k_{p_1} indicates the peak location of the 1-D wavelet without dilation as in (3.29)

so that

$$k_{p_1} = k_{0_x} = 6, \tag{3.31}$$

and k_d is a proportionality constant which is derived from the scale resolution χ as [75]

$$k_d = -\sqrt{-2\ln(\chi)}. \tag{3.32}$$

The scale resolution $\chi \in (0.0, 1.0)$ is defined in [75] as the ratio of the peak energy of a wavelet with a given scaling factor (a_{n_τ}) to that with the previous scaling factor ($a_{n_{\tau-1}}$), the result being

$$\chi = \frac{\left|\hat{\Psi}_{peak\_a_{n_\tau}}\right|}{\left|\hat{\Psi}_{peak\ \ a_{n_{\tau-1}}}\right|}. \tag{3.33}$$

χ near 1.0 or 0.0 represents a high or low resolution wavelet series, respectively. For ocean wave analysis, it is determined from simulated and field data tests that an appropriate range of this parameter is given by $\chi \in [0.9, 0.95]$.

3.2.2 A Look-up-table-based 2-D CWT Wave Analysis Algorithm

After the 2-D CWT analysis, a complex spectrum of a radar image $W(k'_x, k'_y)$ is obtained. Similar to (2.31), a real-valued image spectrum can be obtained from the Hermitian property (2.20) and written as

$$I(k'_x, k'_y) = \frac{\left|W(k'_x, k'_y)\right|^2}{L_x \cdot L_y} \tag{3.34}$$

where $W(k'_x, k'_y)$ is the complex spectrum derived by the 2-D CWT analysis as stipulated in (3.8), (3.14). L_x, L_y are the total lengths of the radar image in the x and y directions, respectively. Techniques similar to those used in the classic 3-D FFT-based

algorithm [51]-[53] are employed to obtain wave spectrum and parameters. To apply the wavelet method for wave extraction, the key is to select a proper calibration factor β. A simple look-up-table-based 2-D CWT wave analysis algorithm [93] is proposed to include the following steps:

1. sub-image acquisition and normalization;
2. determination of appropriate β from Table 3.1 and (3.27) based on the provided information of Δx, N_x, and measured wave period T_{01} using other instruments such as buoy;
3. 2-D CWT analysis on a single frame of radar image to obtain the image spectrum $I(k'_x, k'_y)$;
4. 2-D CWT analysis on multiple frames to obtain an averaged spectrum $I(k'_x, k'_y)$;
5. high-pass filtering (empirical threshold $\omega_{th} = 2\pi \times 0.03$ rad/s);
6. conversion from image spectra to wave spectra using the MTF;
7. derivations of wave spectra and parameters.

3.2.3 A Self-Adaptive 2-D CWT Wave Analysis Algorithm

Although accurate ocean wave spectra and parameters can be derived from the look-up-table-based method, the calibration factor β required for the 2-D CWT cannot be selected until Δx, N_x, and T_{01} are specified. Typically, the image resolution Δx and sub-image size N_x are available from the system specifications, while the value of T_{01} must be obtained from other instrumentation such as a wave buoy. However, here, an iterative algorithm, which enables the system to automatically select an optimal calibration factor β without a *in situ* buoy reference, is proposed. The selection process involves the following:

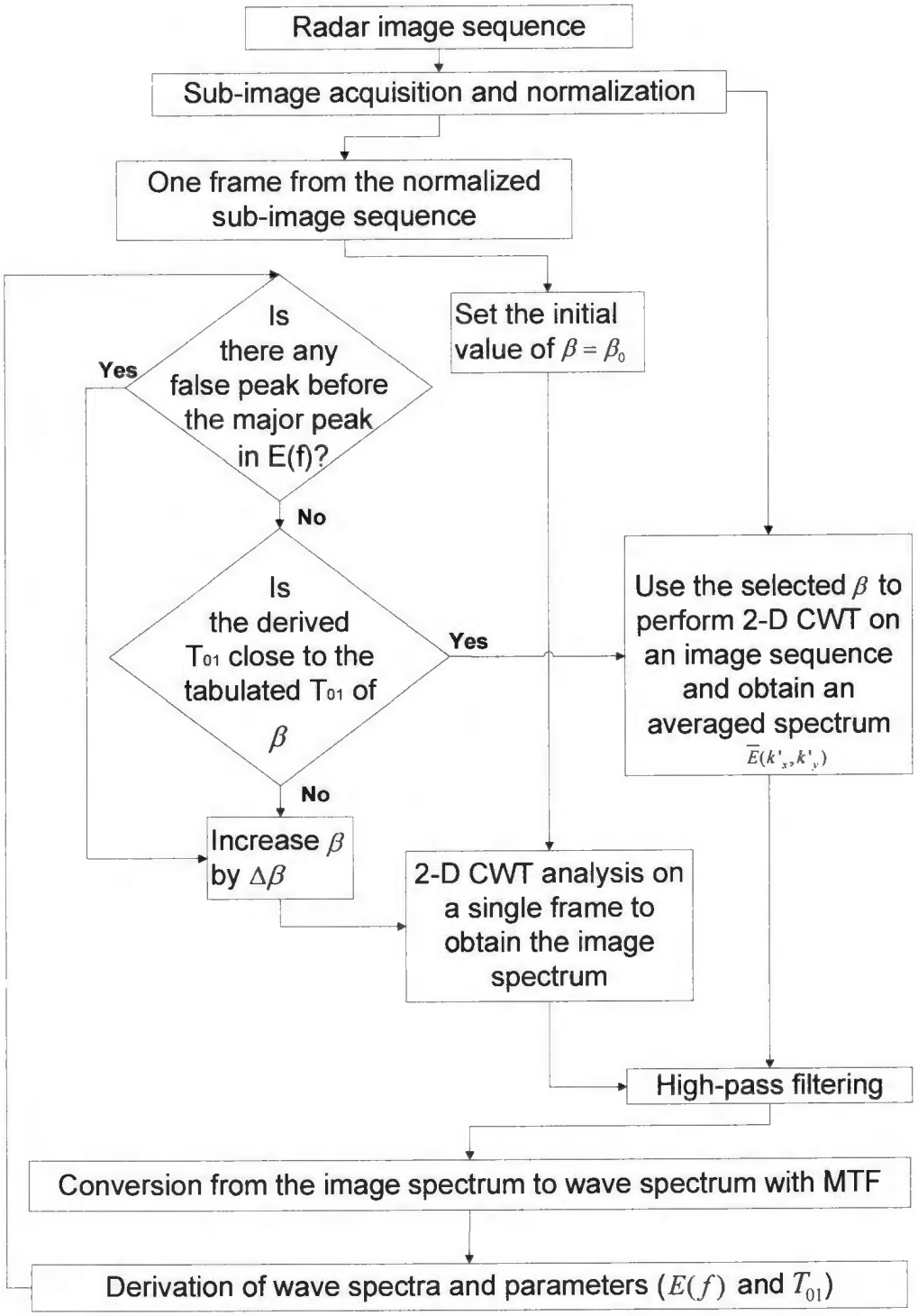

Figure 3.8: Flow chart of the self-adaptive 2-D CWT-based wave analysis algorithm.

Chapter 4

Results and Analysis

In Chapter 2 and Chapter 3, the FFT-based and CWT-based wave analysis algorithms are presented. In this chapter, the proposed algorithms are validated using both simulated radar data and dual-polarized radar field data. In the former case, radar images are simulated for various conditions using a revised Pierson–Moskowitz (P-M) spectrum [97] assuming shadowing and tilt modulations [32], [38]-[1]. For the field test, both horizontally polarized (H-pol) and vertically polarized (V-pol) radar data were collected on the east coast of Canada. *In situ* TRIAXYS directional wave buoy and acoustic Doppler current profiler (ADCP) records that were gathered in the same area are also available for data comparison.

4.1 Simulated Data Test

In this section, numerical simulations of the ocean surface and radar images are first discussed (also see [44]). Then, results derived using both the FFT and CWT algorithms applied to the generated radar images under different circumstances are presented and analyzed.

4.1.1 Nautical Radar Image Simulation

Simulation of ocean surface

Based on the inverse Fourier transform of the ocean wave power spectrum, the ocean surface elevation $\eta(x, y, t)$, where (x, y) and t are the position and time coordinates, respectively, can be described as a superposition of sinusoidal wave components of varying amplitudes, angular frequencies and random phases [38]-[1] and may be cast as

$$\eta(x, y, t) = \sum_{i=1}^{M} \sum_{j=1}^{N} A_{ij} \sin(\omega_i t - k_i x \cos\theta_j - k_i y \sin\theta_j + \delta_{ij}) \tag{4.1}$$

where A_{ij} is the amplitude for the wave component having angular frequency ω_i, direction θ_j, and wavenumber k_i. A random phase δ_{ij}, uniformly distributed on the interval $[0, 2\pi)$, is also introduced in order to generate a realistic ocean surface with irregular waves. The amplitude in equation (4.1) may be expressed as

$$A_{ij} = \sqrt{2S(\omega_i, \theta_j)d\omega d\theta} \tag{4.2}$$

where $S(\omega_i, \theta_j)$ is the ocean wave power spectrum that is used to simulate the ocean surface. Various forms, such as the Neumann Spectrum, the Wallops Spectrum, the P-M Spectrum, and the Mitsuyasu Spectrum [43], [69] are suitable candidates for the ocean power spectrum. The non-directional wave spectrum implemented in this thesis is from the 15th International Towing Tank Conference (ITTC) based on a Pierson Moskowitz (P-M) spectrum [38]-[1] and is given as

$$S(\omega) = \frac{0.11}{2\pi} H_s^2 T_{01} \left(\frac{T_{01}\omega}{2\pi}\right)^{-5} e^{-0.44\left(\frac{T_{01}\omega}{2\pi}\right)^{-4}} \tag{4.3}$$

where ω is the angular frequency, H_s is the significant wave height, and T_{01} is the mean period. The directional characteristics of the wave spectrum are accounted for

by using a distribution function given by

$$D(\theta) = \frac{2^{2d-1}}{\pi}\frac{\Gamma^2(d+1)}{\Gamma(2d+1)} \cdot \cos^{2d}(\frac{\theta - \theta_w}{2}) \tag{4.4}$$

where Γ is the Gamma function, θ_w is the wave propagation direction, and d is a so-called spreading parameter that is used to describe the degree of distribution. As discussed in [69], the selection of this spreading parameter is determined by the wind speed and peak frequency of the wave field. As is usually the case in many investigations, in this thesis, d is assigned a value of 2. Thus,

$$D(\theta) = \frac{4}{3\pi}\cos^4(\frac{\theta - \theta_w}{2}) \tag{4.5}$$

The overall directional wave spectrum is then written as [38]-[1]

$$S(\omega, \theta) = S(\omega)D(\theta) = S(\omega)\frac{4}{3\pi}\cos^4(\frac{\theta - \theta_w}{2}) \tag{4.6}$$

Shadowing modulation

For far ranges and horizontal polarization, the electromagnetic waves from X-band marine radar reach the ocean surface at large incidence angles, nearly grazing the surface. Therefore, the surface is partially shadowed by higher ocean waves. This effect, known as shadowing modulation, is depicted in Fig. 4.1. From that figure, a geometrical optics approximation can be made as follows: the incidence angle at the ocean surface elevation η is

$$\theta_0(\eta) = \tan^{-1}[R(\eta)/(\Lambda - \eta)] \tag{4.7}$$

where $R(\eta)$ is the horizontal range from the radar to the observation point, and Λ is the antenna height over the sea level. As depicted in the figure, with respect to the antenna, a point with elevation η will be in the shadow of a higher wave with elevation η' at the same azimuthal angle when the incidence angles are related as

$$\theta_0'(\eta') \geq \theta_0(\eta) \tag{4.8}$$

where

$$\theta_0'(\eta') = \tan^{-1}[R(\eta')/[\Lambda - \eta'] \tag{4.9}$$

The shadowing factor can be described by [32]

$$\sigma_{sh}(\eta) = \begin{cases} 0, & \text{if } R(\eta') < R(\eta), \text{ and } \theta_0'(\eta') \geq \theta_0(\eta) \\ 1, & \text{otherwise.} \end{cases} \tag{4.10}$$

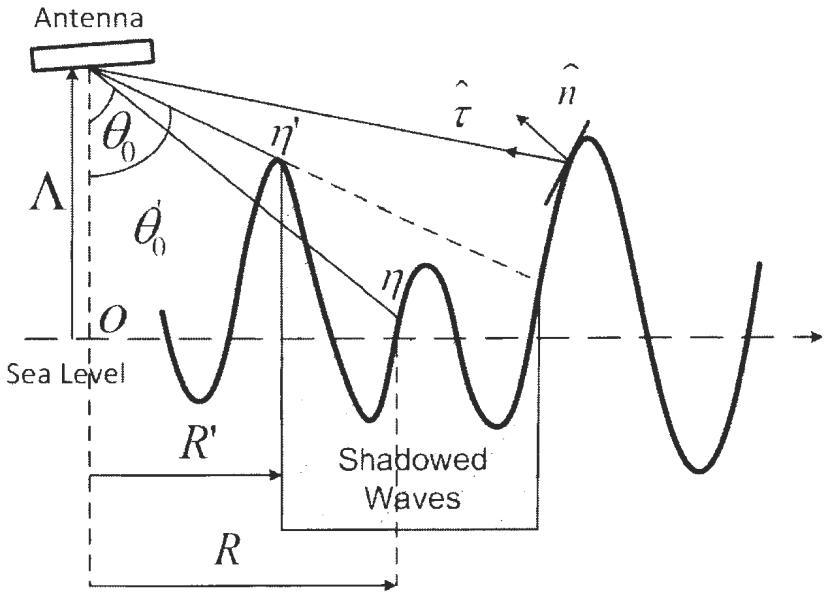

Figure 4.1: Shadowing and tilt modulation [32].

Tilt modulation

Tilt modulation results from changes in the effective incidence angle along the long wave slope, and it can be simulated by using the scalar product of the exterior normal vector to the ocean surface $\hat{n}(\eta)$ and the vector $\hat{\tau}(\eta)$ from the illuminated ocean surface η to the antenna as shown in Fig. 4.1. Analytically,

$$\hat{n}(\eta) = (\vec{\rho}_x \times \vec{\rho}_y)/\left\|\vec{\rho}_x \times \vec{\rho}_y\right\| \tag{4.11}$$

where

$$\vec{\rho}_x = (1, 0, \partial\eta/\partial x) \tag{4.12}$$

$$\vec{\rho}_y = (0, 1, \partial\eta/\partial y) \tag{4.13}$$

are the 3-D tangent vector components on the surface [32]. The tilt factor $\sigma_{tilt}(\eta)$ can be determined from

$$\sigma_{tilt}(\eta) = \begin{cases} \iota(\eta), & \text{if } \iota(\eta) > 0 \\ 0, & \text{otherwise} \end{cases} \tag{4.14}$$

with

$$\iota(\eta) = \hat{n}(\eta) \cdot \hat{\tau}(\eta) \tag{4.15}$$

The values of $\sigma_{sh}(\eta)$, $\sigma_{tilt}(\eta)$ are then applied to the generated sea surface and coded with 256 gray levels [32].

4.1.2 Simulated Data Results and Analysis

To verify the proposed 3-D FFT-based and 2-D CWT-based wave analysis algorithms, simulated nautical radar images generated under various wave conditions are used. The simulation parameters for the radar images are listed in Table 4.1. An example of the simulated images is shown in Fig. 4.2. Fig. 4.2 (a) shows the generated sea

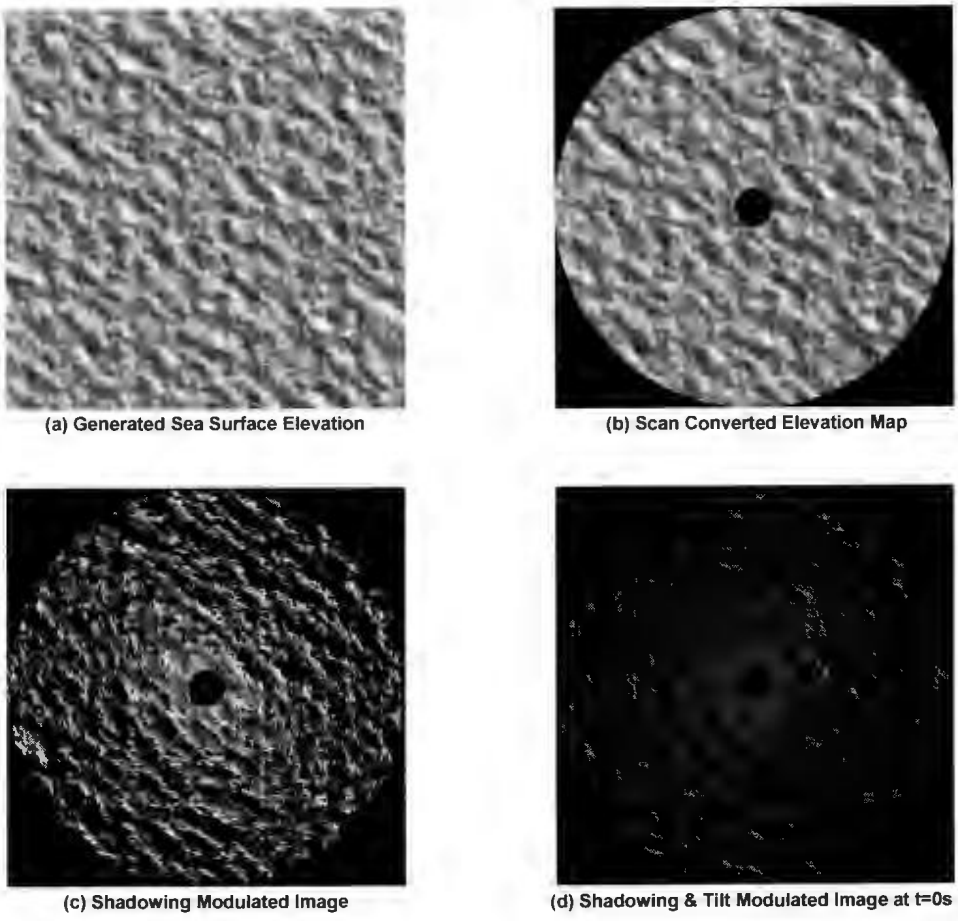

Figure 4.2: Resultant images incorporating the P-M spectrum and using shadowing and tilt modulation: (a) Generated ocean surface elevation; (b) Elevation map after scan conversion; (c) Shadowing modulated image; (d) Tilt and shadowing modulated image

surface elevation using the ITTC-recommended P-M spectrum. The main propagation direction is 45° from true North. Fig. 4.2 (b) depicts the generated sea surface using the scan conversion technique, which transforms the radar data from a range-azimuth (polar) format to an x-y (Cartesian) format for display. The resolutions in range and angle are assigned as 10.5 m and 1°, respectively. Fig. 4.2 (c) shows the image with shadowing modulation and Fig. 4.2 (d) is the simulated radar image incorporating both shadowing and tilt modulation.

Table 4.1: Simulation Parameters

Electromagnetic wave frequency	10 GHz
Antenna angular speed	48 r.p.m.
Polarization	Horizontal
Antenna height	20 m
Range resolution (Δr)	10.5 m
Image Size	512×512 pixels
Directional distribution	Cosine squared

Once images are simulated for a variety of surface conditions, the next step involves the application of current estimation algorithms, including least squares (LS), iterative LS, and normalized scalar product (NSP) methods. Subsequently, with the effects of the currents removed, the enhanced 3-D FFT-based and 2-D CWT-based algorithms may be applied to obtain wave parameters.

4.1.2.1 Results of surface current estimation

In this section, results of the estimated near-surface current velocity (velocity of encounter) and direction derived under a variety of conditions are presented. First, the current algorithms are applied to simulate radar data for cases which differ on in mean period, T_{01}. Then, tests are conducted on simulated data generated with wave fields having various angles between the wave and current directions.

In Fig. 4.3, the distance between the center of the original radar image and the

center of the sub-image (segment "OC") is defined as the sub-image distance, and is symbolized as D_{sub}. The angle between the wave direction and the segment "OC" is defined as the sub-image direction and is written as θ_{sub}.

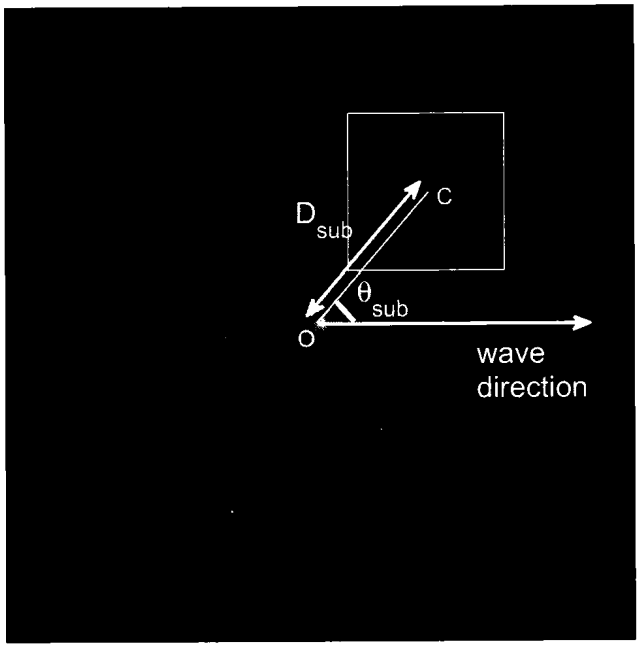

Figure 4.3: Sub-image acquisition for wave field analysis.

Figs. 4.4 - 4.6 present the results of the derived velocity of encounter and direction from the simulated radar images with T_{01} = 8 s, 10 s, and 12 s, respectively. The significant wave height of the wave field is specified as H_s = 3.5 m. The wave direction is $\theta_w = 270°$ with respect to (w.r.t) true North. The input velocity of encounter, u_{in}, ranges from 0 to 15 m/s, in steps of 0.5 m/s. The direction of the surface current from true North is $\theta_u = 90°$. The sub-image sequence used for current and wave analysis is acquired at the wave propagation direction ($\theta_{sub} = \theta_w$), 500 m away from the radar antenna (D_{sub} = 500 m). In Figs. 4.4 - 4.6, the (black) solid line represents the input velocity of encounter parameters; the (green) dotted line with circles represents the derived velocity of encounter information using the LS method; the (red) dashed line

with diamonds indicates the derived velocity of encounter information using the iterative LS method; and the (blue) dash-dot line with asterisks shows the derived velocity of encounter information using the NSP method. It is observed from the figures that Young's LS method [16] provides rough approximations of the velocity of encounter. As may be observed in Fig. 4.4, errors in the retrieved current may reach as high as 2 m/s. Senet's iterative LS method [47] provides more accurate results and the maximum error of the velocity of encounter and direction are around 0.15 m/s and 7°. Similarly, Serafino's NSP method [49] also provides highly accurate results, with maximum error of retrieved velocity of encounter of about 0.10 m/s and maximum error of the retrieved current direction of 6°. As discussed in Section 2.1.3, the accuracy of the original NSP method relies on a large range and a fine resolution of the velocity for the two-dimensional search, and thus it requires significant computation, which takes more than 1000 seconds, while the iterative LS method only needs tens of seconds to process the same dataset. In order to increase the speed of the algorithm, the improved NSP current estimation algorithm that uses variable search ranges and resolutions as referred to in Section. 2.1.3 is applied in this thesis [87]. After the modification, the processing time is reduced to less than 300 seconds.

The error analyses of the current estimation algorithms are given in Table 4.2. ΔV_m and ΔV_{sd} are the mean difference and standard deviation between the retrieved velocity of encounter and the input value. ΔD_m and ΔD_{sd} are the mean difference and standard deviation of the current direction. From the table, it is observed that the mean difference of the results derived from the LS method are larger than those from the iterative LS and NSP methods. It is also easy to conclude from the standard deviations that the iterative LS and NSP methods provide more accurate and robust current estimation results compared with those from the LS method. In this thesis, a fine search resolution of $\Delta u_i = 0.02$ m/s is used in the NSP current estimation. If a

finer resolution is used, better results with smaller mean difference and standard deviation are expected to be obtained, but this will require a longer processing time. In addition, it is observed from the table that errors in the results do not change significantly with mean period T_{01}. Thus, the accuracy of the current retrieval algorithms does not appear to be affected by the mean period of the wave field.

Table 4.2: Error Analyses of the Derived Velocity of Encounter Using Different Algorithms at T_{01} = 8, 10, 12 s.

T_{01} (s)	Algorithms	ΔV_m (m/s)	ΔV_{sd} (m/s)	ΔD_m (°)	ΔD_{sd} (°)
8	LS	-0.0534	0.8330	-2.4165	11.6681
	Iterative LS	-0.0030	0.0741	0.1435	1.8320
	NSP	0.0039	0.0680	0.3632	1.5832
10	LS	-0.0890	0.4283	-0.3423	9.0164
	Iterative LS	0.0130	0.0613	0.5362	2.7169
	NSP	-0.0002	0.0630	0.5266	2.6708
12	LS	-0.2473	0.4717	1.0458	7.3867
	Iterative LS	0.0047	0.0828	0.3167	1.2848
	NSP	0.0001	0.0630	0.4505	1.6009

Simulated data with different angles between the wave and current directions are tested next. In this test, the mean period of the simulated data is fixed as T_{01} = 12 s. The sub-image sequence used in the wave analysis is also acquired at the wave propagation direction ($\theta_{sub} = \theta_w$), 500 m away from the radar antenna (D_{sub} = 500 m). The significant wave height of the wave field remains at 3.5 m. The direction of the surface current is90° from true North. The wave directions in the data test are set to be θ_w = 270°, 240°, 180°, and 120° from true North. Thus, the angles between the wave and current directions are θ_{wu} = 180°, 150°, 90°, and 30°, respectively. Results for the velocity of encounter and direction are provided in Figs. 4.7 - 4.9. The range of the input velocity of encounter is 0 to 15 m/s in steps of 0.5 m/s. The LS method is found to provide rough approximations of the velocity of encounter. More accurate results are derived by the iterative LS and NSP methods.

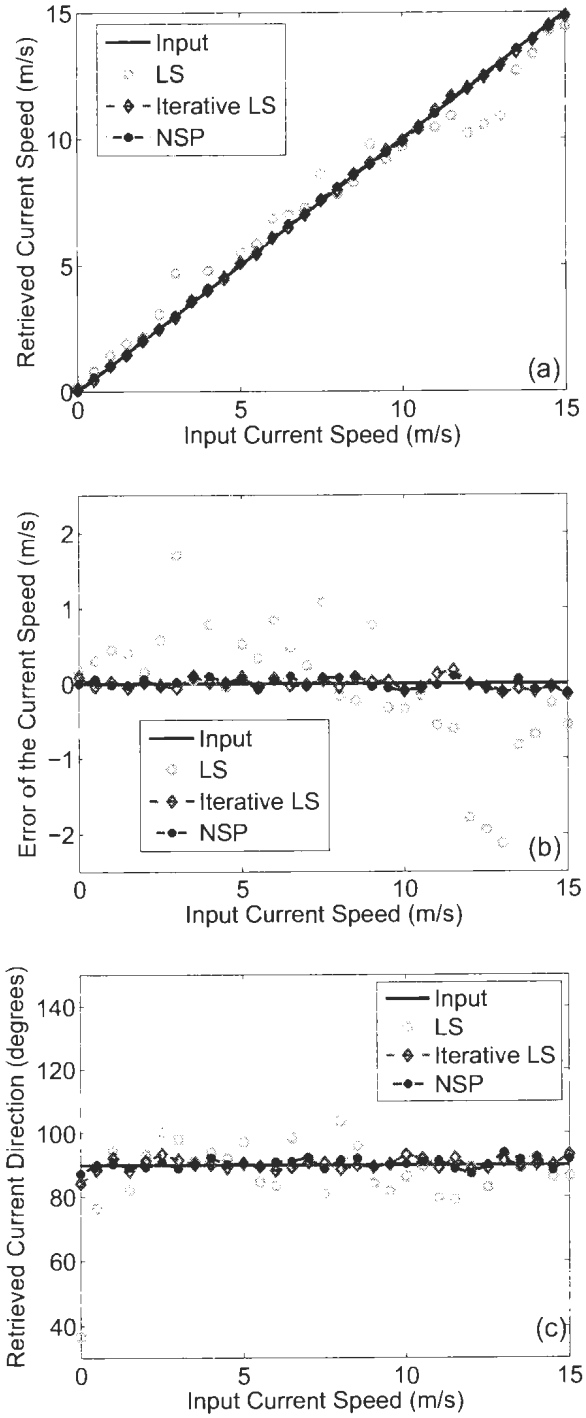

Figure 4.4: Results of derived velocity of encounter from the simulated radar images with $T_{01} = 8$ s: (a) Derived velocity of encounter; (b) Errors of the derived velocity of encounter; (c) Derived current direction.

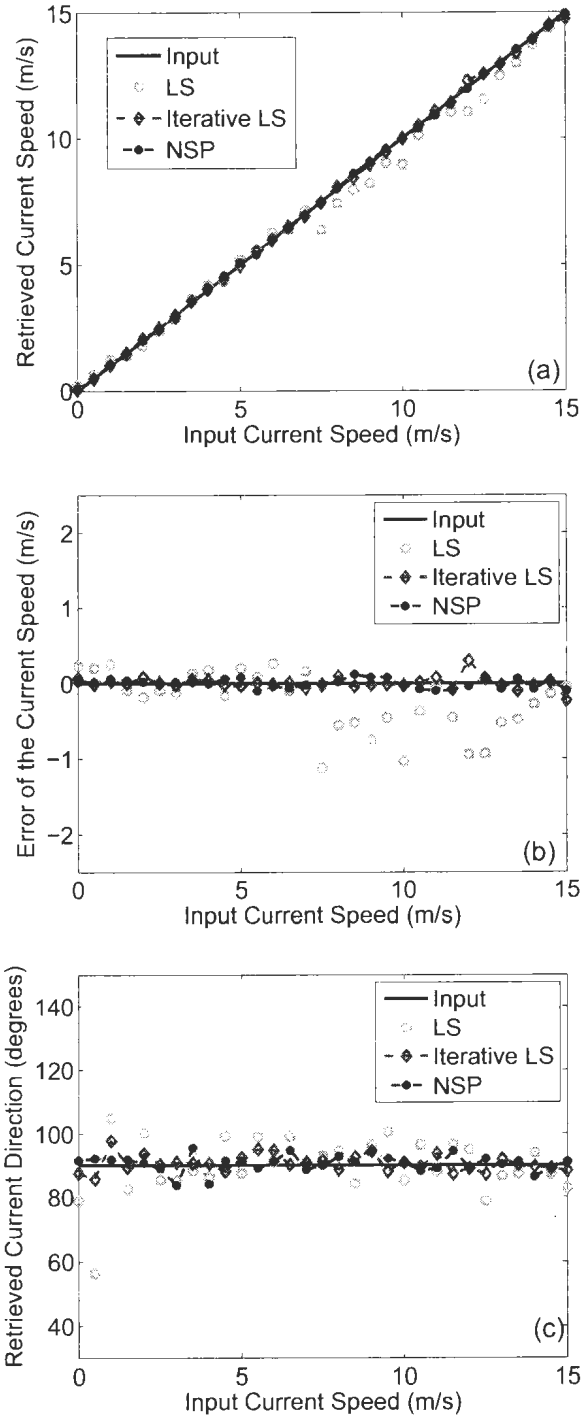

Figure 4.5: Results of derived velocity of encounter from the simulated radar images with $T_{01} = 10$ s.

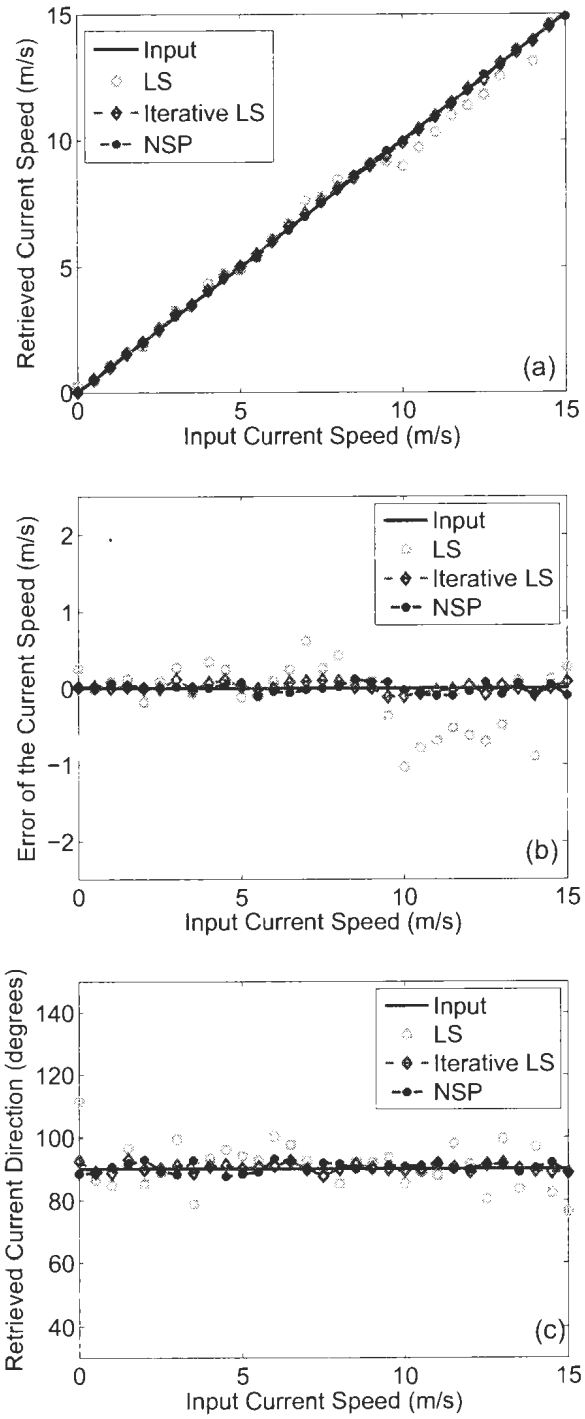

Figure 4.6: Results of derived velocity of encounter from the simulated radar images with $T_{01} = 12$ s.

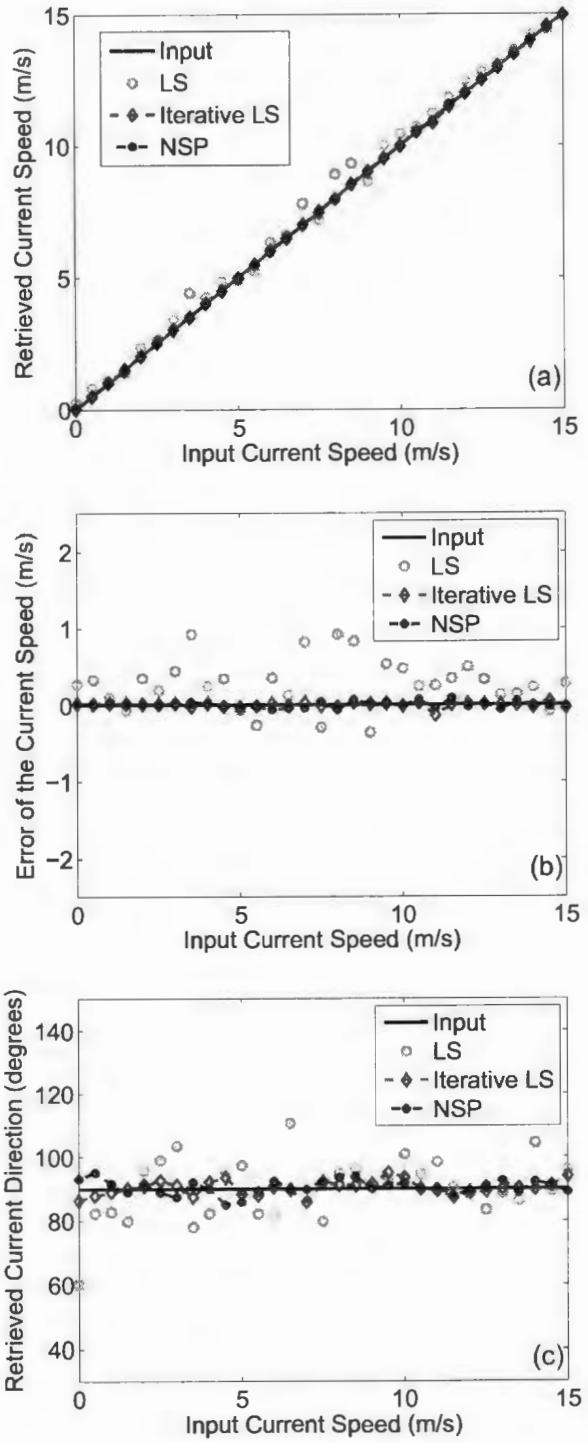

Figure 4.7: Results of derived velocity of encounter from the simulated radar images with $\theta_{wu} = 180°$.

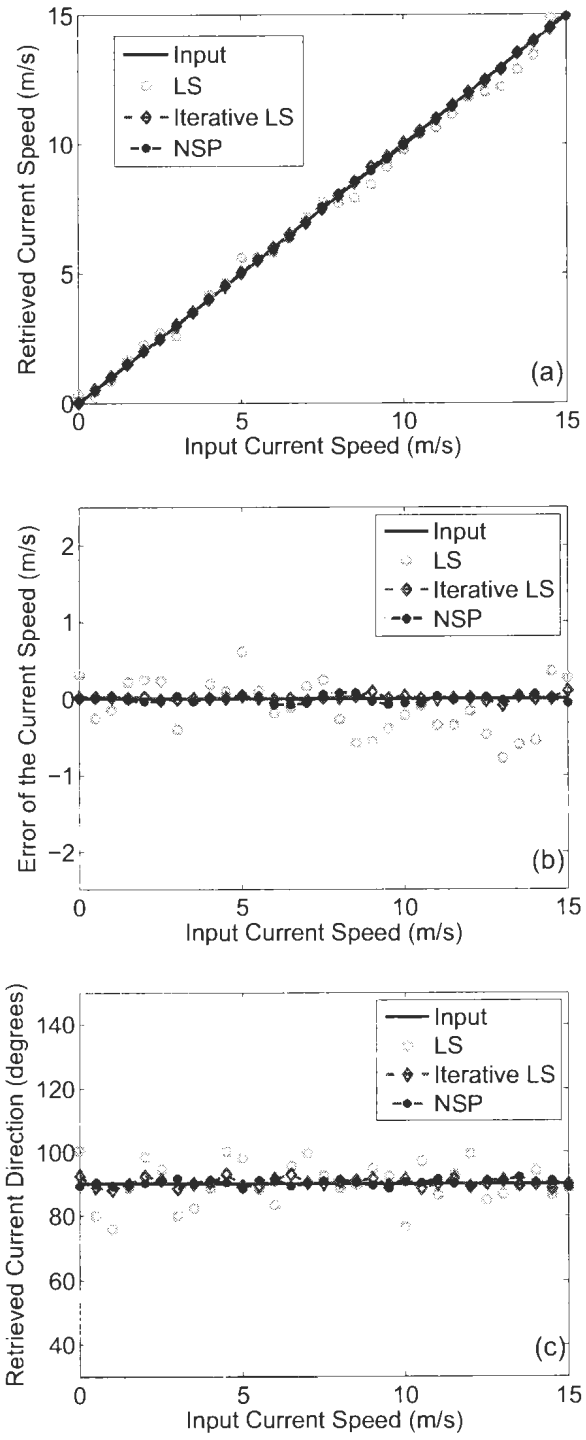

Figure 4.8: Results of derived velocity of encounter from the simulated radar images with $\theta_{wu} = 150^{\circ}$.

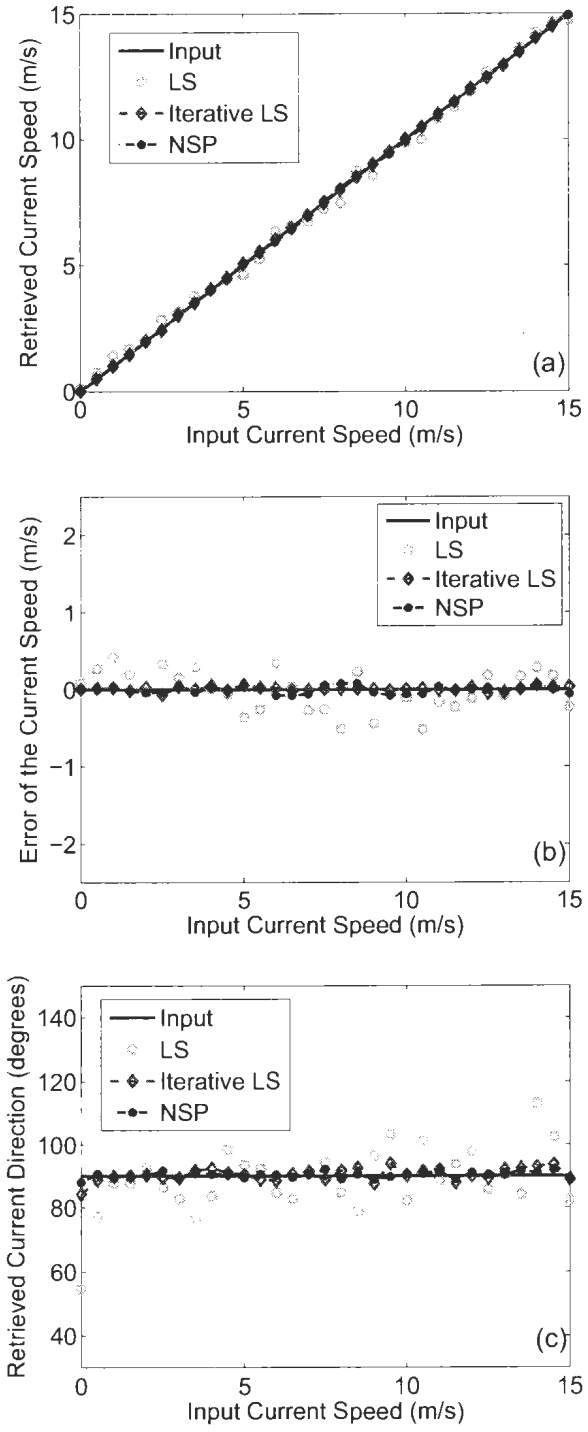

Figure 4.9: Results of derived velocity of encounter from the simulated radar images with $\theta_{wu} = 90^{\circ}$.

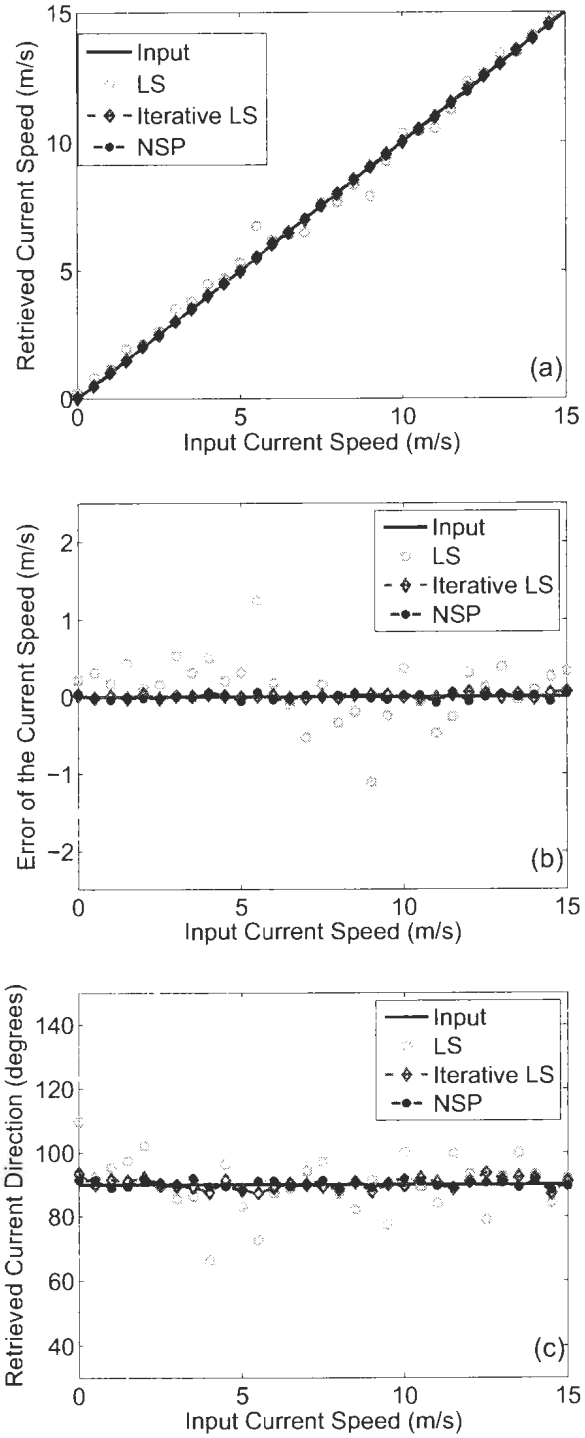

Figure 4.10: Results of derived velocity of encounter from the simulated radar images with $\theta_{wu} = 30^{\circ}$.

Table 4.3: Error Analyses of the Derived Velocity of Encounter Using Different Algorithms for $\theta_{wu} = 180°$, 150°, 90°, and 30°.

θ_{wu} (°)	Algorithms	ΔV_m (m/s)	ΔV_{sd} (m/s)	ΔD_m (°)	ΔD_{sd} (°)
180	LS	-0.0130	0.2623	0.0074	9.7464
	Iterative LS	0.0097	0.0303	0.2130	2.1380
	NSP	-0.0052	0.0479	0.4493	2.2001
150	LS	-0.1082	0.3578	0.1226	6.8352
	Iterative LS	0.0101	0.0337	0.3141	1.3509
	NSP	-0.0052	0.0479	0.3104	0.9857
90	LS	0.1099	0.4161	-1.2248	10.3881
	Iterative LS	0.0112	0.0274	0.4216	2.0265
	NSP	-0.0013	0.0630	0.2965	0.9984
30	LS	0.2728	0.4189	0.0374	8.8776
	Iterative LS	-0.0001	0.0318	0.2660	1.6836
	NSP	0.0045	0.0375	0.2339	1.0701

The error analyses for the current estimation algorithms with differing θ_{wu} are listed in Table 4.3. From the table it can be also observed that the iterative LS and NSP methods provide more accurate and robust current estimation results with smaller standard deviations than those retrieved from the LS method.

4.1.2.2 Wave information results

Once the current information is obtained, a band-pass filter is constructed using (2.35) - (2.37) to retrieve ocean wave information from the radar images. As discussed in Chapter 2, an enhanced 3-D FFT-based wave extraction algorithm, based on the results of mode classification in the iterative LS process, is applied in this thesis. Then, a 2-D CWT-based algorithm, as described in Chapter 3, is used for wave analysis. Results from both algorithms are provided and compared.

Fig. 4.11 illustrates the comparison of the wavenumber spectra derived at each stage in 3-D FFT-based wave analysis. Fig. 4.11 (a) is the image spectrum $I(k_x, k_y)$ after the Fourier analysis and high-pass filtering process. An energy distribution

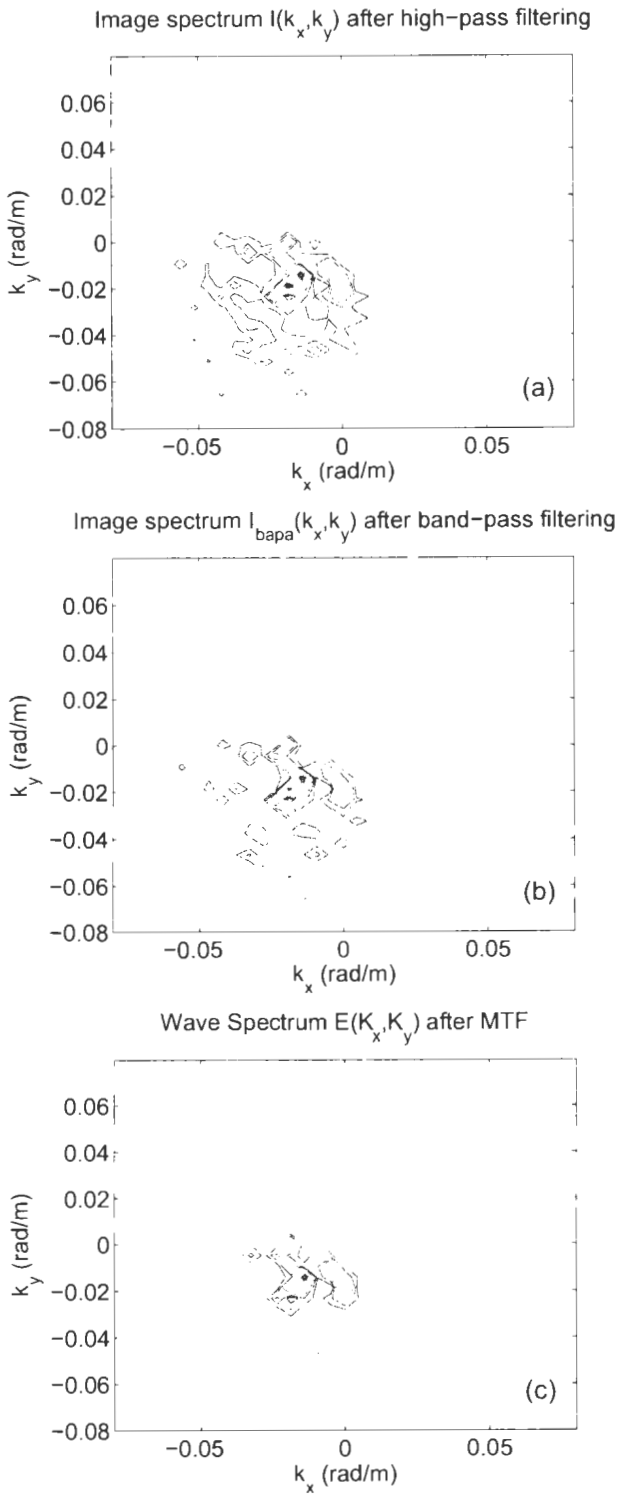

Figure 4.11: Comparison of wavenumber spectra derived at each stage in the 3-D FFT wave analysis: (a) Image spectrum $I(k_x, k_y)$ after the Fourier analysis and high-pass filtering process; (b) Image spectrum $I_{bapa}(k_x, k_y)$ after band-pass filtering; (c) Wave spectrum $E(k_x, k_y)$ after the MTF process.

which roughly describes the wave field is represented by this spectrum, and the non-stationary and non-homogeneous components near zero frequency are eliminated by the high-pass filter. Fig. 4.11 (b) is the image spectrum $I_{bapa}(k_x, k_y)$ after both the high-pass and band-pass filtering process. The simulated wave field contains a velocity of encounter $u = 3$ m/s and this introduces Doppler frequency components into the energy spectrum. As discussed in Chapter 2, a band-pass filter is designed to remove the non-wave components. Compared with Fig. 4.11 (a), it is observed that some energy components which are far away from the dispersion shell are removed in Fig. 4.11 (b). Fig. 4.11 (c) presents the wave spectrum after the modulation transfer function (MTF) process. On comparing with Fig. 4.11 (a), (b), it is obvious that most components due to the non-linearity of the radar imaging mechanism are removed from the spectrum in the Fig. 4.11 (c).

Once $E(k_x, k_y)$ is obtained, various other wave spectra and parameters can be derived as discussed in Section 2.2.1. In this thesis, the following wave information is derived:

- directional frequency spectra $E(f, \theta)$
- frequency spectra $E(f)$
- mean wave direction $\theta(f)$
- wave direction θ_w
- mean period T_{01}
- peak frequency f_p

In order to investigate the performance of the proposed wave analysis algorithms under different circumstances, simulated radar data with different velocities of encounter u, different mean periods T_{01}, and different selections of sub-image positions

are tested. For the FFT-based method, 32 frames of consecutive radar images are used. The velocity of encounter is estimated with the iterative LS method. The parameter used in the modulation transfer function (MTF) process for the Fourier analysis is modified using the curve fitting techniques in [32] and may be written as

$$\mu = \begin{cases} -0.98, & \text{if } |k_{xy}| \leq e^{-2.75} \\ -1.2, & \text{otherwise} \end{cases} \tag{4.16}$$

Compared with the original MTF with $\mu = -1.2$ [32], [51]-[59], this modified MTF expression retrieves a better energy distribution for the high frequency components of the wave field at different sea conditions (see Fig. 4.12).

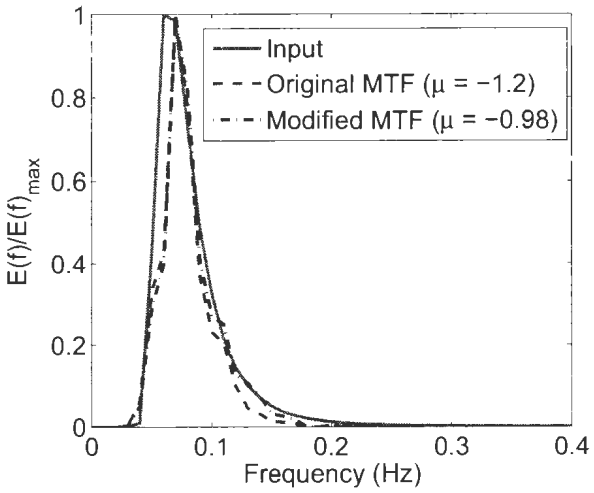

Figure 4.12: Comparison of the derived $E(f)$ with original and modified MTF in the 3-D FFT-based simulated data test.

Having considered the FFT approach, attention is next focused on the wavelet algorithm. Based on the discussion in Chapter 3, the parameters assigned for the wavelet analysis are determined and listed in Table 4.4. The calibration parameter β that regulates the value of scaling factor a_{max} is automatically selected, as proposed

in Fig. 3.8. Once β is determined, a 2-D CWT is performed on the input radar image sequence and an averaged spectrum $E(k_x, k_y)$ is obtained. In this process, a 180° ambiguity is observed and it is manually eliminated for wave information extraction using information gathered from other instrumentation. The parameter used in the MTF process for wavelet analysis is also modified as

$$\mu = \begin{cases} -1.4, & \text{if } |k_{xy}| \leq e^{-2.75} \\ -1.2, & \text{otherwise} \end{cases} \tag{4.17}$$

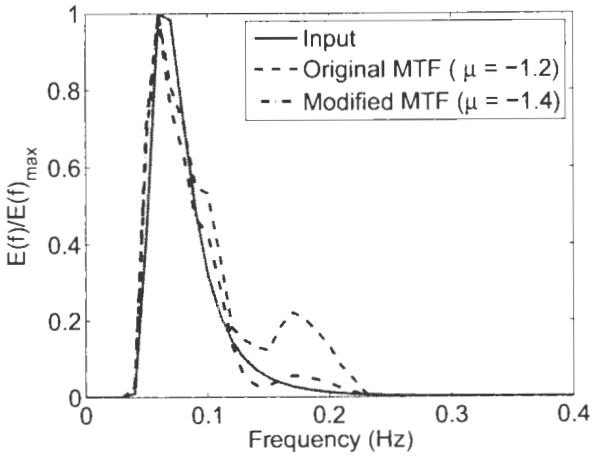

Figure 4.13: Comparison of the derived $E(f)$ with original and modified MTF in the 2-D CWT-based simulated data test.

Table 4.4: Wavelet Parameters Configuration

k_0	(6.0)
λ	0.9
η	0.01
L_0	(1, 1)
N_x	128
β_0	1.4
$\Delta\beta$	0.2

As shown in Fig. 4.13, the modified MTF suppresses the overestimated energy within the high frequency band and leads to an improved spectrum (the dash-dot curve) compared to that derived with the original MTF process (the dash curve).

Fig. 4.14 presents the comparison of the results derived from the classic 3-D FFT algorithm as described in [32] and the modified 3-D FFT algorithm proposed in this paper. From Fig. 4.14 (a), it is observed that the energy of the higher harmonic components are eliminated in the modified 3-D FFT derived frequency spectrum. Also, the mean wave direction spectrum, $\theta(f)$, are recovered more accurately using the proposed modified 3-D FFT method, as shown in Fig. 4.14 (b). Fig. 4.14(c)(d)(e) illustrate the modified 3-D FFT derived, classic 3-D FFT derived, and input directional-frequency spectra $E(f, \theta)$. By comparison it is found that energy distributions derived from modified 3-D FFT algorithm are closer to the input spectrum.

The proposed 3-D FFT-based and 2-D CWT-based wave extraction algorithms are first tested with simulated radar images with velocities of encounter of $u = 0$ m/s, 1.5 m/s, 3.0 m/s, and 5.0 m/s. The sub-image sequence used in the wave analysis is still acquired at the wave propagation direction ($\theta_{sub} = \theta_w$), 500 m away from the radar antenna ($D_{sub} = 500$ m). The significant wave height of the wave field is $H_s = 3.5$ m. The wave and current directions, θ_w and θ_u, are both 210° from true North. The mean period of the wave field is 12 s.

Figs. 4.15 - 4.18 (a) show the input and derived 1-D frequency spectra, and the peaks of $E(f)_{FFT}$ and $E(f)_{CWT}$ agree well with those of $E_m(f)$. Figs. 4.15 - 4.18 (b) indicate that the mean wave direction spectra, $\theta(f)$, are recovered correctly using both methods. Figs. 4.15 - 4.18 (c)(d)(e) illustrate the FFT derived, CWT derived, and input directional-frequency spectra $E(f, \theta)$. It is observed from these spectra that the energy distributions derived from the Fourier and wavelet analysis are similar to the input spectra.

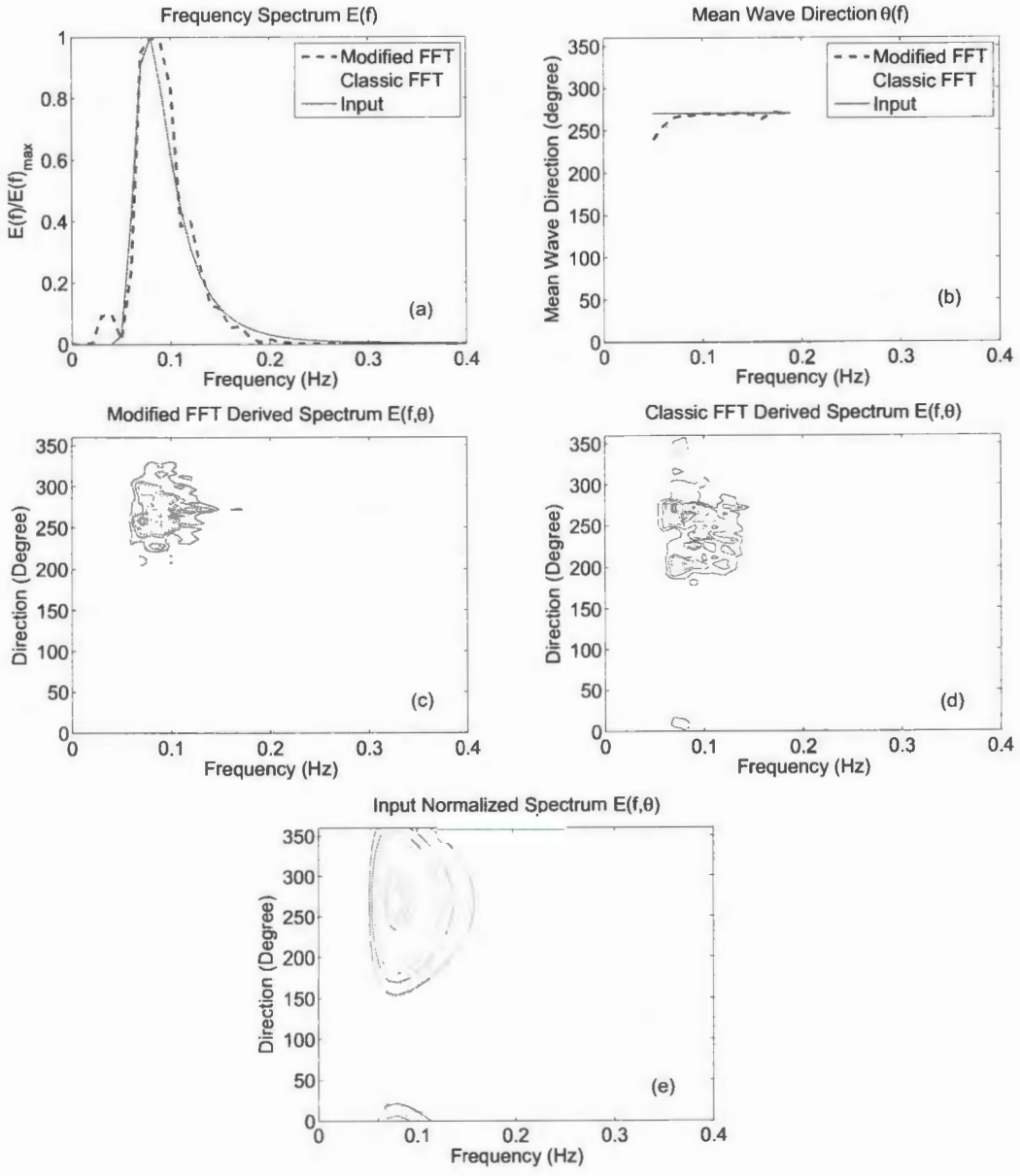

Figure 4.14: Comparison of derived spectra using the proposed modified 3-D FFT and the classic 3-D FFT wave analysis: (a) Normalized frequency spectrum $E(f)$; (b) Mean wave direction spectrum $\theta(f)$; (c) Modified 3-D FFT derived directional frequency spectrum $E(f,\theta)$; (d) Classic 3-D FFT derived directional frequency spectrum $E(f,\theta)$; (e) Input directional frequency spectrum $E(f,\theta)$.

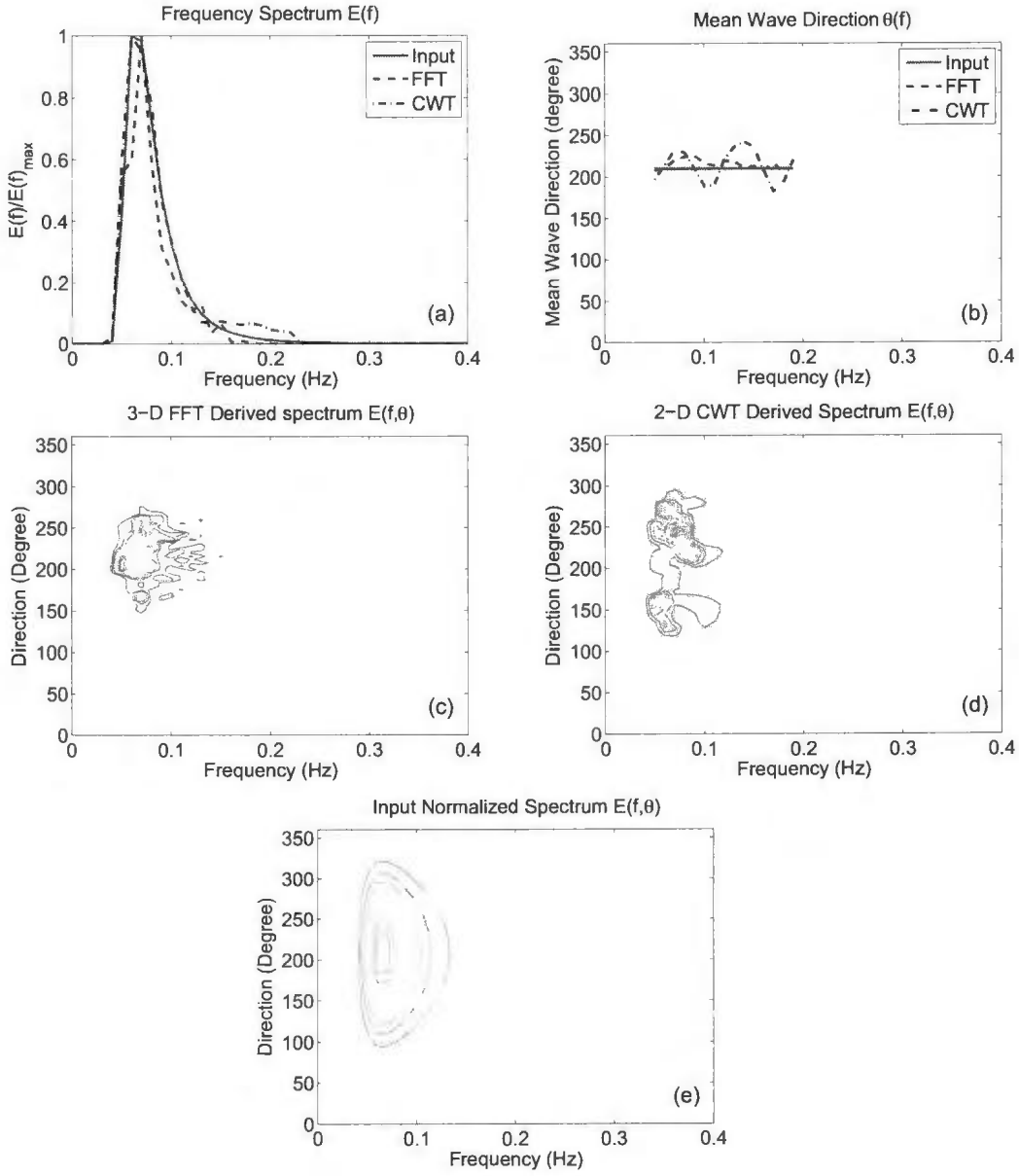

Figure 4.15: Comparison of derived spectra using 3-D FFT and 2-D CWT wave analysis under velocity of encounter $u = 0$ m/s: (a) Normalized frequency spectrum $E(f)$; (b) Mean wave direction spectrum $\theta(f)$; (c) 3-D FFT derived directional frequency spectrum $E(f, \theta)$; (d) 2-D CWT derived directional frequency spectrum $E(f, \theta)$; (e) Input directional frequency spectrum $E(f, \theta)$.

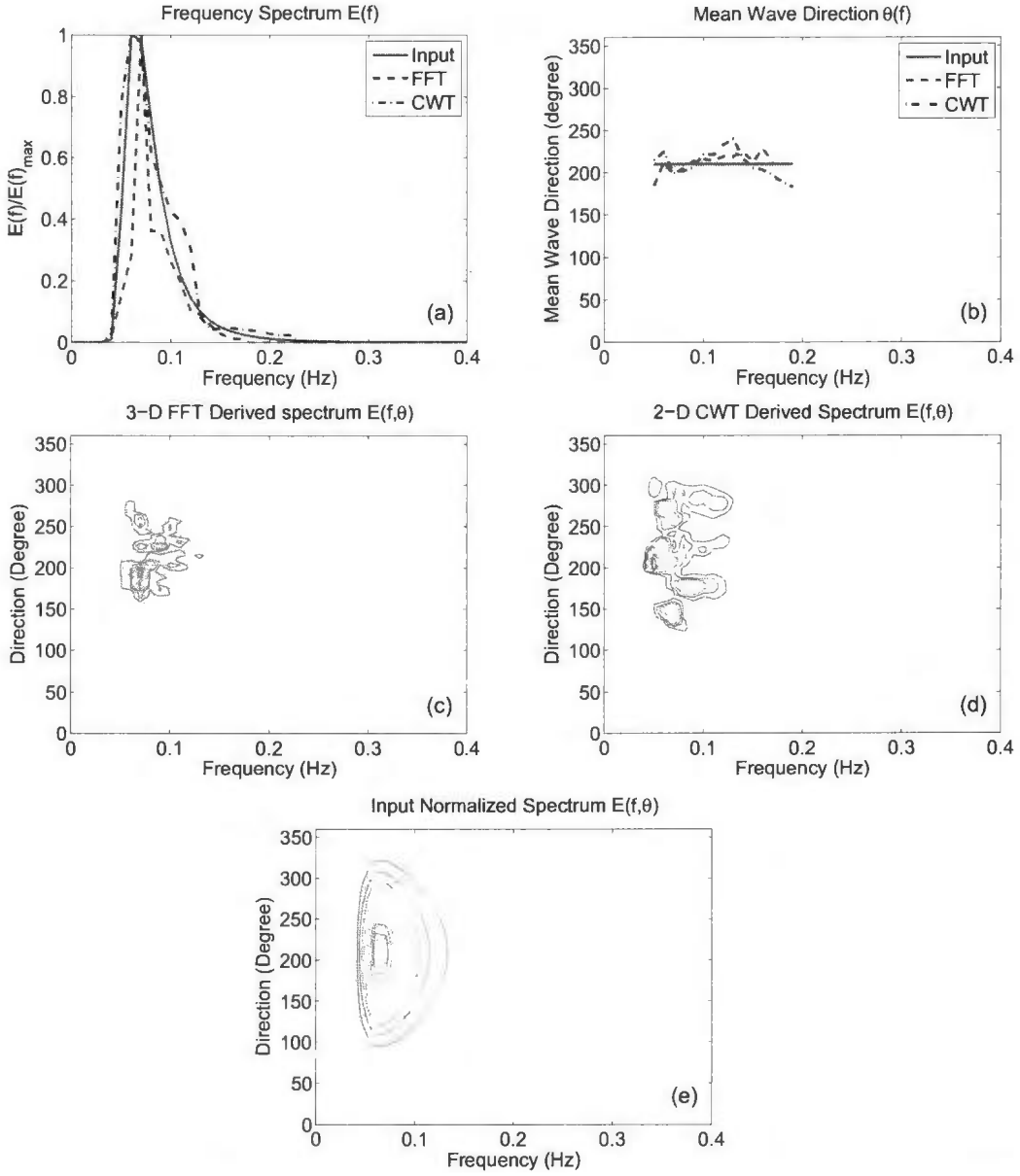

Figure 4.16: Comparison of derived spectra using 3-D FFT and 2-D CWT wave analysis under velocity of encounter $u = 1.5$ m/s.

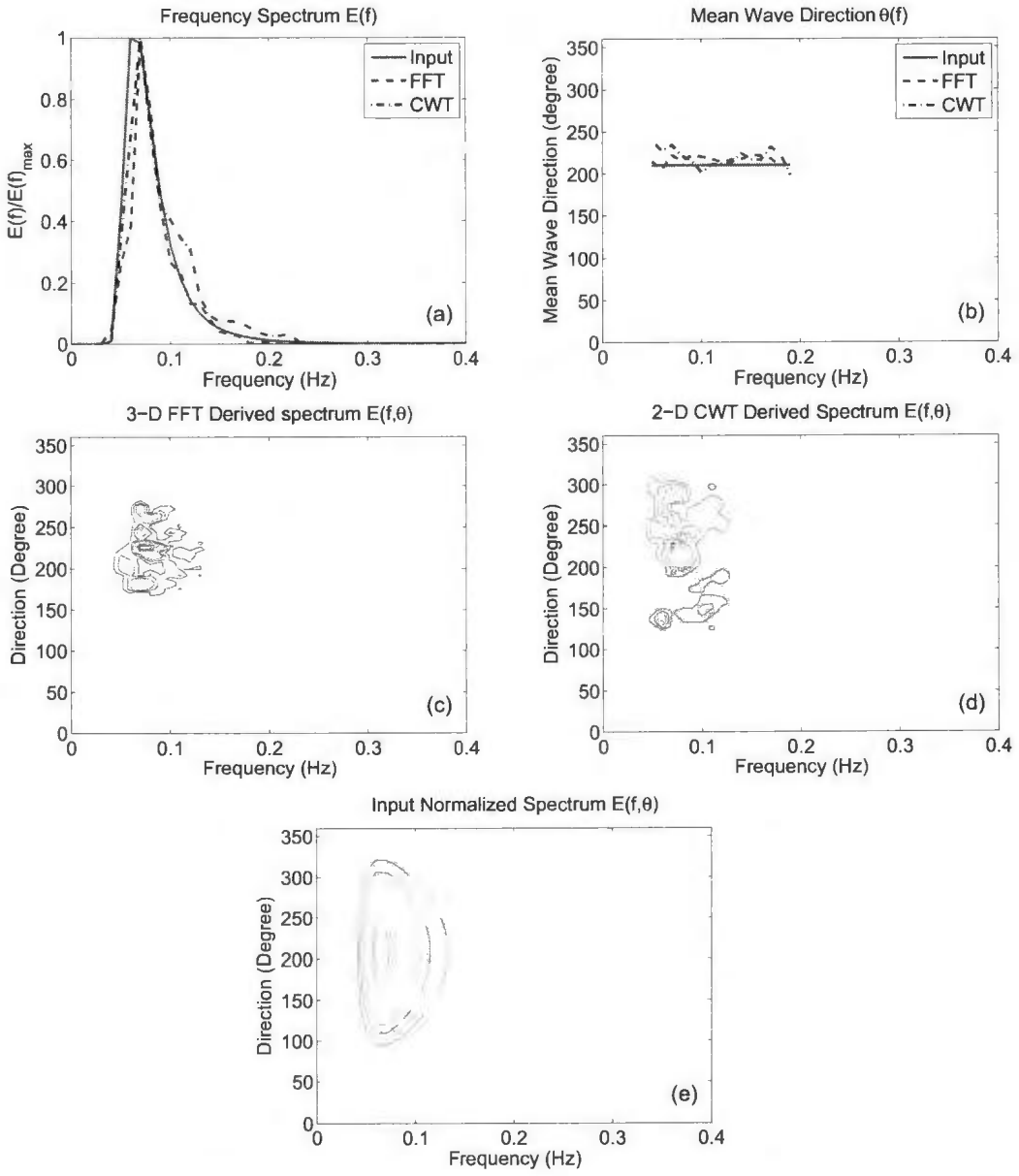

Figure 4.17: Comparison of derived spectra using 3-D FFT and 2-D CWT wave analysis under velocity of encounter $u = 3.0$ m/s.

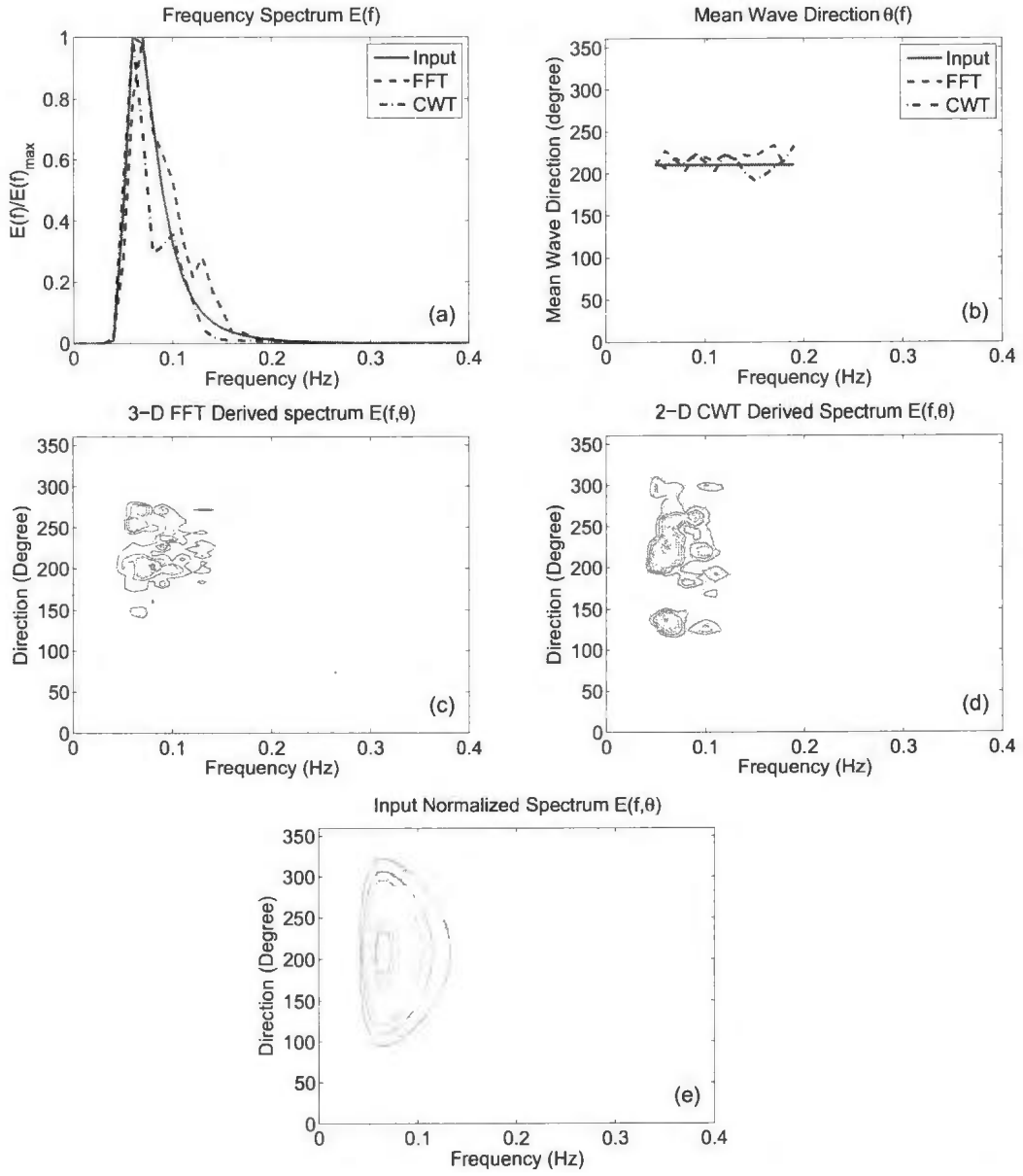

Figure 4.18: Comparison of derived spectra using 3-D FFT and 2-D CWT wave analysis under velocity of encounter $u = 5.0$ m/s.

Table 4.5: Retrieved Wave Parameters Using FFT- and CWT-based Algorithms at velocities of encounter $u = 0$ m/s, 1.5 m/s, 3.0 m/s, and 5.0 m/s.

Parameters	Input Data							
u_{in} (m/s)	0		1.5		3.0		5.0	
$\theta_{u_{in}}$ (°)	-		210		210		210	
$\theta_{w_{in}}$ (°)	210		210		210		210	
$T_{01_{in}}$ (s)	12.03		12.03		12.03		12.03	
$f_{p_{in}}$ (Hz)	0.0650		0.0650		0.0650		0.0650	
	Output Data							
Algorithms	FFT	CWT	FFT	CWT	FFT	CWT	FFT	CWT
u_{out} (m/s)	0.0116	n/a	1.4781	n/a	3.0048	n/a	4.9870	n/a
$\theta_{u_{out}}$ (°)	339.63	n/a	209.84	n/a	208.87	n/a	209.74	n/a
$\theta_{w_{out}}$ (°)	215.43	219.73	205.70	213.65	216.62	226.38	213.89	212.15
$T_{01_{out}}$ (s)	12.61	11.67	12.00	11.97	11.91	10.98	11.42	12.89
$f_{p_{out}}$ (Hz)	0.0700	0.0649	0.0700	0.0649	0.0700	0.0700	0.0655	0.0600

Table 4.5 compares the derived velocity of encounter with the input values for the 3-D FFT-based and 2-D CWT-based wave results under different velocities of encounter. Accurate ocean wave parameters can be obtained from both methods as listed in the table. Since the wavelet analysis does not include the process of band-pass filtering to compensate for the Doppler-shifted frequency due to the velocity of encounter, it is usually considered that the 2-D CWT-based wave analysis algorithm cannot retrieve accurate results in the case of a considerably large velocity of encounter. However, from Figs. 4.15 - 4.18 and Table 4.5 it is observed that retrieved wave parameters from the wavelet analysis are close to the results from the FFT analysis as well as to the input data for velocity of encounter $u \in [0, 5]$ m/s. In addition, the standard deviations of the input and the CWT-derived wave direction, mean period, and peak frequency are calculated to be 9.7586°, 0.7027 s, and 0.0035 Hz, which are close to the respective values of 5.1704°, 0.4254 s, 0.0043 Hz derived from the FFT analysis.

Next, the 3-D FFT-based and 2-D CWT-based wave analysis algorithms are tested

with simulated data of different mean periods, T_{01} = 8, 10, 12, and 14 s. The sub-image sequence used in the wave analysis is acquired at the wave propagation direction ($\theta_{sub} = \theta_w$), 500 m away from the radar antenna (D_{sub} = 500 m). The wave direction is $\theta_w = 270°$ from true north. The significant wave height of the wave field is H_s = 3.5 m. The velocity of encounter of the wave field is u = 0 m/s.

Table 4.6: Retrieved Wave Parameters Using FFT- and CWT-based Algorithms at Mean Period T_{01} = 8 s, 10 s, 12 s, and 14 s.

Parameters	Input Data							
$T_{01_{in}}$ (s)	8.03		10.03		12.03		14.03	
u_{in} (m/s)	0		0		0		0	
$\theta_{u_{in}}$ (°)	-		-		-		-	
$\theta_{w_{in}}$ (°)	270		270		270		270	
$f_{p_{in}}$ (Hz)	0.0997		0.0797		0.0650		0.0551	
	Output Data							
Algorithms	FFT	CWT	FFT	CWT	FFT	CWT	FFT	CWT
$T_{01_{out}}$ (s)	8.76	9.14	9.94	9.48	11.65	11.77	13.18	13.82
u_{out} (m/s)	0.0141	n/a	0.0205	n/a	0.0124	n/a	0.0101	n/a
$\theta_{u_{out}}$ (°)	281.2937	n/a	159.4181	n/a	78.87	n/a	34.32	n/a
$\theta_{w_{out}}$ (°)	270.78	280.83	268.04	274.69	276.42	291.84	264.98	260.44
$f_{p_{out}}$ (Hz)	0.0948	0.0948	0.0800	0.0849	0.0747	0.0654	0.0653	0.0548

Figs. 4.19 (a) - 4.22 (a) present the input and derived 1-D frequency spectra, $E(f)$. Both Fourier and wavelet derived spectra recover the energy distribution correctly. However, it is observed that a second peak near $2f_p$ appears in the wavelet derived spectra for T_{01} = 10, 12, and 14 s (see Figs. 4.21 - 4.22 (a)). This may be explained by the effect of wave nonlinearity [79]. In addition, as suggested in Chapter 3, a scale resolution, χ, regulates the resolution of the wavelet series. If an underestimated χ is used, some energy components may not be retrieved successfully. Thus, based on simulated and field data tests, it is recommended that $\chi \in [0.9, 0.95]$ be used throughout the ocean wave analysis. However, this high-scale resolution may also result in a sec-

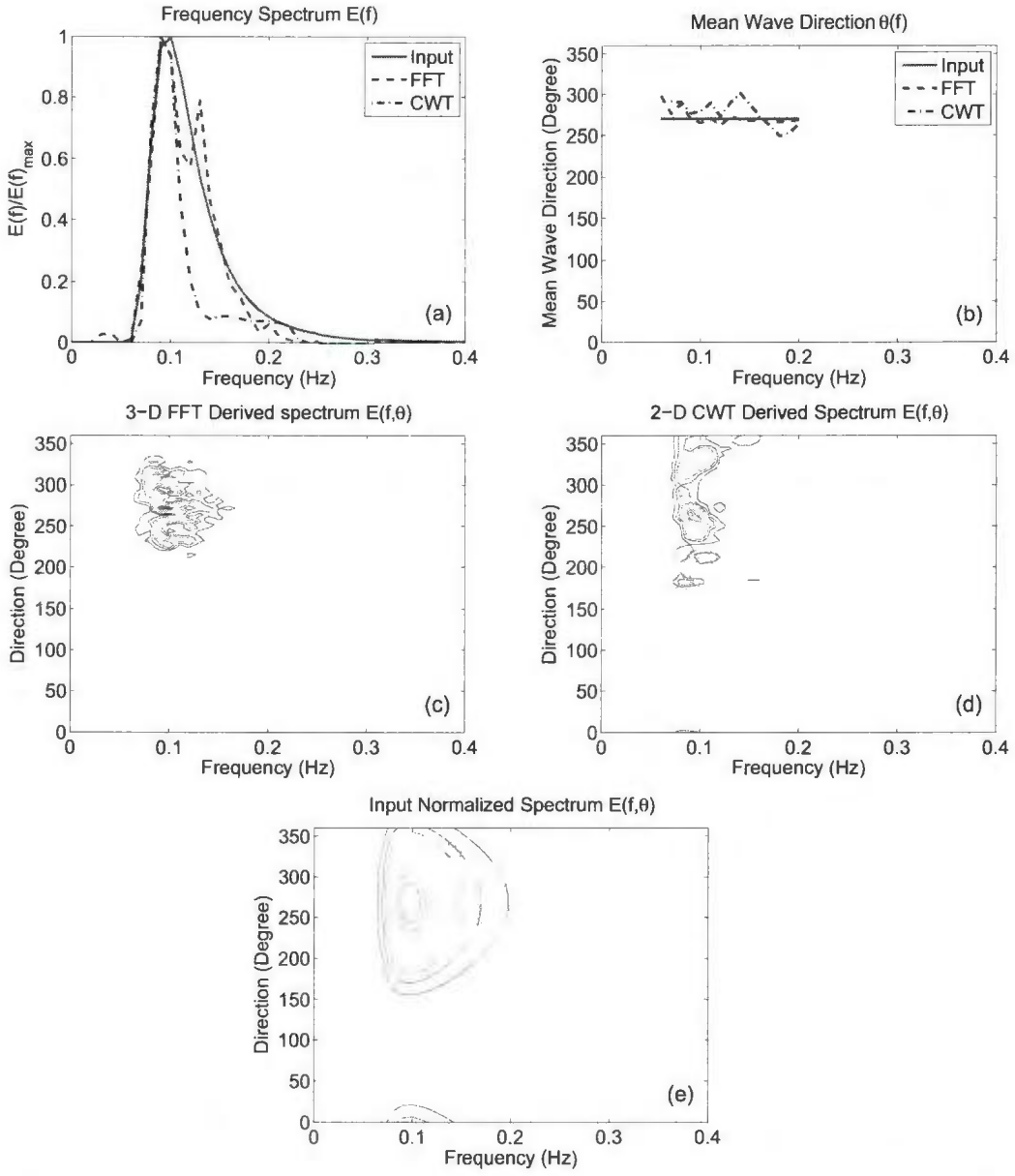

Figure 4.19: Comparison of derived spectra using 3-D FFT and 2-D CWT wave analysis with mean wave period $T_{01} = 8$ s: (a) Normalized frequency spectrum $E(f)$; (b) Mean wave direction spectrum $\theta(f)$; (c) 3-D FFT derived directional frequency spectrum $E(f, \theta)$; (d) 2-D CWT derived directional frequency spectrum $E(f, \theta)$; (e) Input directional frequency spectrum $E(f, \theta)$.

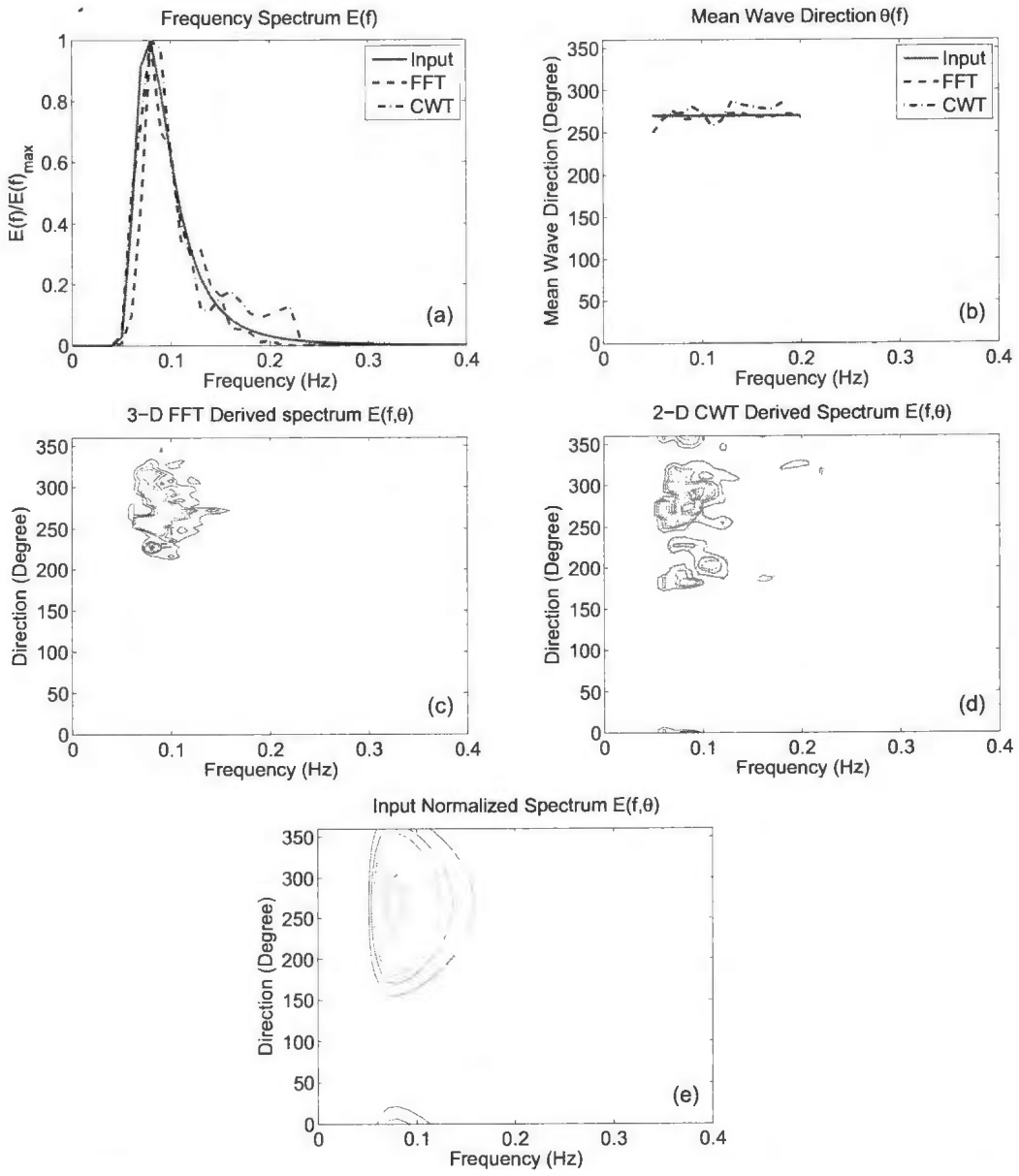

Figure 4.20: Comparison of derived spectra using 3-D FFT and 2-D CWT wave analysis with mean wave period $T_{01} = 10$ s.

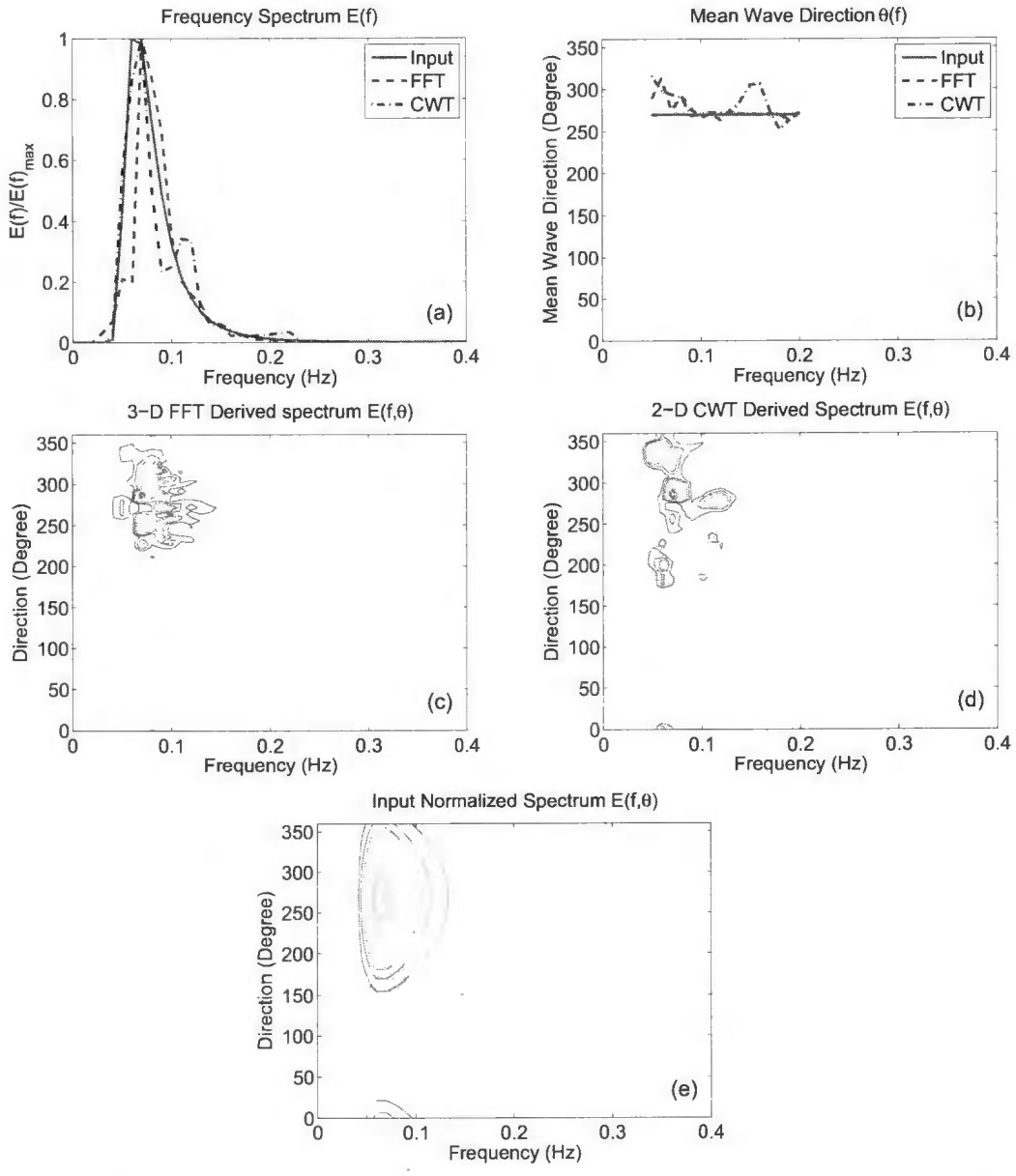

Figure 4.21: Comparison of derived spectra using 3-D FFT and 2-D CWT wave analysis with mean wave period $T_{01} = 12$ s.

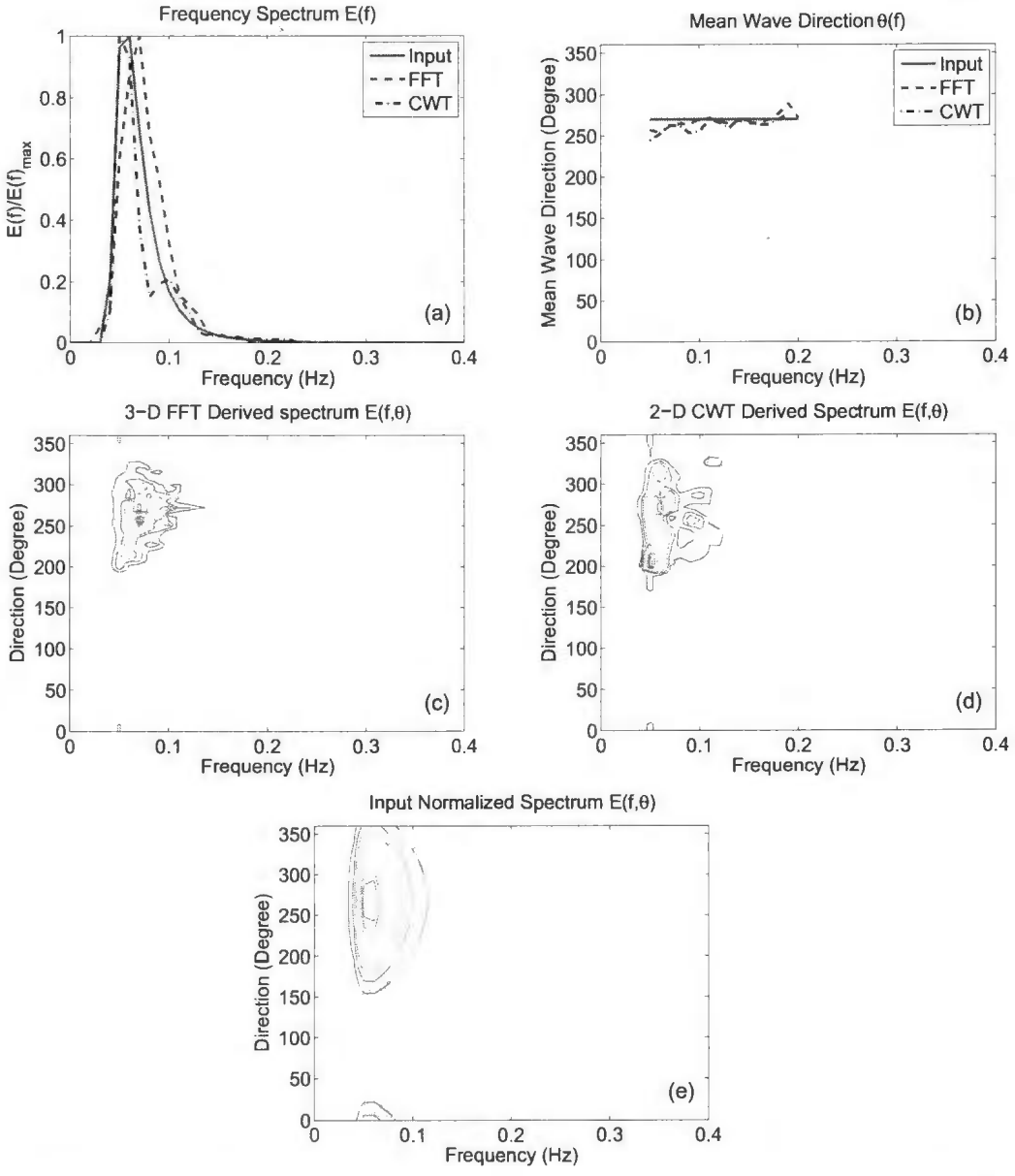

Figure 4.22: Comparison of derived spectra using 3-D FFT and 2-D CWT wave analysis with mean wave period $T_{01} = 14$ s.

ond peak. In this thesis, the second peaks are suppressed by the modified MTF (4.17). Thus, in some cases they cannot been observed (see Figs. 4.15 - 4.17 (a)). Figs. 4.19 (b) - 4.22 (b) show the comparison of the mean wave direction spectra $\theta(f)$. It is demonstrated from the figures that the derived mean wave direction spectra derived from both methods are close to the input curve. Figs. 4.19 (c)(d)(e) - 4.22 (c)(d)(e) show the directional-frequency spectra $E(f, \theta)$ retrieved from the Fourier and wavelet analysis as compared with the input spectra. It is observed from the comparisons that both the 3-D FFT-based and 2-D CWT-based wave analysis algorithms can be used to recover accurate energy distributions of wave fields with different mean periods.

The comparison between the input and retrieved wave parameters using the 3-D FFT-based and 2-D CWT-based wave analysis algorithms is found in Table 4.6. It is obvious from the table that both methods give reliable wave parameters from the simulated radar images for different mean wave periods.

After the analysis of wave information extraction using the 3-D FFT-based and 2-D CWT-based algorithms for various velocities of encounter and mean wave periods, the impact of the selection of sub-image position are investigated. As discussed in Chapter 2, for the simulations, the sub-image patches are selected with dimensions of 128×128 pixels at the wave propagation ($\theta_{sub} = \theta_w$) with a distance of 500 m from the radar antenna ($D_{sub} = 500$ m). Next, to examine their impact on the derived wave information, two groups of sub-image sequences are selected from different positions (different directions and distances) on the same series of generated radar images. Such discussions have been made in [1], [69]. The radar images are generated with a velocity of encounter of $u = 1.5$ m/s, $\theta_u = 270°$ from true North. The wave propagation direction θ_w is also chosen to be 270° from true North. The mean period of the wave field is taken as 10 s and a significant wave height of 3.5 m is used. In the data test, the first group of sub-image sequences is selected from the original radar

image series with a fixed distance D_{sub} = 500 m, and the directions of the sub-image are chosen as θ_{sub} = 0°, 45°, 90°, and 180°. The second group of sub-image sequences is selected from the original radar image series with a fixed direction of θ_{sub} = 0°, and the distances from the origin are taken to be D_{sub} = 200 m, 500 m, 800 m, and 1100 m.

Figs. 4.23 (f) - 4.26 (f) present the sub-image sequence position for the first group test. It is obvious from the 1-D frequency spectra $E(f)$ as depicted in Figs. 4.23 (a) - 4.26 (a) that the best results are obtained at θ_{sub} = 0°, which is the case when the sub-images are acquired at the wave propagation direction. When the sub-images are not selected at the wave direction, a second peak is often observed in the retrieved frequency spectrum, as shown in the FFT curves for the cases when θ_{sub} = 45°, 180°. In these cases, the derived peak frequency is less accurate, as indicated in Table 4.7 which lists the derived wave and current parameters at different selections of sub-image direction θ_{sub}.

Table 4.7: Retrieved Wave Parameters using FFT- and CWT-based Algorithms with the Selection of Sub-image Sequence at D_{sub} = 500, θ_{sub} = 0°, 45°, 90°, and 180°

Parameters	Input Data							
θ_{sub} (°)	0°		45°		90°		180°	
D_{sub} (m)	500		500		500		500	
u_{in} (m/s)	1.5		1.5		1.5		1.5	
$\theta_{u_{in}}$ (°)	270		270		270		270	
$\theta_{w_{in}}$ (°)	270		270		270		270	
$T_{01_{in}}$ (s)	10.03		10.03		10.03		10.03	
$f_{p_{in}}$ (Hz)	0.0797		0.0797		0.0797		0.0797	
	Output Data							
Algorithms	FFT	CWT	FFT	CWT	FFT	CWT	FFT	CWT
u_{out} (m/s)	1.5221	n/a	1.5035	n/a	1.4954	n/a	1.5196	n/a
$\theta_{u_{out}}$ (°)	267.97	n/a	267.85	n/a	269.75	n/a	269.59	n/a
$\theta_{w_{out}}$ (°)	268.14	271.08	245.86	255.91	267.15	279.56	273.94	271.64
$T_{01_{out}}$ (s)	10.45	10.69	10.85	10.95	10.50	10.54	10.49	10.44
$f_{p_{out}}$ (Hz)	0.0846	0.0847	0.0700	0.0794	0.0804	0.0600	0.0810	0.0700

Table 4.8: Retrieved Wave Parameters Using FFT- and CWT-based Algorithms with the Selection of Sub-image Sequence at $\theta_{sub} = 0^{\circ}$. D_{sub} = 200 m, 500 m, 800 m, 1100 m.

Parameters	Input Data							
D_{sub} (m)	200		500		800		1100	
θ_{sub} (°)	0°		0°		0°		0°	
u_{in} (m/s)	1.5		1.5		1.5		1.5	
$\theta_{u_{in}}$ (°)	270		270		270		270	
$\theta_{w_{in}}$ (°)	270		270		270		270	
$T_{01_{in}}$ (s)	10.03		10.03		10.03		10.03	
$f_{p_{in}}$ (Hz)	0.0797		0.0797		0.0797		0.0797	
	Output Data							
Algorithms	FFT	CWT	FFT	CWT	FFT	CWT	FFT	CWT
u_{out} (m/s)	1.5279	n/a	1.5221	n/a	1.5081	n/a	1.4992	n/a
$\theta_{u_{out}}$ (°)	272.85	n/a	267.97	n/a	266.21	n/a	268.51	n/a
$\theta_{w_{out}}$ (°)	265.72	275.80	268.14	271.08	276.42	268.72	268.97	271.47
$T_{01_{out}}$ (s)	10.33	9.78	10.45	10.69	10.69	11.06	10.90	11.74
$f_{p_{out}}$ (Hz)	0.0850	0.0807	0.0846	0.0847	0.0846	0.0700	0.0848	0.0747

Figs. 4.27 (f) - 4.30 (f) present the sub-image sequence position for the second group test as noted above for the case involving a fixed $\theta_{sub} = 0^{\circ}$ but various values of D_{sub}. By comparing the derived spectra of $E(f)$, $\theta(f)$, and $E(f, \theta)$ from sub-images at different distances as shown in Figs. 4.27 - 4.30, no obvious advantages can be observed at any distance D_{sub}. It appears that the choice of the sub-image distance has little impact on the wave spectra derived from either method.

The wave and current parameters derived from sub-images at different distances are next investigated (see results in Table 4.8). It is observed that reliable current information and wave direction can be derived for different sub-image distances. However, if the sub-images are acquired far away from the radar antenna, it is found that an overestimated mean period is obtained. The best result for mean period is derived at D_{sub} = 200 m. This makes sense because the further the ocean waves are away from the radar antenna, the more likely they are to be shadowed by higher waves

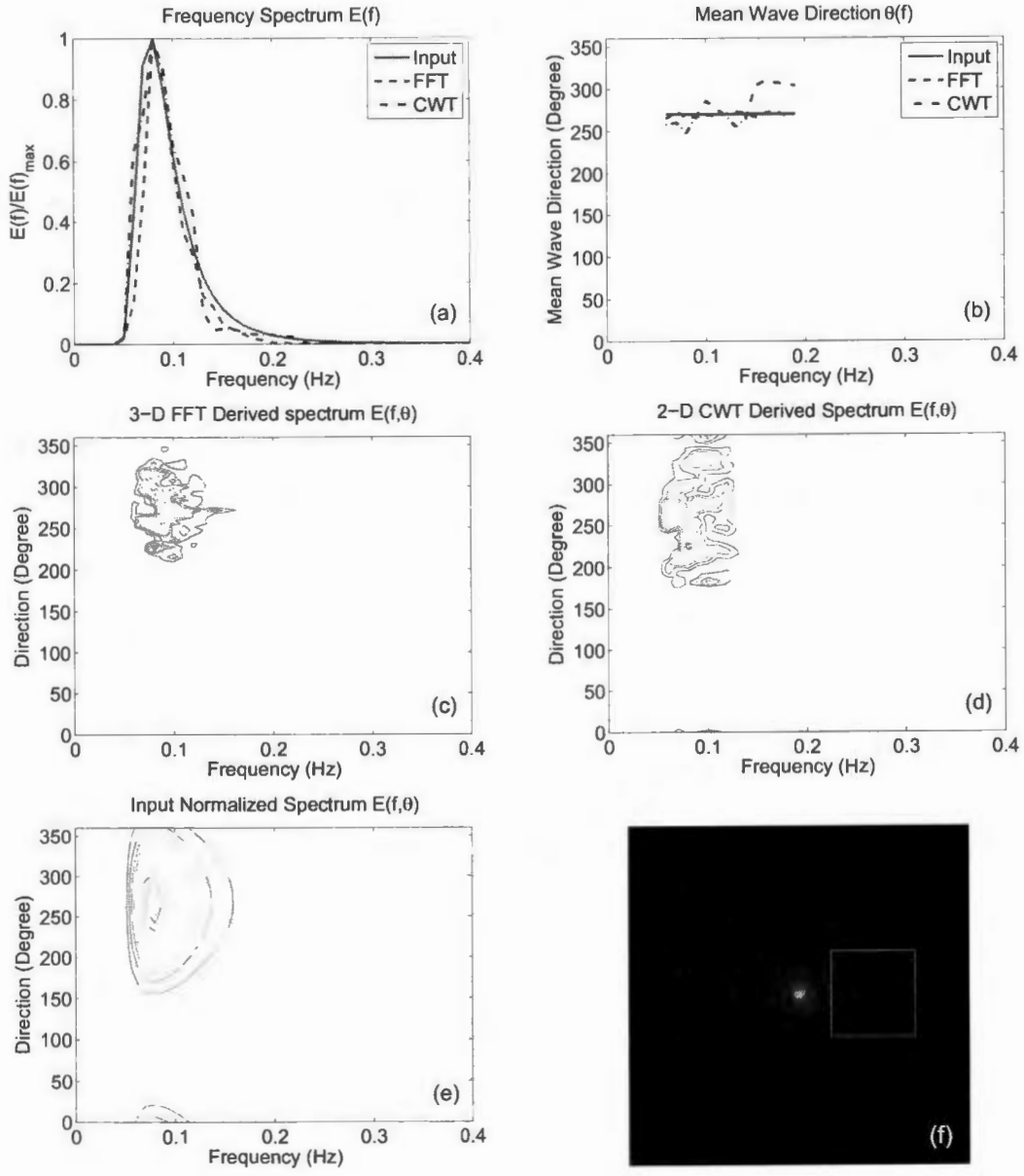

Figure 4.23: Comparison of derived spectra using 3-D FFT and 2-D CWT wave analysis with the selection of sub-image sequence at $D_{sub} = 500$, $\theta_{sub} = 0°$: (a) Normalized frequency spectrum $E(f)$; (b) Mean wave direction spectrum $\theta(f)$; (c) 3-D FFT derived directional frequency spectrum $E(f,\theta)$; (d) 2-D CWT derived directional frequency spectrum $E(f,\theta)$; (e) Input directional frequency spectrum $E(f,\theta)$; (f) Selection of the sub-image sequence.

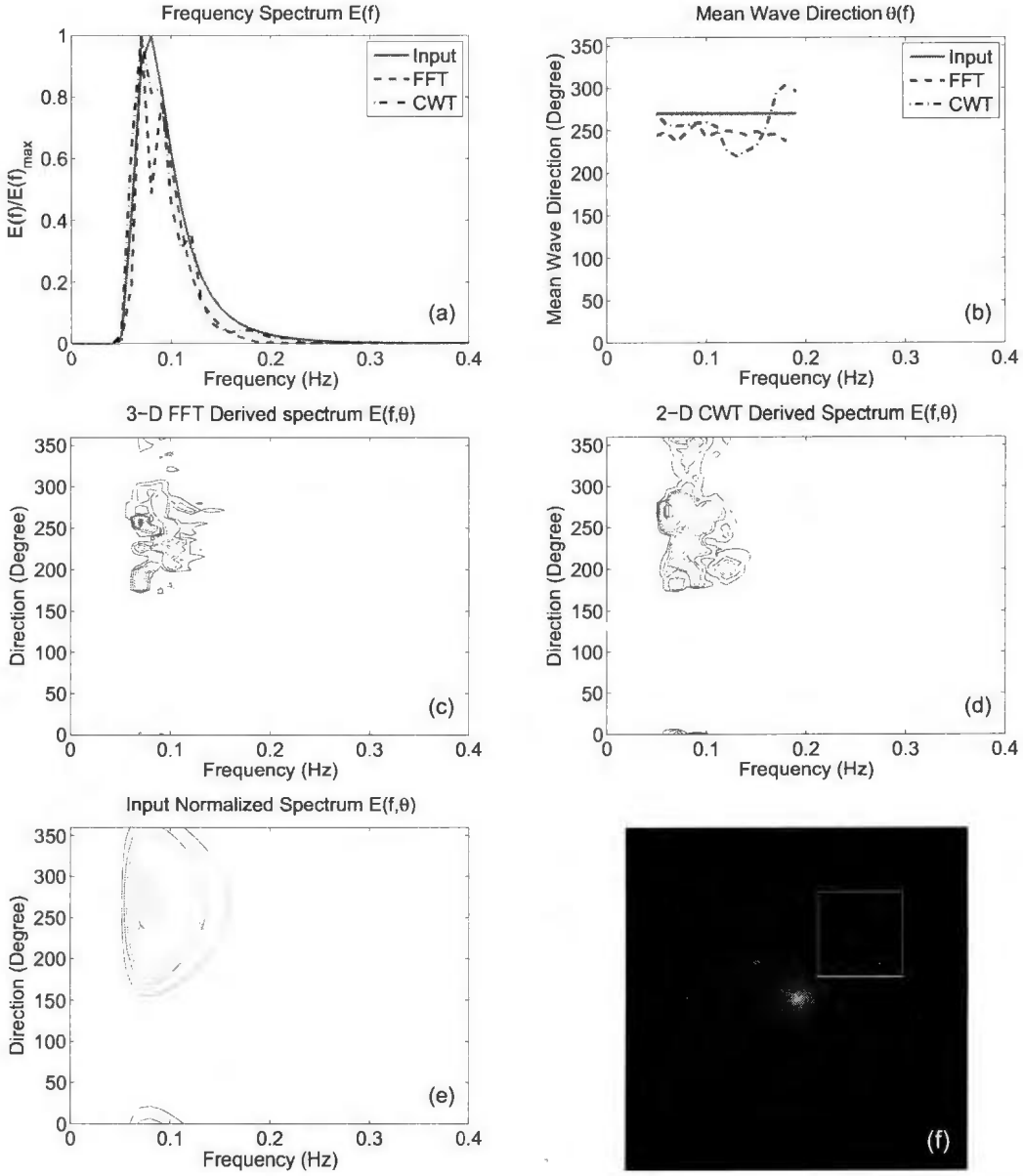

Figure 4.24: Comparison of derived spectra using 3-D FFT and 2-D CWT wave analysis with the selection of sub-image sequence at $D_{sub} = 500$, $\theta_{sub} = 45°$.

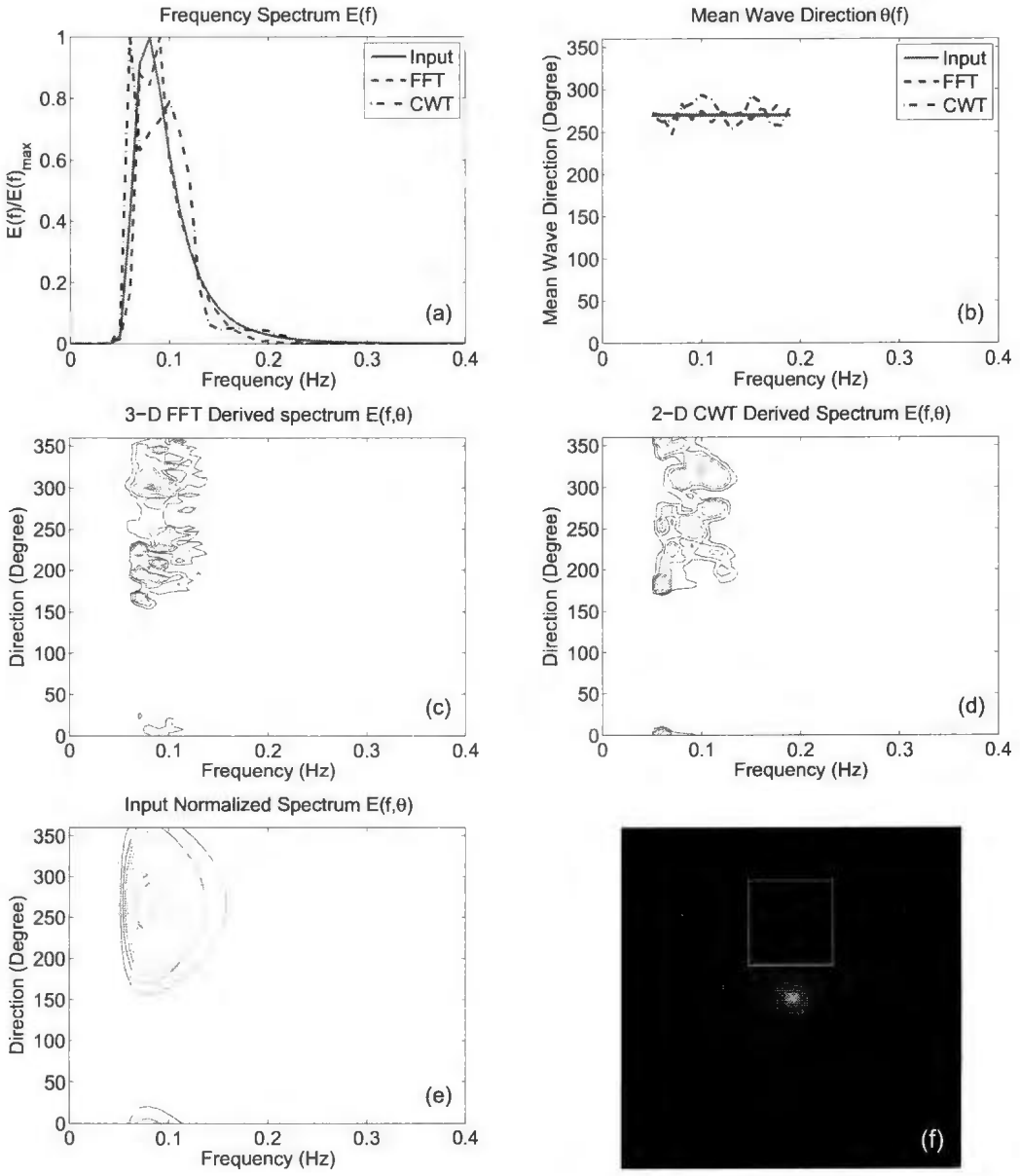

Figure 4.25: Comparison of derived spectra using 3-D FFT and 2-D CWT wave analysis with the selection of sub-image sequence at $D_{sub} = 500$, $\theta_{sub} = 90°$.

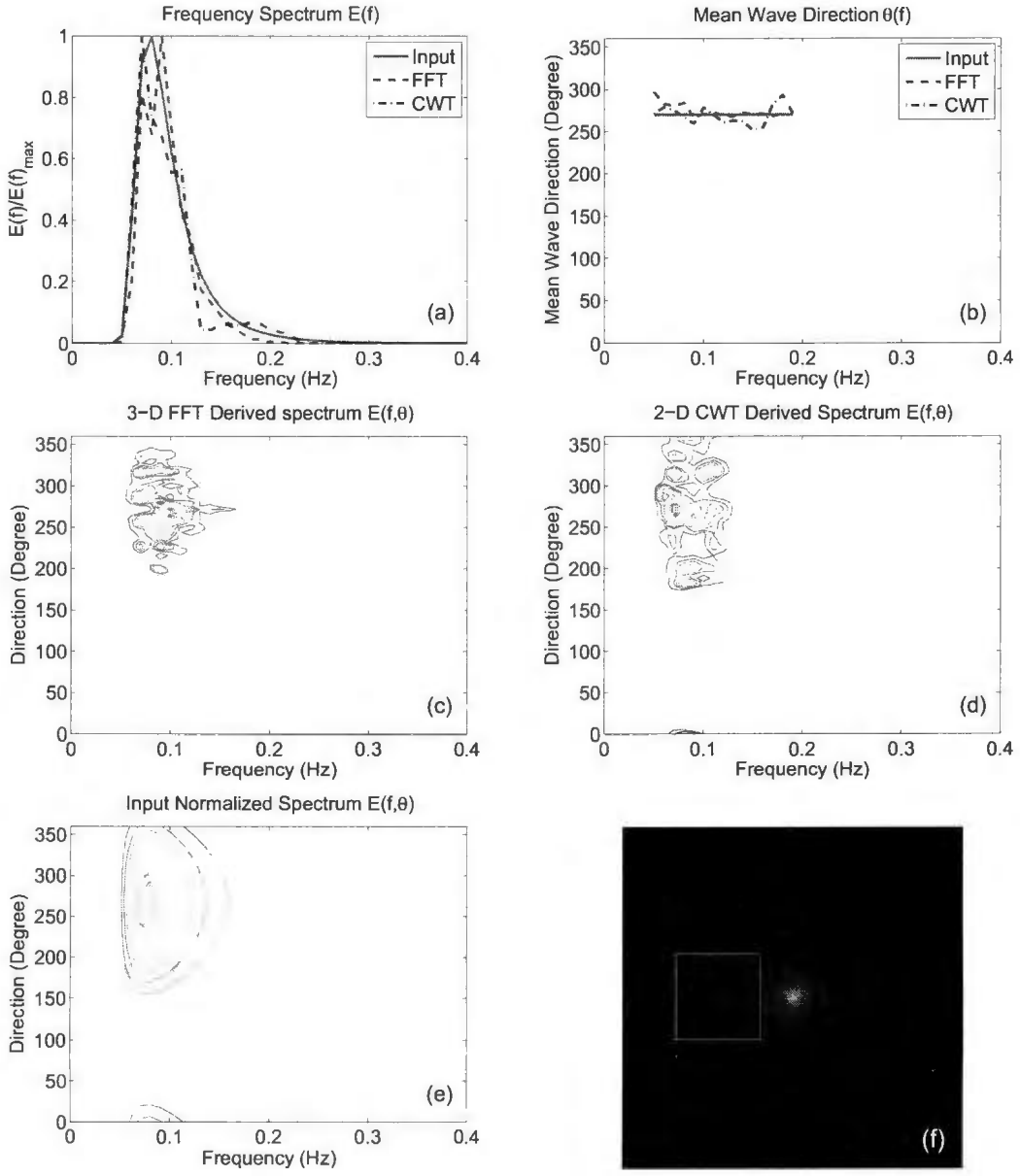

Figure 4.26: Comparison of derived spectra using 3-D FFT and 2-D CWT wave analysis with the selection of sub-image sequence at $D_{sub} = 500$, $\theta_{sub} = 180°$.

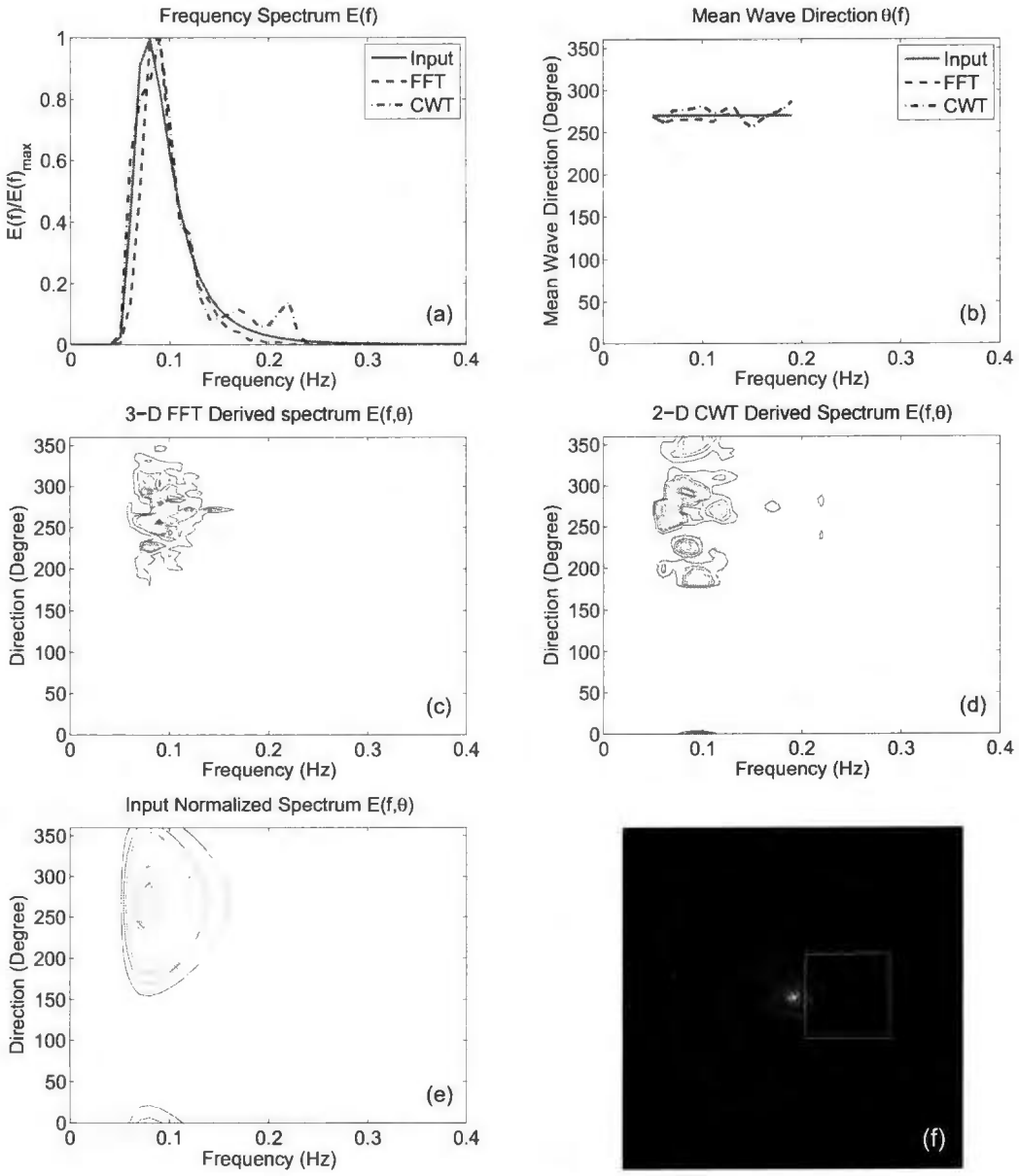

Figure 4.27: Comparison of derived spectra using 3-D FFT and 2-D CWT wave analysis with the selection of sub-image sequence at $\theta_{sub} = 0°$, $D_{sub} = 200$.

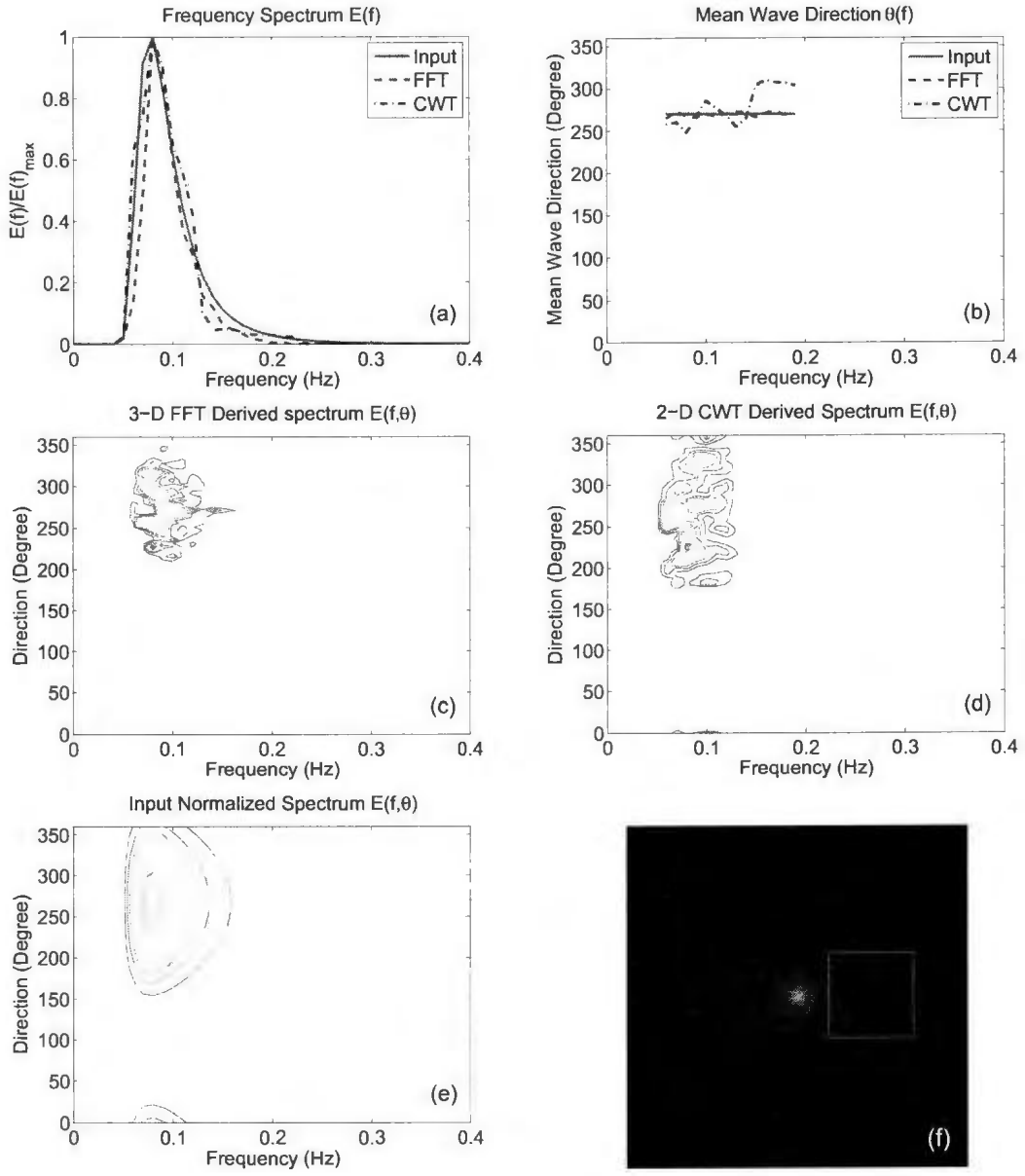

Figure 4.28: Comparison of derived spectra using 3-D FFT and 2-D CWT wave analysis with the selection of sub-image sequence at $\theta_{sub} = 0°$, $D_{sub} = 500$.

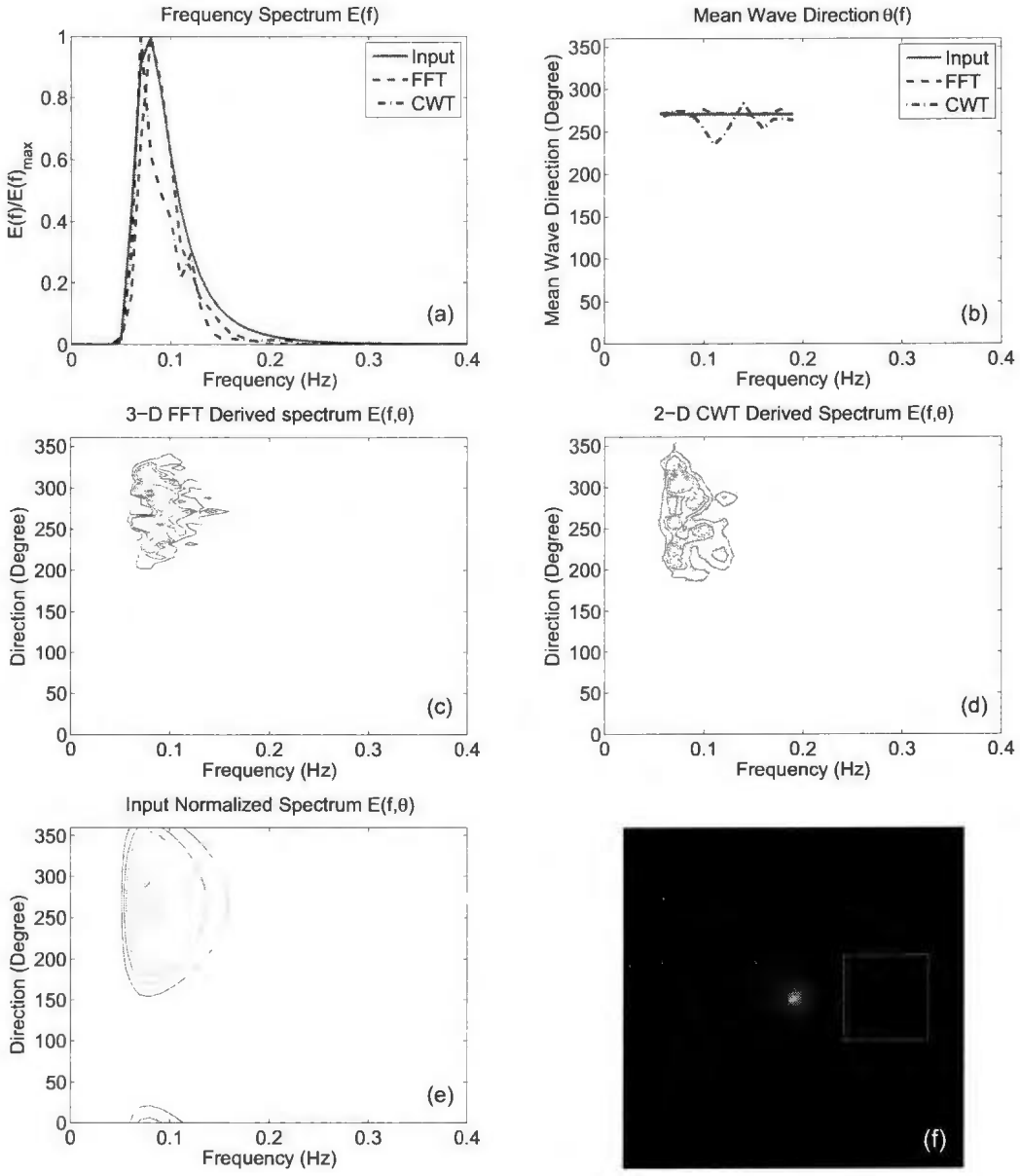

Figure 4.29: Comparison of derived spectra using 3-D FFT and 2-D CWT wave analysis with the selection of sub-image sequence at $\theta_{sub} = 0°$, $D_{sub} = 800$.

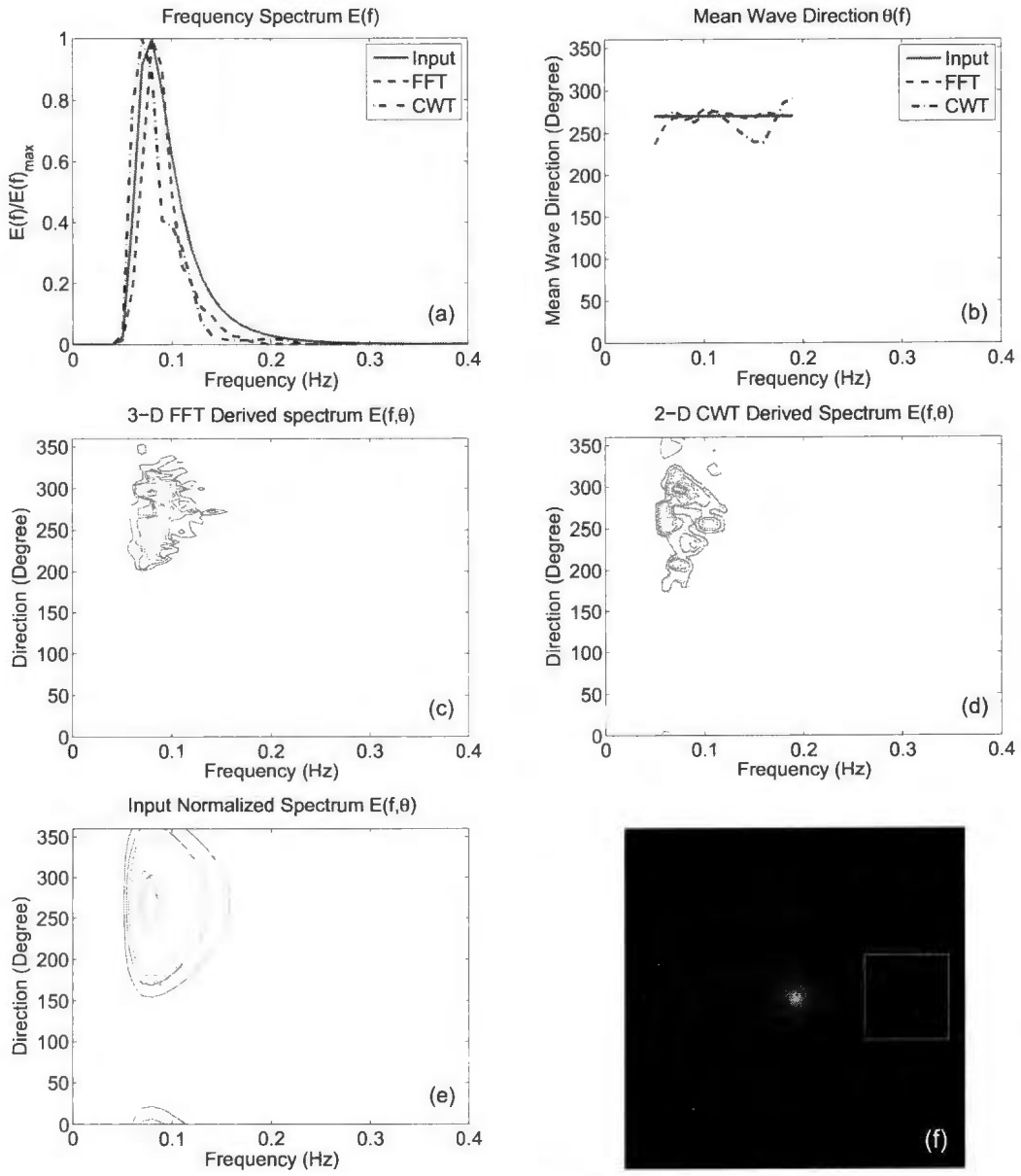

Figure 4.30: Comparison of derived spectra using 3-D FFT and 2-D CWT wave analysis with the selection of sub-image sequence at $\theta_{sub} = 0°$, $D_{sub} = 1100$.

(see Fig. 4.1). Also, the intensity of the radar image will be very low near the edge since the back-scattered energy is inversely proportional to the fourth power of the distance between the radar and the target [42]. Thus, the ocean wave information retrieved from sub-images near the edge of the original image is expected to be less accurate. On the other hand, it is not recommended to select sub-images too close to the radar antenna because of the severe distortions of wave fronts due to the tilt modulation [51].

4.2 Field Data Test

Having tested both the FFT- and CWT-based algorithms using simulated data, they are next applied to H-pol and V-pol field data collected on the east coast of Canada. The impact which polarization has on the results is considered, and outcomes are compared with information gathered from *in situ* instrumentation.

4.2.1 Experimental Data Collection

Dual-polarized radar field data collected on Dec. 15 and Dec. 20, 2010 at Skerries Bight near the St. John's Harbor on the east coast of Canada were used for wave analysis. Data from a TRIAXYS wave buoy and an acoustic Doppler current profiler (ADCP) collected at the same time were used as the ground truth [86], [93]. The ADCP provided current information for 50 bins starting at approximately 1.75 m. With the extent of each bin were set being 1 m, the maximum depth for current measurement is about 52 m. The accuracy of the ADCP was ± 0.04 m/s and $\pm 3^{\circ}$ for current speed and direction, respectively. The ADCP current results were averaged every half an hour [85].

The radar and buoy sites are shown in Fig. 4.31. It is assumed that the water is

deep enough for the deep water dispersion relationship (2.4). A typical V-pol X-band nautical radar image collected on Dec. 15 is provided in Fig. 4.32. The white box of dimensions 128 × 128 pixels shown on the figure depicts a typical sub-image used for wave retrieval. The center of this sub-image indicates the position of the moored wave buoy. Detailed information on the radar and buoy is given in Table 4.9.

Table 4.9: Radar and Buoy Data Information

Radar System Specification	
Collecting date	12/15/2010; 12/20/2010
Starting time	16:30:02 (GMT); 13:30:57 (GMT)
Radar location	47.5934N 52.6634W
Polarization	Dual Polarization
Antenna angular speed	48 r.p.m.
The radar range resolution	7.51 m
Generated Image Size	1024 × 1024 pixels
Buoy Information	
Collecting date	12/15/2010; 12/20/2010
Starting time	16:30:00 (GMT); 13:30:00 (GMT)
Buoy location	47.3362N 52.4210W

In the 3-D FFT-based analysis, 30 sequences consisting of 32 consecutive radar sub-images were used for current and wave information extraction. For the given radar operating parameters, this corresponds to a period of 20 minutes for each data set. The parameter used in the MTF process for FFT-based field data analysis is modified as

$$\mu = \begin{cases} -0.96, & \text{if } |k_{xy}| \leq e^{-2.2} \\ -1.2, & \text{otherwise} \end{cases} \tag{4.18}$$

Based on the information provided, the parameters assigned for the wavelet analysis are determined and listed in Table 4.10. As described in Chapter 3, an initial value of $j_0 = 1.4$ and $\Delta j = 0.2$ are used for $\Delta x = 10.5$ m and $N_x = 128$. As listed in Table 4.9, the radar range resolution is $\Delta x = 7.51$ m. Therefore, the corresponding

Table 4.10: Wavelet Parameters Configuration

$\vec{k}_0$	(6.0)
λ	0.9
η	0.01
$\vec{b}_0$	$(1,1)$
N_x	128
β_0	1.001
$\Delta\beta$	0.143

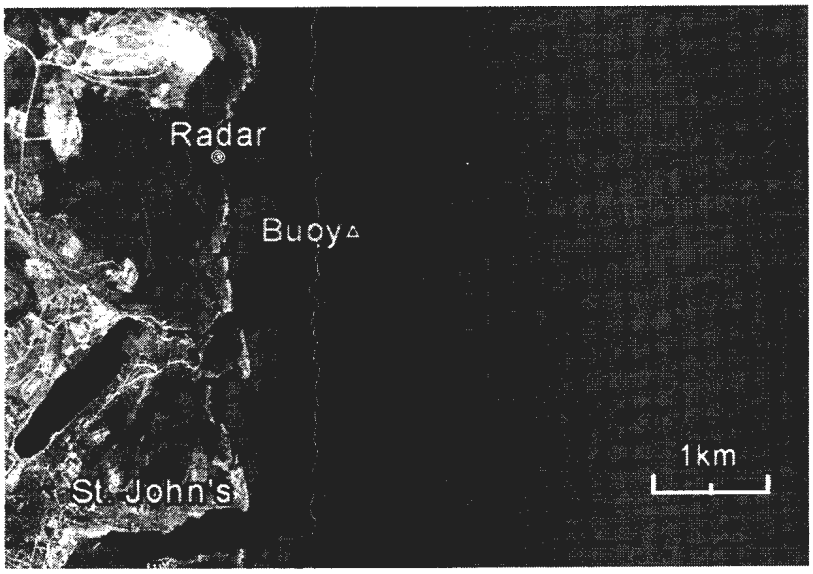

Figure 4.31: Radar and buoy sites

starting β_0 and $\Delta\beta$ used in this field data test can be calculated from equation (3.27) to be 1.001 and 0.143, respectively. The MTF expression for the 2-D CWT-based field data test is provided as

$$\mu = \begin{cases} -1.42, & \text{if } |k_{xy}| \leq e^{-2.75} \\ -1.2, & \text{otherwise} \end{cases} \tag{4.19}$$

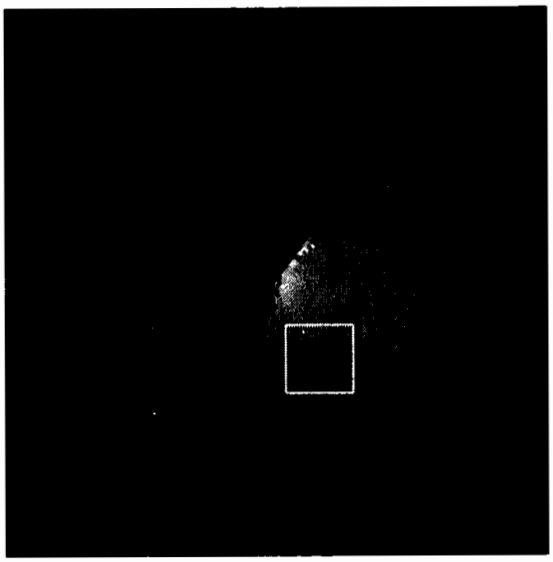

Figure 4.32: An example of V-pol X-band nautical radar plan position indicator (PPI) image from Dec.15, 2010 and the sub-image selection for wavelet analysis.

4.2.2 Result and Discussion

Near-surface current information is estimated first from the Fourier analysis, using the LS, iterative LS and NSP methods. For the field data collected from a land-based radar, the vessel's velocity $\vec{u}_s = 0$, and thus the retrieved velocity of encounter $\vec{u}_e$ is the true value of the near-surface current velocity $\vec{u}_c$. The ADCP record measured from the second bin (2.75 to 3.75 m below the sea surface) is used as ground truth. The comparison of the derived results of the current speed and direction from the H-pol and V-pol radar data and ADCP record on Dec. 15 and 20, 2010 are shown in Figs. 4.33 - 4.36. On Dec. 15, the current speed and direction obtained from the ADCP record were 0.35 m/s and 57.4°, respectively; on Dec. 20, the speed and direction measured from the ADCP were 0.47 m/s and 97.4°, respectively. In Figs. 4.33 - 4.36, the (black) solid line represents the ADCP record; the (green) dot line with circles represents the derived current information using the LS method; the

(red) dash line with diamonds indicates the derived current information using the iterative LS method; and the (blue) dash-dot line with asterisks shows the derived current information using the NSP method. It is obvious from the figures that the LS method provides only a rough estimation of the current information with large errors appearing in both speed and direction. The iterative LS and NSP methods generate more accurate and stable surface current than those obtained using the LS method. Results from the iterative LS and NSP methods also show good agreement with each other and with the ADCP record. However, by comparing the H-pol and V-pol results (Figs. 4.33, 4.35 vs. Figs. 4.34, 4.36), it is observed that the derived current information from the V-pol radar data is more accurate. The large error in the results derived from the H-pol data may be due to the low sea state during the measurement period [85]. Although the iterative LS method determines the current information based on the first guess of the LS estimation, it is observed from the figures that the results of the iterative LS method are not affected when the initial guess from the classical LS is poor.

Table 4.11: Error Analyses of the Derived Current Information of the Field Data Test

Data (s)	Algorithms	ΔV_m (m/s)	ΔV_{sd} (m/s)	ΔD_m (°)	ΔD_{sd} (°)
Dec.15 H-pol	LS	-0.1765	0.1107	109.8837	135.9728
	Iterative LS	-0.2964	0.0210	78.0619	47.5012
	NSP	-0.2967	0.0231	72.0796	26.3543
Dec.15 V-pol	LS	0.5183	0.6293	60.0588	106.3091
	Iterative LS	0.0313	0.0571	12.7988	14.4612
	NSP	0.0120	0.0386	13.9047	16.4557
Dec.20 H-pol	LS	-0.1330	0.2589	78.0894	86.7100
	Iterative LS	-0.2709	0.0391	76.6812	36.6118
	NSP	-0.2713	0.0517	59.2753	40.9942
Dec.20 V-pol	LS	0.1125	-9.5439	1.0458	65.1157
	Iterative LS	-0.0446	0.0559	-6.6970	8.9025
	NSP	-0.0507	0.0661	-7.4697	9.9323

The error analyses result is listed in Table 4.11, where ΔV_m and ΔV_{sd} are the mean

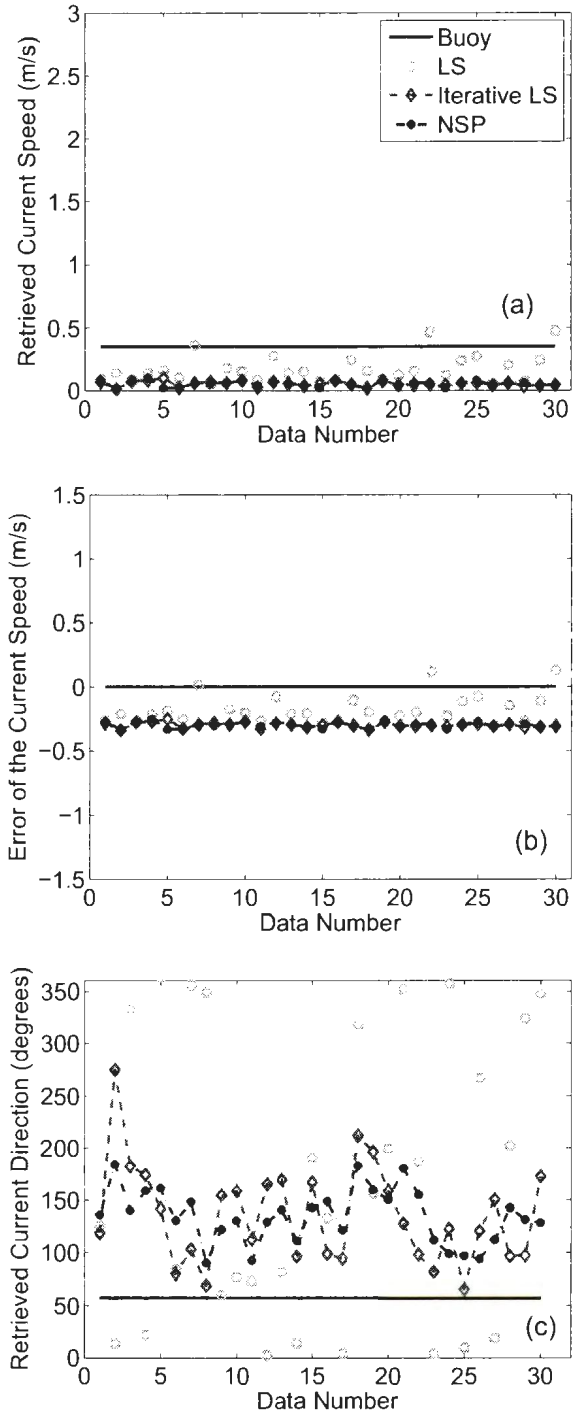

Figure 4.33: Results of derived surface currents from the Dec.15 H-pol data: (a) Derived current speed; (b) Errors of the derived current speed; (c) Derived current direction.

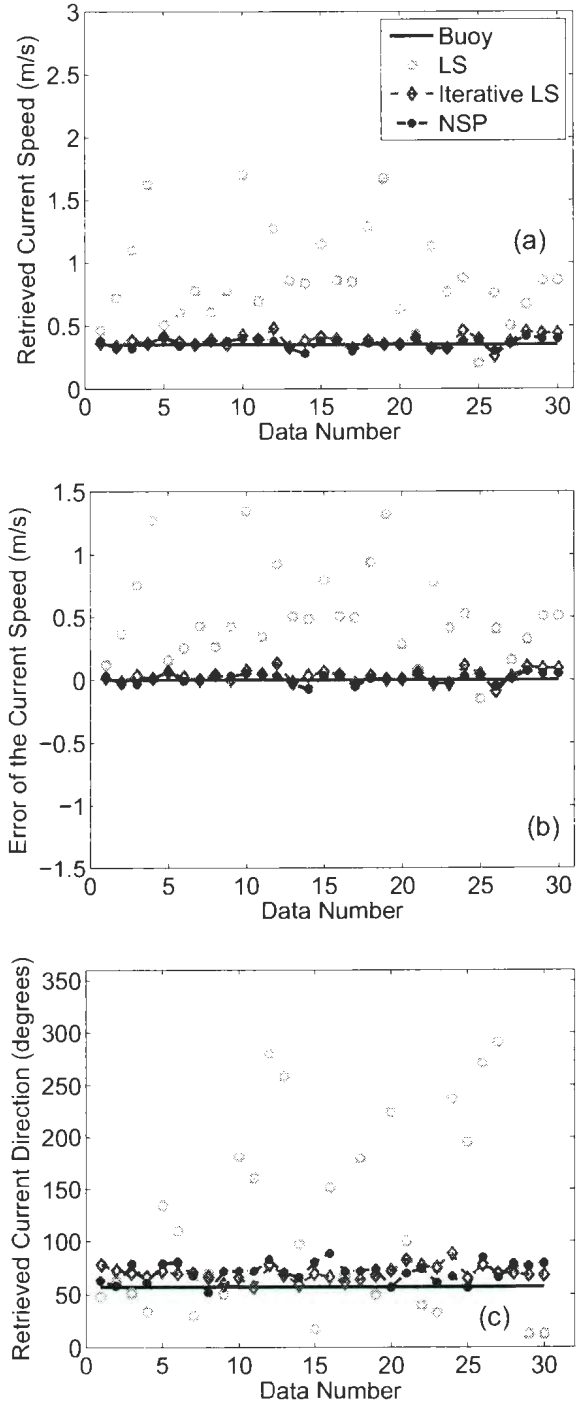

Figure 4.34: Results of derived surface currents from the Dec.15 V-pol data.

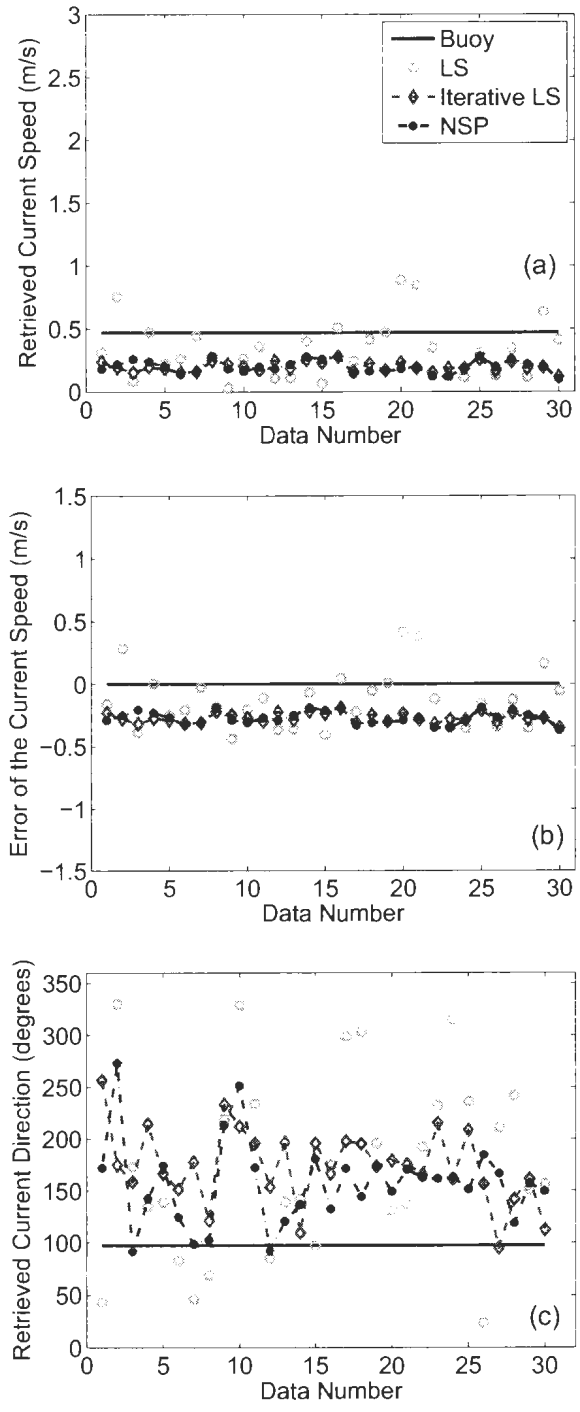

Figure 4.35: Results of derived surface currents from the Dec.20 H-pol data.

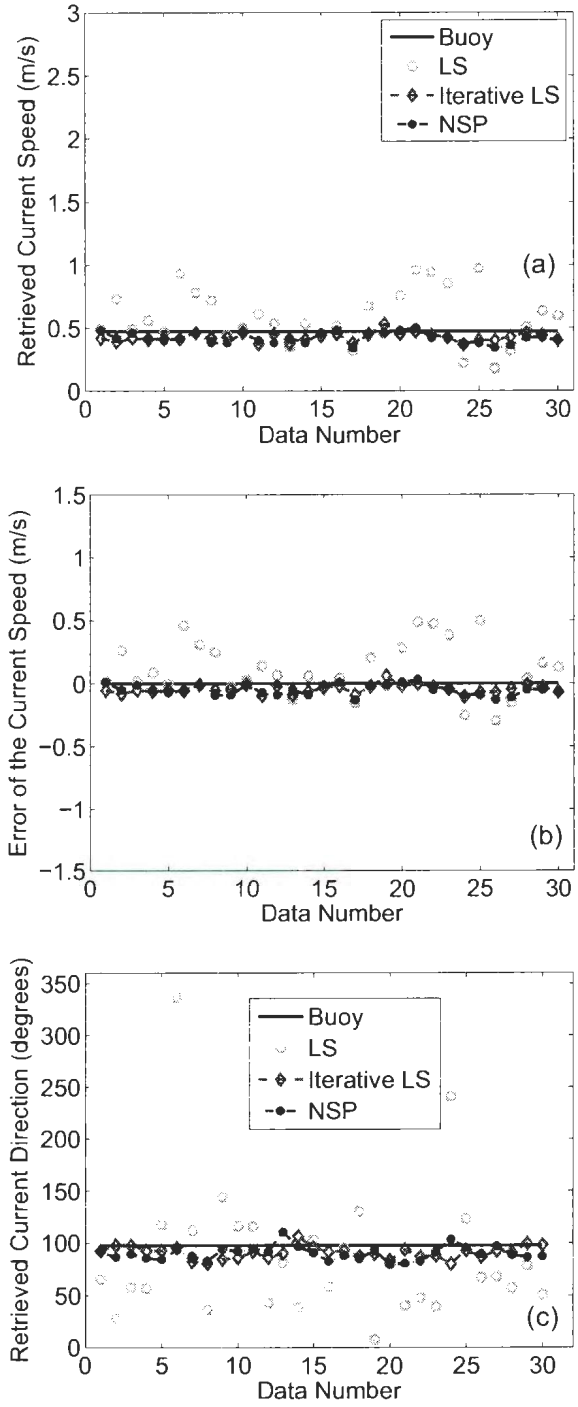

Figure 4.36: Results of derived surface currents from the Dec.20 V-pol data.

difference and standard deviation between the retrieved current speed and the ADCP record. ΔD_m and ΔD_{sd} are the mean difference and standard deviation of the current direction. From the data collected on Dec. 15, it is observed that the mean difference in the current speed derived using the LS method on the H-pol data (−0.1765 m/s) is slightly smaller than the mean difference in current speed using the iterative LS (−0.2964 m/s) and NSP (−0.2967 m/s) methods. This is because the current speed is underestimated with the iterative LS and NSP methods from the H-pol data, while the LS method provides a rough estimation and the derived points are distributed on both sides of the ADCP data, resulting in a better ΔD_m. However, it is obvious from the derived current direction that the results of the LS method are not reliable, with a difference of over 109.88°. For this H-pol data, the differences in the current directions obtained from the iterative LS and NSP methods as compared with that from the ADCP record are still quite large, being 78.07° and 72.07°, respectively. However, from the table, it may be observed that the iterative LS and NSP methods produce much more accurate results from the V-pol data. The mean current speed differences of the iterative LS and NSP methods are −0.0313 m/s and −0.0120 m/s, respectively, and both are better than those from the LS estimation (−0.5183 m/s). The direction differences of the LS, iterative LS and NSP methods are 60.05°, 12.79°, and 13.90°, respectively. A similar analysis can be observed from the results of the radar data collected on Dec. 20. The mean current speed differences of the H-pol data are −0.2709 m/s and −0.2713 m/s for the iterative LS and NSP methods, respectively. Much smaller mean speed differences of −0.0446 m/s, and −0.0507 m/s, respectively, are derived from the V-pol data. The current direction differences of the H-pol data are 76.68° and 59.27° for the iterative LS and NSP methods. For the V-pol data, the mean direction differences of the two algorithms are only −6.69° and −7.46°. In addition, from the comparisons of standard deviation, it is found that the iterative

LS and NSP methods provide robust current estimation results, with much smaller ΔV_{sd} than that from the LS method.

During the field data test, a 20-minute radar time series was used for both 2-D CWT and 3-D FFT analysis. The results were averaged to acquire the directional-frequency spectrum $E(f, \theta)$ in each case. For both methods, wave parameters calculated from these two averages are listed in Table 4.12, in which the *in situ* wave buoy results are also included. It is obvious that the wave direction, θ_w, and peak frequency, f_p, retrieved using both methods are close to those from the buoy record. The mean periods derived from the radar data using both algorithms are slightly larger than the *in situ* buoy recorded value.

Table 4.12: Comparison of Derived Parameters from Dual-pol Radar Data and Buoy Records

Wave parameters	Wave direction	Mean period	Peak frequency
Date	Dec. 15, 2010		
3-D FFT (H-pol)	63.25°	7.42 s	0.1053 Hz
2-D CWT (H-pol)	61.39°	7.78 s	0.1096 Hz
3-D FFT (V-pol)	63.72°	7.93 s	0.1053 Hz
2-D CWT (V-pol)	73.30°	7.74 s	0.1047 Hz
Buoy Record	60.47°	6.39 s	0.1025 Hz
Date	Dec. 20, 2010		
3-D FFT (H-pol)	38.11°	10.76 s	0.0850 Hz
2-D CWT (H-pol)	61.62°	10.45 s	0.0796 Hz
3-D FFT (V-pol)	39.23°	11.0 s	0.0804 Hz
2-D CWT (V-pol)	62.56°	10.42 s	0.0794 Hz
Buoy Record	53.63°	9.42 s	0.0746 Hz

The surface current velocity cannot be obtained from the 2-D CWT based algorithm. Thus, the band-pass filtering process that is designed to eliminate the energy offset due to surface current in the 3-D Fourier analysis is not applicable in the wavelet analysis. However, in this data set, the wavelet analysis provides similar results to the Fourier method because the currents, as discussed in [85], are relatively small ($u \approx 0.35$ m/s on Dec. 15 and $u \approx 0.47$ m/s on Dec. 20) so that they will not

significantly affect the wave field energy distribution.

Figs. 4.37 - 4.40 show the spectra derived from both the 2-D CWT and 3-D FFT algorithms using the dual-polarized radar data collected on Dec. 15 and 20, 2010. The wave buoy information recorded at the same time is also sketched in the figures. It is clear that a second peak near 0.18 Hz appears in the Dec. 15 buoy record of the 1-D frequency spectra ((a) in Figs 4.37, 4.38). The energy of this second peak is detected by the enhanced 3-D FFT-based algorithm which considered the aliasing and harmonic effects in the wave field analysis. However, this second peak is not shown in the recovered curve from the 2-D CWT-based algorithm. This is mainly because the band-pass filtering process is not applied in the wavelet analysis to back-fold the aliased energy components due to the Nyquist limit. Also, the introduction of the modified MTF function as described in (4.19) further suppresses the energy near the frequency components of $2f_p$. In addition, it is observed from Fig. 4.37 and Fig. 4.38 (a) that both methods fail to recover the energy of the higher frequency components ($f > 0.28$ Hz). This results in the overestimated mean wave period.

It is demonstrated by comparing the mean wave direction spectra ((b) in Figs. 4.37 - 4.40) that the wave directions retrieved using both methods are close to those obtained from the buoy data. However, by comparing the derived mean wave direction spectra, it is observed that wavelet analysis produces better results in $\theta(f)$ for both large and small frequency components.

In general, the 2-D directional-frequency spectra ((c)-(e) in Figs. 4.37 - 4.40) derived by both methods recovered the energy distribution correctly. The peak frequencies of the radar-derived spectra using both methods are also within 0.01 Hz of those obtained from the buoy reference.

In summary, it is verified through the comparison of V-pol and H-pol derived results that vertically polarized transmission provides better current information. The

wave results extracted from V-pol data and H-pol data do not differ significantly.

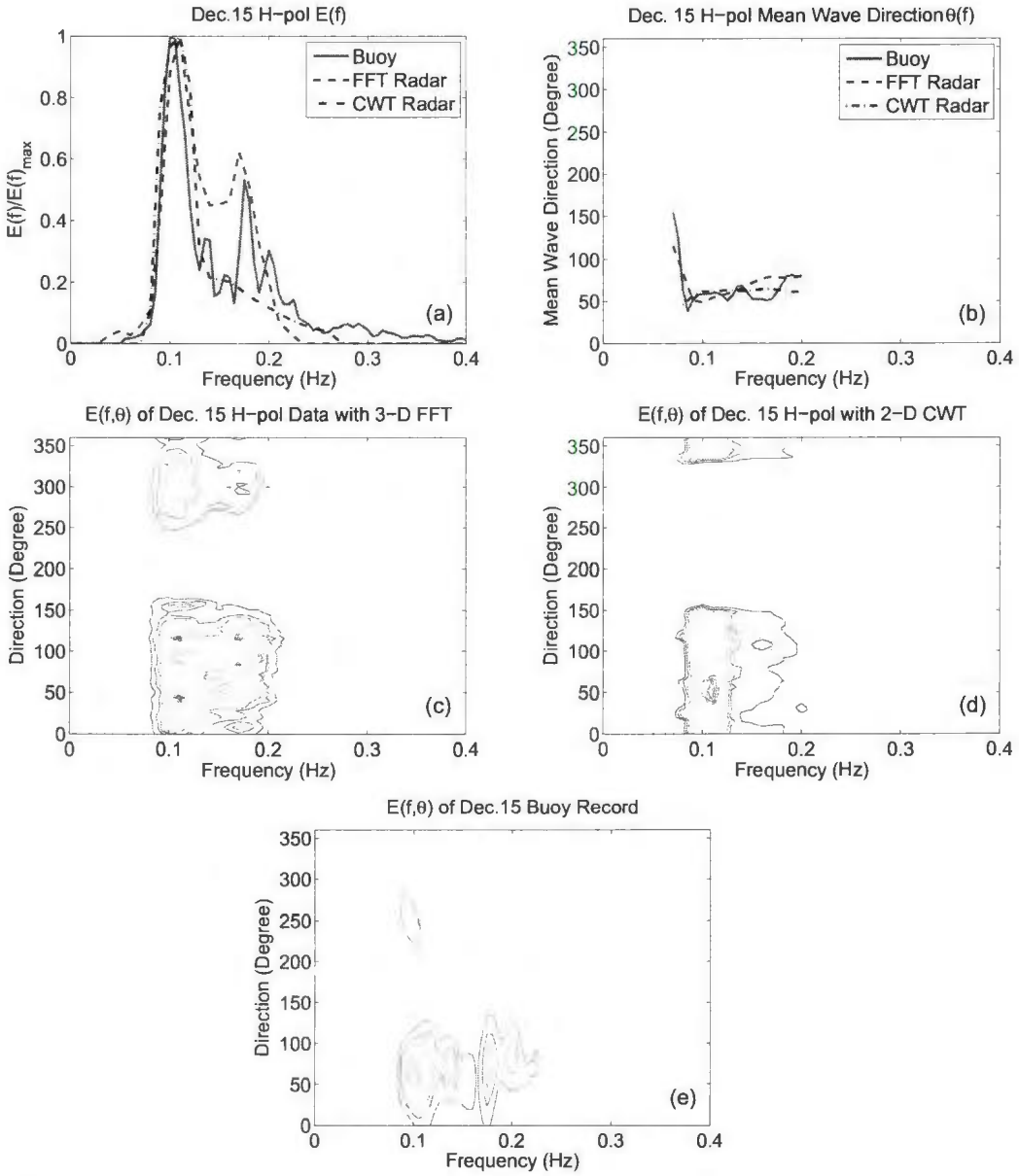

Figure 4.37: Comparison of Dec.15 results from buoy and H-pol radar data: (a) 1-D frequency spectrum $E(f)$; (b) Mean wave direction spectrum; $\theta(f)$; (c) 3-D FFT derived directional-frequency spectrum $E_{\mathrm{FFT}}(f,\theta)$; (d) 2-D CWT derived directional-frequency spectrum $E_{\mathrm{CWT}}(f,\theta)$; (e) Buoy-recorded directional-frequency spectrum $E_{\mathrm{buoy}}(f,\theta)$; .

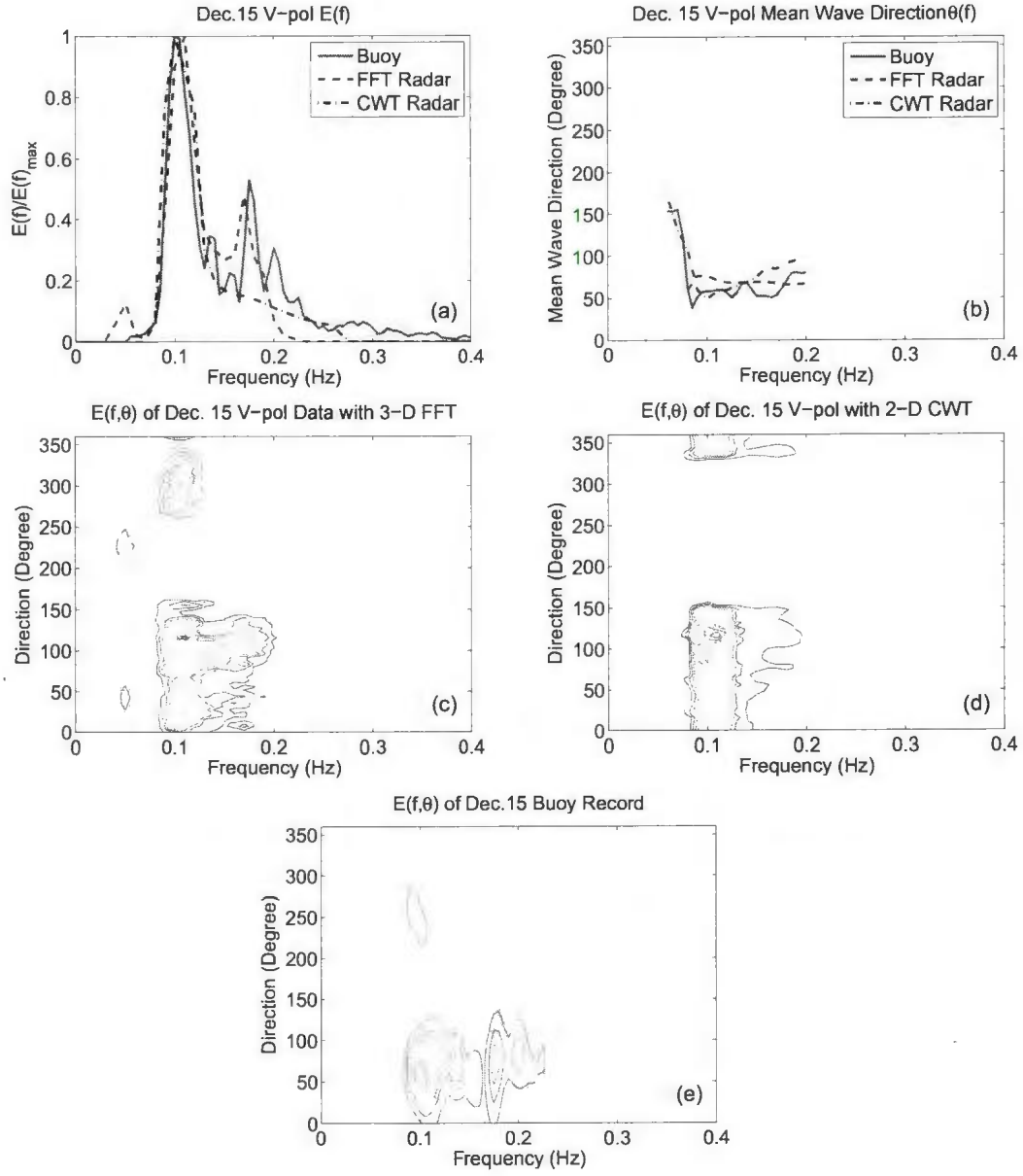

Figure 4.38: Comparison of Dec.15 results from buoy and V-pol radar data.

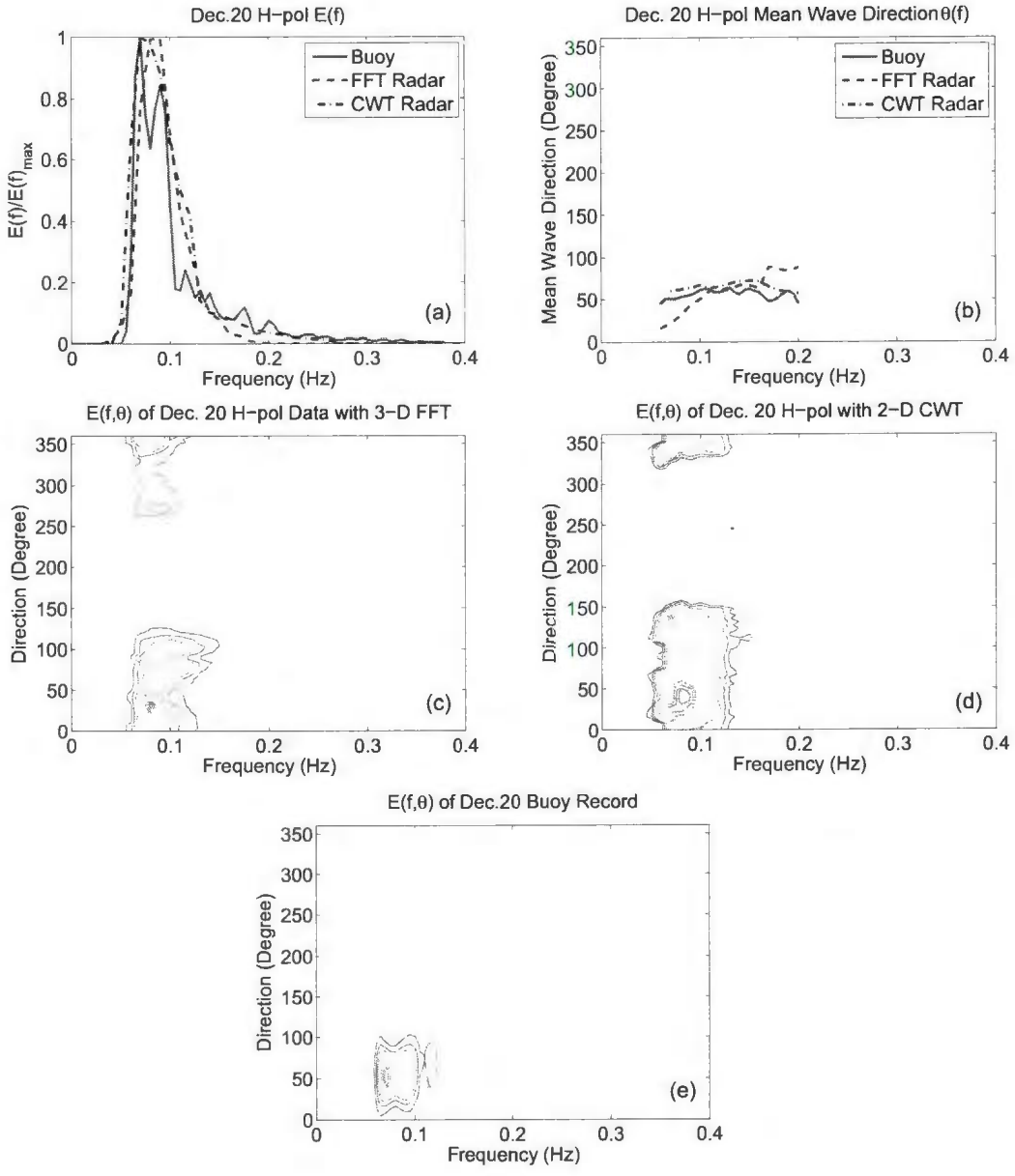

Figure 4.39: Comparison of Dec.20 results from buoy and H-pol radar data.

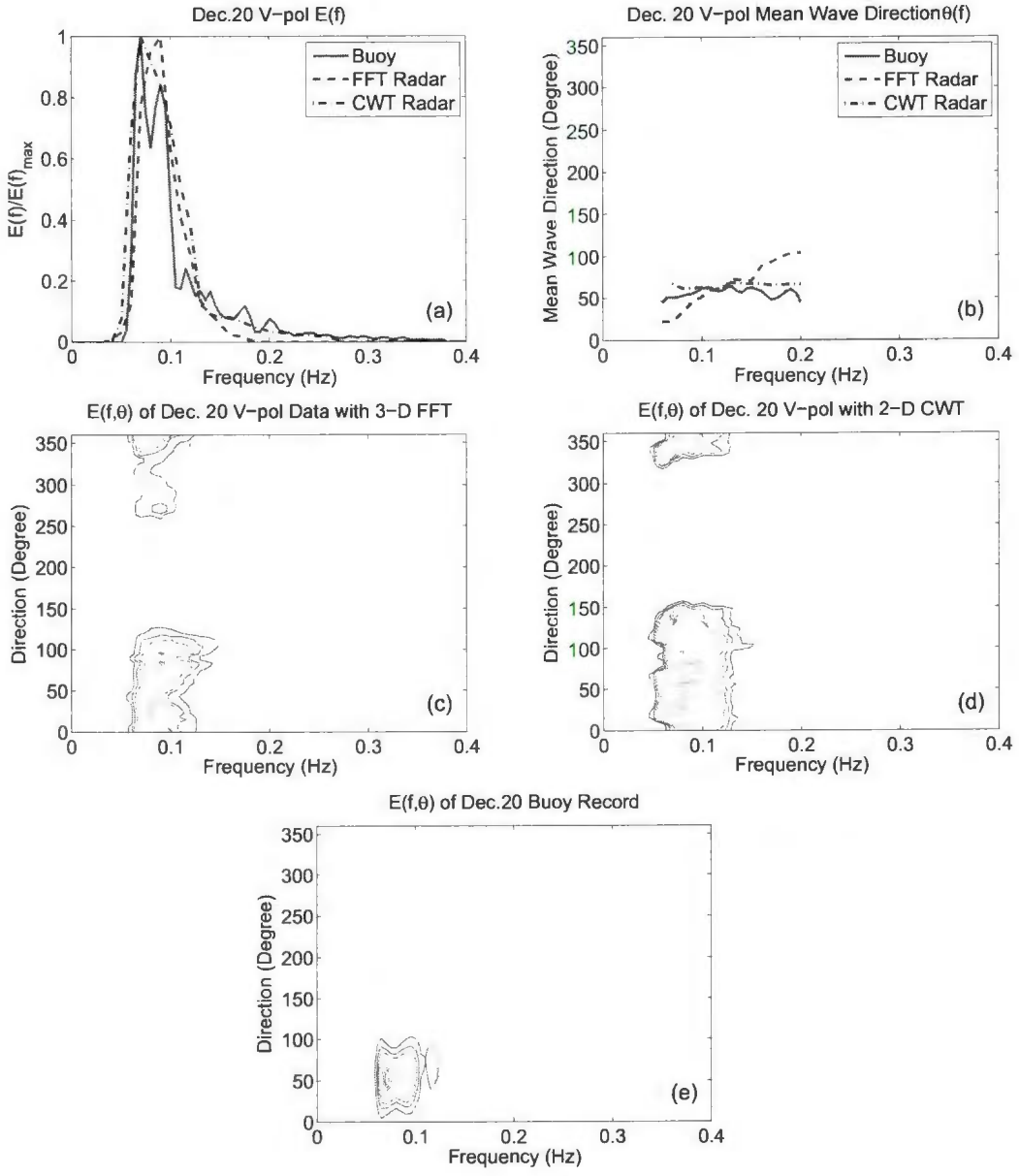

Figure 4.40: Comparison of Dec.20 results from buoy and V-pol radar data.

Chapter 5

Conclusions and Future Work

5.1 Conclusions

In this thesis, current and wave information extraction algorithms for use with nautical radar data are reviewed. Then, improvements and new algorithms are presented. Both simulated and field data have been used in the validation of the techniques.

Firstly, the least squares (LS), iterative LS, and the normalized scalar product (NSP) surface current estimation methods are investigated. The iterative LS method is improved by introducing an adaptive iteration termination criterion to reduce the number of iterations while improving the efficiency and accuracy of the current estimation. The accuracy of the NSP method relies on a large range and a fine resolution of the velocity for the two-dimensional search; Thus a large number of calculations are usually expected in this process. To reduce the computational cost of this method, an improvement is suggested using variable search ranges and resolutions.

Secondly, the classic 3-D FFT-based wave analysis algorithm is studied. However, the non-wave, fundamental and higher-order harmonic wave components that fall in the pass band of the required filter are all used for wave spectrum derivation in existing

algorithms. In this thesis, an enhanced algorithm using a modified band-pass filter to extract ocean wave information of fundamental components from nautical radar images is proposed based on the mode classification results for the iterative LS current estimation.

In addition, a new strategy to retrieve ocean wave information from nautical radar images based on 2-D continuous wavelet transform (CWT) analysis is also proposed. The research explores the wavelet selection and parameter configuration. It is observed from a series of simulation tests that the selection of scaling parameters significantly affects the derived wave field results. Thus, the relation of the maximum wavelet scaling parameter a_{max} to the minimum distinguishable wavenumber is deduced, and empirical values of the calibration factor, β, which refines the optimal a_{max} under varying wave conditions, are provided. A look-up-table-based wave analysis algorithm is first proposed with the knowledge of the empirical optimal values of calibration factor with reference to wave period from other instrumentation. Then a self-adaptive wave analysis algorithm is designed using an iterative verification process involving the tabulated calibration factors for different states without given T_{01}.

Lastly, both simulation and dual-polarized field data tests are used for the algorithm verification and analysis. In the simulated data test, radar images are generated under different circumstances assuming shadowing and tilt modulation. It is concluded from the simulation that accurate and robust current estimation can be obtained from the iterative LS and NSP methods for different current velocities, and mean wave periods. Also, the ocean wave spectra and associated parameters derived from both 3-D FFT-based and 2-D CWT-based wave algorithms agree well with the input data and, in particular, can be retrieved for different current speeds and mean wave periods. It is also observed that the position of the sub-image sequence may affect the retrieved ocean wave information and it is suggested that the optimal posi-

tions of the sub-image sequence for wave analysis are selected at the wave propagation direction, $200-800$ m away from the radar antenna for the simulated data test. Data were used from a two-day field test which involve both H-pol and V-pol X-band radars on the Canadian East Coast. A TRIAXYS wave buoy and ADCP record collected at the same time near the radar antenna were also available as ground truth for analysis. Current velocity results show that both the iterative LS and NSP methods can be used to retrieve reliable current information. Also, the V-pol data allows for better current estimation than that does the H-pol data, even under low sea state conditions. Wave spectra parameters using both the 3-D FFT-based and 2-D CWT-based wave algorithms are close to those obtained from the buoy reference. It appears that reliable ocean wave information can be retrieved from both the H-pol and V-pol data using modified modulation transfer functions. It is concluded from the results that the key to the retrieval of accurate wave information with the 2-D CWT-based method is the proper selection of the calibration factor and modulation transfer function.

5.2 Future Work

In this thesis, the field data is collected from a ground-based radar system under a low sea state within a limited time span. A further validation with longer data sets collected during a variety of sea states and ship speeds should be conducted. Also, as discussed in Chapter 2, the thresholds used in the LS and iterative LS current estimation are selected empirically. It is necessary to further explore an adaptive threshold selection method under varying conditions in order to improve the accuracy and robustness of the results.

In the 2-D CWT wave analysis, the effect of current velocity on the performance of the algorithm is not considered. Also, directional ambiguity inherently exists in

the wavenumber spectrum obtained from the 2-D CWT analysis. In this thesis, the ambiguity is removed by referencing the buoy data. Ongoing work suggests that a 3-D wavelet analysis for the estimation of currents and the possible elimination of the wave directional ambiguity should be explored [82].

Bibliography

[1] D. H. Nomiyama and T. Hirayama, "Evaluation of marine radar as an ocean-wave-field detector through full numerical simulation," *J. Marine Sci. Technol.*, vol. 8, pp. 88-98, 2003.

[2] J. C. Nieto, K. Hessner, P. Jarabo-Amores, and D. de la Mata-Moya, "Signal-to-noise ratio analysis to estimate ocean wave heights from X-band marine radar image time series," *IET Radar Sonar Navig.*, 2,(1), pp. 35-41, 2008.

[3] F. F. Wright, "Wave observation by shipboard radar," *Ocean Sci. and Ocean Eng.*, vol.1, pp. 506-514, 1965.

[4] W. Alpers, "Imaging ocean waves by synthetic aperture radar: A review," *Satellite Microwave Sensing*, pp. 107–120, Ellis Horwood, Chichester, U. K., 1983.

[5] W. McLeish, D. B. Ross, "Imaging radar observations of directional properties of ocean waves," *J. Geophys. Res.*, vol. 88, pp. 4407–4419, 1983.

[6] D. E. Barrick, M. W. Evans, B. L. Weber, "Ocean surface currents mapped by radar," *Science*, vol. 198, pp. 138–144, 1977.

[7] T. Ijima, T. Takahashi, H. Sasaki, "Application of radars to wave observations," *Proc. 11th Conf. Coastal Eng.*, vol. 30(1), pp. 10–22, 1964.

[8] R. Watson-Watt, *The Use of Radar at Sea*, pp. 332, Hollis and Carter, London, 1978.

[9] H. M. Oudshorn, "The use of radar in hydrodynamic surveying," *Proc. 7th Conf. Coastal Eng.*, pp. 59–76, 1960.

[10] T. G. Willis, and H. Beaumont, "Wave direction measurements using sea surveillance radars," *Tech. Memo. TR 118*, R. Aircraft Establishment, Farnbough, Great Britain, 1971.

[11] V. F. Evmenov, "Test of the radar method of defining ocean waves elements," *Fluid Mech. Sov. Res.*, vol. 25, pp. 141–145, 1973.

[12] M. G. Mattie, and D. L. Harris, "A system for using radar to record wave direction," *Tech. Rep.*, vol. 79-1, pp. 50, U.S. Army Corps of Eng., Coast. Eng. Res. Ctr., Fort Belvoir, Va., 1979.

[13] P. Hoogeboom, W. Rosenthal, "Directional wave spectrum radar images," *Proc. IEEE Int. Geoscience and Remote Sensing Symp.*, Munich, June 1 4, 1982.

[14] F. Ziemer, W. Rosenthal, and H. Carlson, "Measurements of directional wave spectra by ship radar," *Proc. Int. Assoc. for Phys. Sci. of the Oceans Symp.*, Hamburg, Federal Republic of Germany, 1983.

[15] V. Atanassov, W. Rosenthal, and F. Ziemer, "Removal of ambiguity of two-dimensional power spectra obtained by processing ship radar images of ocean waves," *J. Geophys. Res.*, vol. 90, no. C1, pp. 1061-1067, 1985.

[16] I. R. Young, W. Rosenthal, and F. Ziemer, "A three-dimensional analysis of marine radar images for the determination of ocean wave directionality and surface currents," *J. Geophys. Res.*, vol. 90, pp. 1049-1059, 1985.

[17] J. C. Nieto Borge, F. Ziemer, J. Seemann, and C. Senet, "Overcome the Nyquist limit in frequency in nautical radar measurement of wave fields," *Proc. 17th Int. Conf. OMAE*, Lisbon, Portugal, 1998.

[18] F. Ziemer, "Directional spectra from shipboard navigation radar during LEWEX," *Directional ocean wave spectra*, R. C. Beal, ed., Johns Hopkins University Press, Baltimore, pp. 80–84.

[19] C. M. Senet, J. Seemann, and F. Ziemer, "Current and wave observation from coastal and vessel mounted stations by marine radar," *Proc. 4th Int. Conf. on Remote Sensing for the Marine and Coastal Environments*, pp. 1485–1491, 1997.

[20] IAHR Working Group on Wave Generation and Analysis, "List of sea-state parameters," *J. Waterway, Port, Coastal, Ocean Eng.*, vol.115, pp. 793-808, 1989.

[21] M. Darras, "IAHR list of sea state parameters: A presentation," *Proc. Seminar on Wave Analysis and Generation in Lab. Basins*, XXII Congress, International Association for Hydraulic Research, pp. 11-74, 1987.

[22] W. Alpers, and K. Hasselmann, "Spectral signal to clutter and thermal noise properties of ocean wave imaging synthetic aperture radars," *Int. J. Remote Sens.*, vol. 3, pp. 423 -446, 1982.

[23] F. Ziemer, and H. Gunther, "A system to monitor ocean wave fields," *Proc. 2nd Int. Conf. on Air-Sea Interaction and Meteorology and Oceanography of the Coastal Zone*, vol.2, pp. 13-16, 1994.

[24] J. C. Nieto Borge, "Significant wave height estimation from nautical radar data sets," *Rep. 98/E/28*, GKSS-Research Center, Hamburg, Germany.

[25] J. C. Nieto Borge, K. Hessner, and K. Reichert, "Estimation of the significant wave height with X-band nautical radars," *Proc. 18th Int. Conf. on Offshore Mechanics and Arctic Engineering*, St. Johns, NF, Canada, vol. 1, pp. 1-8, 1999.

[26] K. Hessner, J. C. Nieto Borge, and H. Gunther, "Evaluation of WaMoS II wave data," *Proc. Fourth Int. Symp. Ocean Wave Meas. Anal.*, San Francisco, CA, ASCE, pp. 221–230, 2001.

[27] L. B. Wenzel, "Electromagnetic scattering from the sea at low grazing angles," *Surface Waves and Fluxes*, G. L. Geernaert and W. J. Plant, Eds., Kluwer Academic, pp. 41 108, 1990.

[28] M. D. Henschel, J. R. Buckley, and F. W. Dobson, "Estimates of wave height from low incidence angle sea clutter," *Proc. Fourth Int. Workshop on Wave Hindcasting and Forecasting*, Banff, AB, Canada, 1995.

[29] J. R. Buckley, and J. Aler, "Estimation of ocean surface wave height from grazing incidence microwave backscatter," *Proc. IEEE Int. Geoscience and Remote Sensing Symp.*, Singapore, China, pp. 1015–1017, 1997.

[30] J. R. Buckley, and J. Aler, "Enhancements in the determination of ocean surface wave height from grazing incidence microwave backscatter," *Proc. IEEE Int. Geoscience and Remote Sensing Symp.*, Seattle, WA, 1998.

[31] J. Seemann and F. Ziemer, "Computer simulation of imaging ocean wave fields with a marine radar," *Proc. MTS/IEEE Oceans Conf.*, pp. 1128-1133, 1995.

[32] J. C. Nieto Borge, R. G. Rodriguez, K. Hessner, and I. P. Gonzales, "Inversion of marine radar images for surface wave analysis," *J. Atmos. Ocean. Technol.*, vol. 21, pp. 1291-1300, 2004.

[33] F. Ziemer, C. Brockmann, R. A. Vaughan, J. Seemann, and C. M. Senet, "Radar survey of near shore bathymetry within the OROMA project," *EARSeL ePro-ceedings*, vol. 3(2), pp. 282 288, 2004.

[34] H. Dankert, and W. Rosenthal, "Ocean surface determination from X-band radar-image sequences," *J. Geophys. Res., Oceans*, vol. 109, pp. 2156-2202, 2004.

[35] P. H. Y. Lee, J. D. Barter, K. L. Beach, C. L. Hindman, B. M. Lake, H. Rungaldier, J. C. Shelton, A. B. Williams, R. Yee, and H. C. Yuen, "X-band microwave backscattering from ocean waves," *J. Geophys. Res.*, vol. 100, pp. 2591–2611, 1995.

[36] W. J. Plant, and W. C. Keller, "Evidence of Bragg scattering in microwave Doppler spectra of sea return," *J. Geophys. Res.*, vol. 310, pp. 299–16, 1990.

[37] D.E. Hasselman, M. Dunkel, J. A. Ewing, "Directional wave spectra observed during Jonswap 1973," *J. Phys. Oceanogr.*, vol. 10, no. 8, pp. 1264-1280. 1980.

[38] F. K. Takase and T. Hirayama, "Evaluation of marine wave radar, part I. fundamental considerations and numerical generation of radar image," *J. Soc. Nav. Archit. Jpn.*, vol. 187, pp.85-92, 2000.

[39] F. K. Takase and T. Hirayama, "Evaluation of marine wave radar, part II. wave parameters from radar images," *J. Soc. Nav. Archit. Jpn.*, vol. 188, pp. 225-237, 2000.

[40] D. B. Trizna, D. J. Carlson, "Studies of dual polarized low grazing angle radar sea scatter in nearshore regions," *IEEE Trans. Geosc. Remote Sens.*, vol. 34, pp. 747-757, 1996.

[41] D. C. Schleher, *MTI and Pulsed Doppler Radar*, Norwood, MA: Artech House, 1991.

[42] F. E. Nathanson, *Radar Design Principles: Signal Processing and the Environment, 2nd ed*, New York: Mcgraw-Hill, 1990.

[43] H. Mitsuyasu, F. Tasai, T. Suhara, S. Mizuno, M. Ohkusu, T. Honda, and K. Rikiishi, "Observation of the power spectrum of ocean waves using a cloverleaf buoy," *J. Phys. Oceanogr.*, vol. 10, pp. 286–296, 1980.

[44] J. An, W. Huang, and E. Gill, "Numerical simulation of X-band marine radar imaging," *Proc. IEEE NECEC Conf.*, Newfoundland, Canada, 2011.

[45] J. Seemann, F. Ziemer, and C. M. Senet, "A method for computing calibrated ocean wave spectra from measurements with a nautical X-band radar," *Proc. MTS/IEEE Oceans Conf., 500 Years of Ocean Exploration*, Halifax, NS, Canada, vol. 2, pp. 1148-1154, 1997.

[46] J. Seemann, C. M. Senet, H. Dankert, H. Hatten, and F. Ziemer, "An iterative technique to determine the near surface current velocity from time series of sea surface images," *Proc. MTS/IEEE Oceans Conf., 500 Years of Ocean Exploration*, Halifax, NS, Canada, vol. 1, pp. 66–72, 1997.

[47] C. M. Senet, J. Seemann, and F. Ziemer, "The near-surface current velocity determined from image sequences of the sea surface," *IEEE Trans. Geosci. Remote Sens.*, vol. 39, pp. 492-505, 2001.

[48] R. Gangeskar, "Ocean current estimated from X-band radar sea surface images," *IEEE Geosci. Remote Sens.*, Vol. 40, No. 4, pp. 783-792, 2002.

[49] F. Serafino, C. Lugni, and F. Soldovieri, "A novel strategy for the surface current determination from marine x-band radar data," *IEEE Geosci. Remote Sens. Lett.*, vol. 7, pp. 232-236, 2010

[50] F. Serafino, F. Soldovieri, C. Lugni, "Sea-state monitoring via X-band marine radar images sequences: a new approach for an accurate surface currents estimation," *Proc. ASME 2009 28th International Conference on Ocean, Offshore and Arctic Engineering*, Honolulu, Hawaii, pp. 515-522, 2009.

[51] J. C. Nieto Borge and C. Guedes Soares, "Analysis of directional wave fields using X-band navigation radar," *Coastal Eng.*, vol. 40, pp. 375-391, 2000.

[52] K. Reichert, K. Hessner1, J. C. Nieto Borge, J. Dittmer, "WaMoS II: A Radar based wave and current monitoring system," *Proc. International Offshore and Polar Engineering Conference (ISOPE)*, Brest, France, vol. 3, 1999.

[53] J. C. Nieto, K. Reichert, and J. Dittmer, "Use of nautical radar as a wave monitoring instrument," *Coastal Eng.*, vol. 37, pp. 331-342, 1999.

[54] M. Alfonso, A. Muñoyerro, and J. C. Nieto Borge, "Directional wave navigation radar measurements compared with pitch-roll buoy data," *J. Offshore Mech. Arct. Eng.*, vol. 119, pp. 25–29, 1997.

[55] J. C. Nieto Borge, R. Sanz González, K. Hessner, K. Reichert, and C. Guedes Soares, "Estimation of sea state directional spectra by using marine radar imaging of sea surface," *Proc. 19th Int. Conf. on Offshore Mechanics and Arctic Engineering, Paper OMAE2000/ SR-6120*, 2000.

[56] J. C. Nieto Borge, M. Alfonso, and R. Sanz, "Reliability of measured sea states using radar system on shore," *Proc. 14th Int. Conf. on Offshore Mechanics and Arctic Engineering*, vol. II, pp. 63, 1995.

[57] P. Izquierdo, C. Guedes Soares, J. C. Nieto, and G. R. Rodriguez, "A comparison of sea-state parameters from nautical radar images and buoy data," *Ocean Eng.*, vol. 31, pp. 2209-2225, 2004.

[58] P. Izquierdo, J. C. Nieto Borge, C. Guedes Soares, R. Sanz González, R., and G. Rodríguez, "Comparison of wave spectra from nautical radar images and scalar buoy data," *J. Waterway, Port, Coastal, Ocean Eng.*, vol. 131(3), pp. 123–131, 2005.

[59] J. C. Nieto Borge, and K. Hessner, "Comparison of WaMoS II with in situ measurements," in D. Hauser, K. Kahma, H. E. Krogstad, S. Lehner, J. A. J. Monbaliu, and L. R. Wyatt, (Eds.): 'Measuring and analysing the directional spectra of ocean waves,' EU COST Action 714, ISBN 92-898-0003-8, EUR 2136, pp. 465, 2005.

[60] T. Hirayama, Y. Hagino, T. Matsuno, "Real-time estimation of sea spectra based on motions of a running ship - full scale trial (1st report)," *J. Kansai Soc. Nav. Archit. Jpn.*, vol. 198, pp. 17-29, 1985.

[61] T. Hirayama T, "Real-time estimation of sea spectra based on motions of a running ship - full scale trial (2nd report) - directional wave estimation," *J. Kansai Soc. Nav. Archit. Jpn.*, vol. 204, pp. 21-27, 1987.

[62] T. Hirayama, K. Minami, and M. Hiramastu, "Development of hybrid-type on board measuring system for directional wave spectrum (1st report)," *J. Soc. Nav. Archit. Jpn.*, vol. 180, pp. 295-309, 1996.

[63] T. Hirayama, K. Minami, and M. Hiramastu, "Development of hybrid-type on board measuring system for directional wave spectrum (2nd report)," *J. Soc. Nav. Archit. Jpn.*, vol. 182, pp. 217-229, 1997.

[64] T. Iseki, and K. Ohtsu, "Bayesian estimation of directional wave spectra based on ship motions," *Control Eng. Pract.*, vol. 8(2), pp. 215-219, 2000.

[65] H. Yoshimoto, and I. Watanabe, "On the estimation of encounter directional wave spectra of a running ship," *J. Soc. Nav. Archit. Jpn.*, vol. 176, pp. 107-117, 1994.

[66] H. Ishida, T. Inoue, M. Hayashi, S. Shiotani, and R. Hosoda, "Wave observation apparatus by marine radar and evaluation of its analytical results," *Proc. Techno Ocean'94*, vol. I, pp. 469-474, 1994.

[67] T.Hirayama, S. G. Park, F. K. Takase, Y. Hirakawa, and T. Takayama, "Directional ocean wave spectra from marine radar," *Proc. Int. Offshore Polar Eng. Conf.*, pp. 119-123, 2002.

[68] F. Wang, J. Wang, and S. Wang, "Estimation of significant wave height from X-band marine radar images," *3rd International Congress on Image and Signal Processing (CISP)*, vol. 5, pp. 2172-2174, 2010.

[69] L. Cui, "Study on remote sensing mechanism and retrieval method of ocean wave and current with X band radar," PHD dissertation in Chinese, Chinese Academy of Sciences, China, 2010.

[70] L. Cui, Y. He, H. Shen, and H. Lü, "Measurements of ocean wave and current field using dual polarized X-band radar," *Chin. J. Oceanol. Limnol.*, vol. 28(5), pp. 1021-1028, 2010.

[71] H. Li, L. Cui, Z. Qiu, S. Zhang, and Y. He, "Improving sea states monitoring of nautical radar using dispersion relation of nonlinear ocean waves," *Proc. IEEE Int. Geoscience and Remote Sensing Symp.*, vol. 3, pp. III-41 - III-44, 2009.

[72] C.K. Chui, L. Montefusco, and L. Puccio, *Wavelets: Theory, Algorithms and Applications*, Academic Press, Boston, 1994.

[73] I. Daubechies, "The Wavelet Transform, Time-Frequency Localization and Signal Analysis," *IEEE Trans. Inform. Theory*, vol. 36, No. 6, pp. 961-1005, 1990.

[74] G. E. Carlson, "Wavelet processing of SAR ocean wave images," *Proc. IEEE Int. Geoscience and Remote Sensing Symp.*, Firenze, Italy, vol. 1, pp. 679-681, 1995.

[75] D. Jordan, R. W. Miksad, and E. J. Powers "Implementation of the continuous wavelet transform for digital time series analysis," *Rev. Sci. Instrum.*, vol. 68, no. 3, pp. 1484-1494, 1997.

[76] S. R. Massel, "Wavelet analysis for processing of ocean surface wave records," *Ocean Eng.*, vol. 28, pp. 957-987, 2001.

[77] M. C. Huang, "Wave parameters and functions in wavelet analysis," *Ocean Eng.*, vol. 31, pp. 111-125, 2004.

[78] J. -P. Antoine, R. Murenzi, P. Vandergheynst, and S. Twareque Ali, *Two Dimensional Wavelets and Their Relatives*, Cambridge: Cambridge University Press, 2004, ISBN:9780521065191.

[79] L. -C. Wu, L. Z. H. Chuang, D. J. Doong, and C. C. Kao, "Ocean remotely sensed image analysis using two-dimensional continuous wavelet transform," *Int. J. Remote Sens.*, vol. 32, no. 23, pp. 8779-8798, 2011.

[80] L. Z. H. Chuang, L. -C. Wu, D. J. Doong, and C. C. Kao, "Two-dimensional continuous wavelet transform of simulated spatial images of waves on a slowly varying topography," *Ocean Eng.*, vol. 35, pp. 1039-1051, 2008.

[81] D. J. Doong, L. -C. Wu, and C. C. Kao, "Spatial wave fields extracted from marine radar images by wavelet transform," *Proc. 3rd Chinese-German Joint Symposium on Coastal and Ocean Eng.*, Taiwan, 2001.

[82] D. J. Doong, L. -C. Wu, C. C. Kao, L. Z. H. Chuang, "Wavelet spectrum extracted from coastal marine radar images," *Proc. 13th International Offshore and Polar Engineering Conference (ISOPE)*, Honolulu, Hawaii, USA, pp. 258-264, 2003.

[83] X. -B. Feng, Y. -X. Yan, W. Zhang, "Application of two-dimensional wavelet transform in near-shore X-band radar images," *J. Hydrodynamics*, vol. 23, no. 2, pp. 179-186, 2011.

[84] J. C. Nieto Borge, A. M. Baquero-Martinez, D. de la Mata-Moya, J. L. Alvarez-Perez, "Analysis of the sea clutter structure using temporal sequences of X-band marine radar images," *Proc. IEEE International Conference on Radar*, pp. 563-568, 2008.

[85] W. Huang, and E. Gill, "Surface current measurement under low sea state using dual polarized X-band nautical radar," *IEEE J. Sel. Topics Earth Observ. Remote Sens.*, vol. 5, no. 6, pp. 1868-1873, 2012.

[86] W. Huang, and E. Gill, "Simulation analysis of sea surface current extraction from microwave nautical radar images," *Proc. 19th IEEE International Conference on Image Processing (ICIP)*, Orlando, FL, USA, pp. 2673-2676, 2012.

[87] W. Huang, E. W. Gill, and Z. Zhong, "Enhancement of the normalized scalar product method for surface current measurement using nautical radar," *Proc. MTS/IEEE Oceans Conf.*, Hampton Roads, USA, vol.1(4), pp.14-19, 2012.

[88] R. H. Stewart and J. W. Joy, "HF radio measurements of surface currents," *Deep Sea Res.*, vol. 21, pp. 1039–1049, 1974.

[89] H. Nyquist, "Certain topics in telegraph transmission theory," *Trans. AIEE*, vol. 47, pp. 617–644, 1928.

[90] C. E. Shannon, "Communication in the presence of noise," *Proc. Institute of Radio Engineers*, vol. 37(1), pp. 10–21, Jan. 1949.

[91] R. J. Marks, *Introduction to Shannon sampling and interpolation theory*, Spinger-Verlag, New York, 1991.

[92] K. Reichert, "Analysis of the azimuth dependence of the navigation radar imaging of the sea surface," (in German) Diplomarbeit, Fachbereich Geowissenschaften Universitat Hamburg, 1994.

[93] J. An, W. Huang, and E. Gill, "An enhanced algorithm for wave information extraction from X-band nautical radar images," *Proc. MTS/IEEE Oceans Conf.*, Hampton Roads, VA, USA, pp.1-5, 2012.

[94] J. An, W. Huang, "Extraction of fundamental wave components information from X-band nautical radar images," *Proc. IEEE NECEC Conf.*, Newfoundland, Canada, 2012.

[95] J. G. Daugman, "Complete discrete 2-D Gabor transforms by neural networks for image analysis and compression," *IEEE Trans. Acoust., Speech, Signal Process.*, vol. 36, pp. 1169-1179, 1988.

[96] J. An, W. Huang, and E. Gill, "2-D continuous wavelet based algorithm for extracting wave information from nautical radar images," *Proc. IEEE RadarCon'13*, Ottawa, Canada, 2013.

[97] M. K. Ochi, *Ocean waves : the stochastic approach*, Cambridge University Press, Cambridge, U.K, 1998.

1. sub-image acquisition and normalization;

2. generation of an image spectrum by applying 2-D CWT on a single frame of the normalized sub-image using an initial β_0;

3. derivation of a 1-D frequency spectrum $E(f)$ and calculation of the mean period, T_{01}, and application of an empirical threshold to $E(f)$ to check whether any point other than the major peak lies above the threshold line to the left of the major peak in the derived $E(f)$: if such a point is detected, it will be identified as a false peak.

   (a) if any false peak is detected, go back to step (2), increase the value of β by $\Delta\beta$ and repeat steps (2),(3);

   (b) if no false peak is detected, compare the calculated T_{01} with the mean period that corresponds to β using Table 3.1 and (3.27):

      i. if the difference of the two mean periods is larger than a preset threshold ζ, increase the value of β by $\Delta\beta$ and repeat steps (2), (3);

      ii. if the difference is smaller than the specified threshold ζ, β is identified as an appropriate value for wave field analysis. This value may then be used to process the 2-D CWT on the whole radar image sequence and the derived 2-D directional-frequency spectra $E(f, \theta)$ may be averaged for wave information extraction. In this research, if $T_{01} < 10$ s, $\zeta = 0.5$; otherwise, $\zeta = 1$.

The complete self-adaptive wavelet-based algorithm for the extraction of ocean wave information is depicted in Fig. 3.8.